

We are IntechOpen, the world's leading publisher of Open Access books Built by scientists, for scientists

6,300

Open access books available

171,000

International authors and editors

190M

Downloads

Our authors are among the

154

Countries delivered to

TOP 1%

most cited scientists

12.2%

Contributors from top 500 universities



WEB OF SCIENCE™

Selection of our books indexed in the Book Citation Index
in Web of Science™ Core Collection (BKCI)

Interested in publishing with us?
Contact book.department@intechopen.com

Numbers displayed above are based on latest data collected.
For more information visit www.intechopen.com



Excitation-Intensity (EI) Effect on Photoluminescence of ZnO Materials with Various Morphologies

Prasada Rao Talakonda

Additional information is available at the end of the chapter

<http://dx.doi.org/10.5772/64937>

Abstract

The chapter discusses about excitation-intensity effects on photoluminescence emission peaks of zinc oxide (ZnO) material. ZnO is an ideal material for optoelectronic devices due to its wide band gap of 3.37 eV and some exciting optical properties. The performance of optoelectronic devices is greatly affected by the vibrational properties of the material, which are influenced by the interaction of phonons with free and bound electron-hole pairs. The photoluminescence (PL) spectroscopy is used to understand the extrinsic and intrinsic defects in ZnO materials. Understanding PL of ZnO nanostructures/thin films may lead to development of more efficient ZnO-based optoelectronic devices.

Keywords: ZnO, Defects, excitation intensity, photoluminescence

1. Introduction

Luminescence is one of the fastest growing and most useful analytical techniques in science and technology. The applications of luminescence can be found in various subject areas as materials science, microelectronics, clinical chemistry, biology, physics, environmental science, chemistry, toxicology, biochemistry, pharmaceuticals, and medicine. The term luminescence includes a wide variety of light-emitting processes, which originate their names from the varied sources of excitation energy that power them.

Photoluminescence (PL) spectroscopy is a sensitive nondestructive technique, suitable for identifying point defects including extrinsic and intrinsic defects in materials [1]. It is a useful tool to evaluate the quality and to study the physical parameters of semiconductor materials

in the form of thin films and nanomaterials. Zinc oxide (ZnO) is one of the promising semiconductor materials of II–VI group, because of its wider band gap (3.37 eV) and large excitation binding energy (60 meV) at room temperature [2]. ZnO thin films and nanostructures are increasingly being used in light-emitting diodes, solar cells, chemical sensors, photocatalysis, and antibacterial materials, etc., because of their unique physical properties [2, 3].

In general, defects and impurities are playing an important role in the semiconductor industry to develop devices. In the case of ZnO material, it is very difficult to understand and study the role of defects or impurities in order to develop optoelectronic devices. Native or intrinsic defects are existing in the ZnO material such as oxygen vacancies (V_{O}), zinc interstitials (Zn_{i}), oxygen interstitial (O_{i}), zinc vacancies (V_{Zn}), zinc antisites, and oxygen antisites. Understanding the incorporation and behavior of intrinsic defects in ZnO material is essential to its successful application in optoelectronic devices. These native defects have long been believed to play an important role in ZnO-based devices. The band-to-band excitation of ZnO promotes electrons from the valence band to the conduction band, leaving holes in the valence band. The holes migrate from the valence band to deep levels and recombination occurs between electrons from either the conduction band or shallow donor levels and trapped holes on deep levels [4–6]. Basically, the PL of ZnO is related to the presence of holes in the valence band [4]. The PL spectroscopy can help to understand the extrinsic and intrinsic defects in ZnO materials. Understanding of PL on ZnO nanostructure/thin films may lead to development of more efficient ZnO-based optoelectronic devices.

The PL properties of ZnO materials have been widely studied by many research groups and several research groups noticed that excitation intensity (EI) also has important influence on the PL spectra of ZnO material [7, 8]. The current chapter is providing more details about the EI effects on ZnO materials with different morphologies. Three different sets of ZnO samples were deposited on various substrates with three kinds of morphologies. PL and Raman spectra were recorded using LABRAM-HR spectrometer excited with a 325 nm He-Cd laser at room temperature. The excitation intensity-dependent PL and Raman spectra were obtained at room temperature by changing the laser intensity with the change of optical filters. The laser intensity was fixed as P_0 for without filter (no filter). The EI for different filters denoted as $D_{0.03} = P_0/2$, $D_{0.06} = P_0/4$, $D_1 = P_0/10$, $D_2 = P_0/100$, $D_3 = P_0/1000$, $D_4 = P_0/10,000$. Low-temperature PL and Raman spectra were obtained using WITec instrument. The crystal structure and morphology of the samples were characterized by X-ray diffraction (XRD) and scanning electron microscopy (SEM).

2. Results

2.1. ZnO thin films

ZnO thin films with thickness of 450 nm were deposited on glass substrates using spray pyrolysis (SP) technique. The precursor solution for spray pyrolysis was prepared by dissolving appropriate amounts of zinc acetate dihydrate in a mixture of deionized water and ethanol at room temperature. In this mixture, ethanol concentration was 10 ml in 100 ml solution. A

solution of 0.3 M Zn (CH₃CO₂)₂ was used as a precursor, prepared by the dissolving in deionized water and ethanol [3]. A few drops of acetic acid were added to aqueous solutions to prevent the formation of hydroxides. ZnO thin films were deposited on glass substrates at a substrate temperature of 623 K. The glass substrates were cleaned thoroughly with acetone, isopropanol, deionized water, and finally cleaned with the help of an ultrasonic bath for 30 min and dried [3, 9]. The spray nozzle was at a distance of 20 cm from the substrate during deposition [3, 9]. The solution flow rate was held constant at 3 ml/min. Air was used as the carrier gas at the pressure of 2 bar [3, 9]. The structural and morphological properties of ZnO thin films are shown in **Figure 1**.

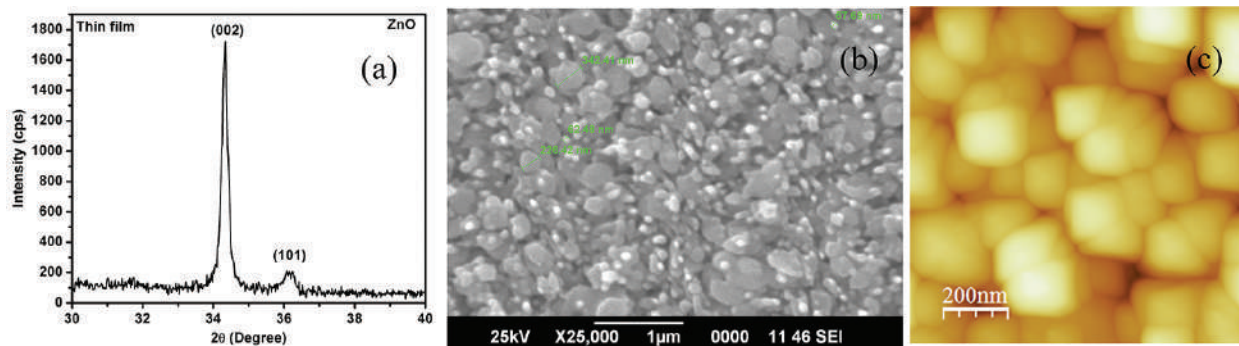


Figure 1. (a) XRD, (b) SEM, and (c) AFM.

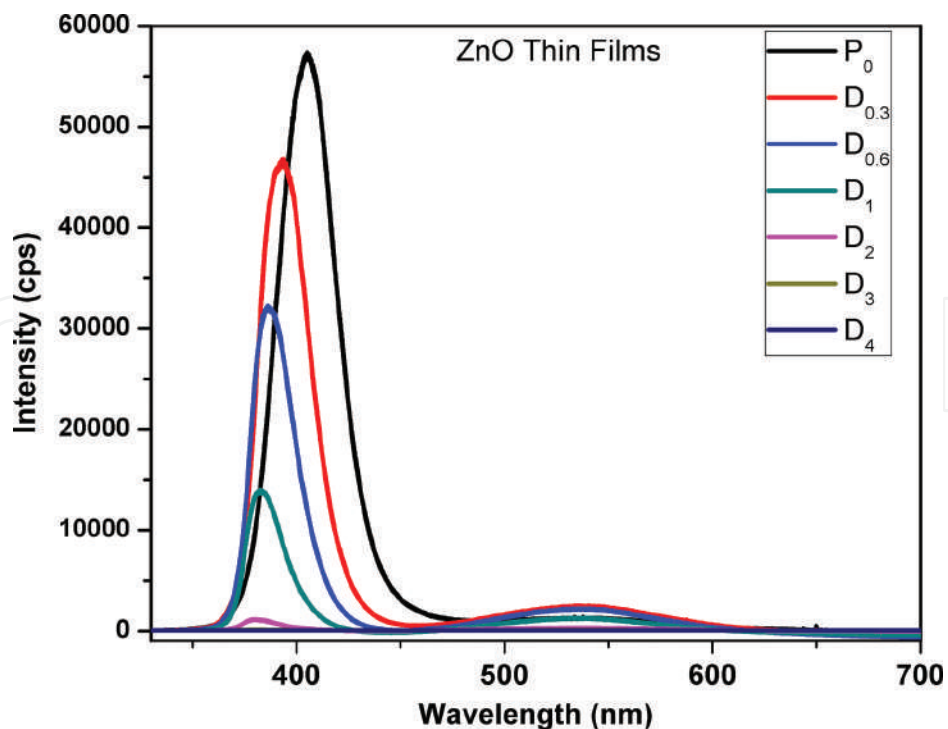


Figure 2. PL emission peak intensity variation with EI intensity.

The XRD studies have shown that all the diffraction peaks belong to ZnO wurtzite structure and the (0 0 2) diffraction peak related to the c -axes is predominant. No other phase was observed. The ZnO thin films are having uniform grains on the surface. These grains are uniformly distributed on the surface of the films without any voids. This can be understood from the SEM and AFM studies (**Figure 1**). The room temperature PL studies are shown in **Figure 2**.

The PL spectrum of ZnO thin films consists of two major emission peaks: a sharp peak located at ultraviolet region, and a weak broad peak in the visible region. According to the previous reports, the appearance of UV emission and visible emission indicates that the existence of native defects in ZnO. The intensity of UV peak of ZnO thin films is decreases with the decreasing EI. The UV emission peak position moved toward lower wavelength side (406–380 nm) with the decreasing of EI. The UV emission peak variation with EI could not explained completely by previous reports. Some previous reports were explained this kind of effect using the concept of laser-induced heating effect. The EI variation studies have extend for different ZnO samples with different morphology (nanorods, tetrapods, etc.) to understand EI effect on ZnO material.

2.2. ZnO nanorods

Nanorods structures like ZnO material were deposited on ITO substrate by electrochemical deposition (EC) technique. Electrolytes were zinc nitrate hydrate ($\text{Zn}(\text{NO}_3)_2 \cdot 6\text{H}_2\text{O}$) and analytic-grade hexamethylenetetramine ($\text{C}_6\text{H}_{12}\text{N}_4$). **Figure 3** shows XRD and the FESEM images of rod-like ZnO nanostructures with different magnifications that have been grown on ITO substrate. The nanostructures are arbitrarily directed and a nonuniform distribution of dense, arbitrarily directed ZnO nanorods, and no branching is observed, which indicates that the ZnO nanorods are grown from spontaneous nucleation.

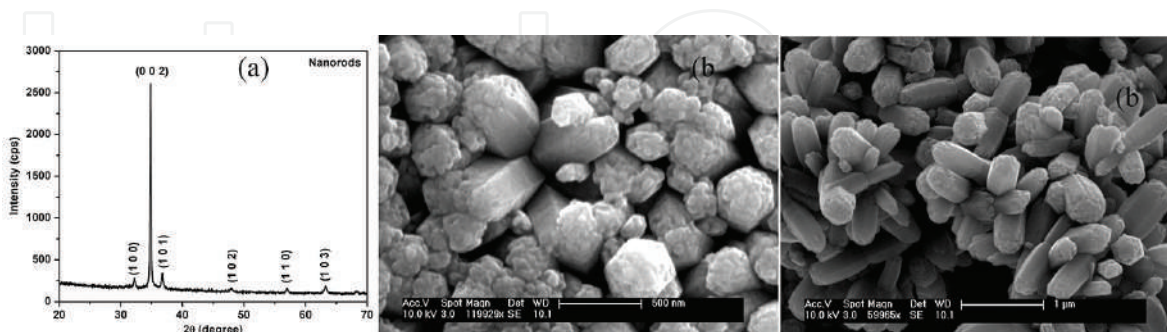


Figure 3. (a) XRD and (b) SEM.

Figure 4 shows that the PL spectrum of ZnO nanorods. The UV emission peak position exhibits a significant blue-shift from 417 to 377 nm with a range of about 40 nm with decrease of EI. The UV peak intensity also varied with the EI.

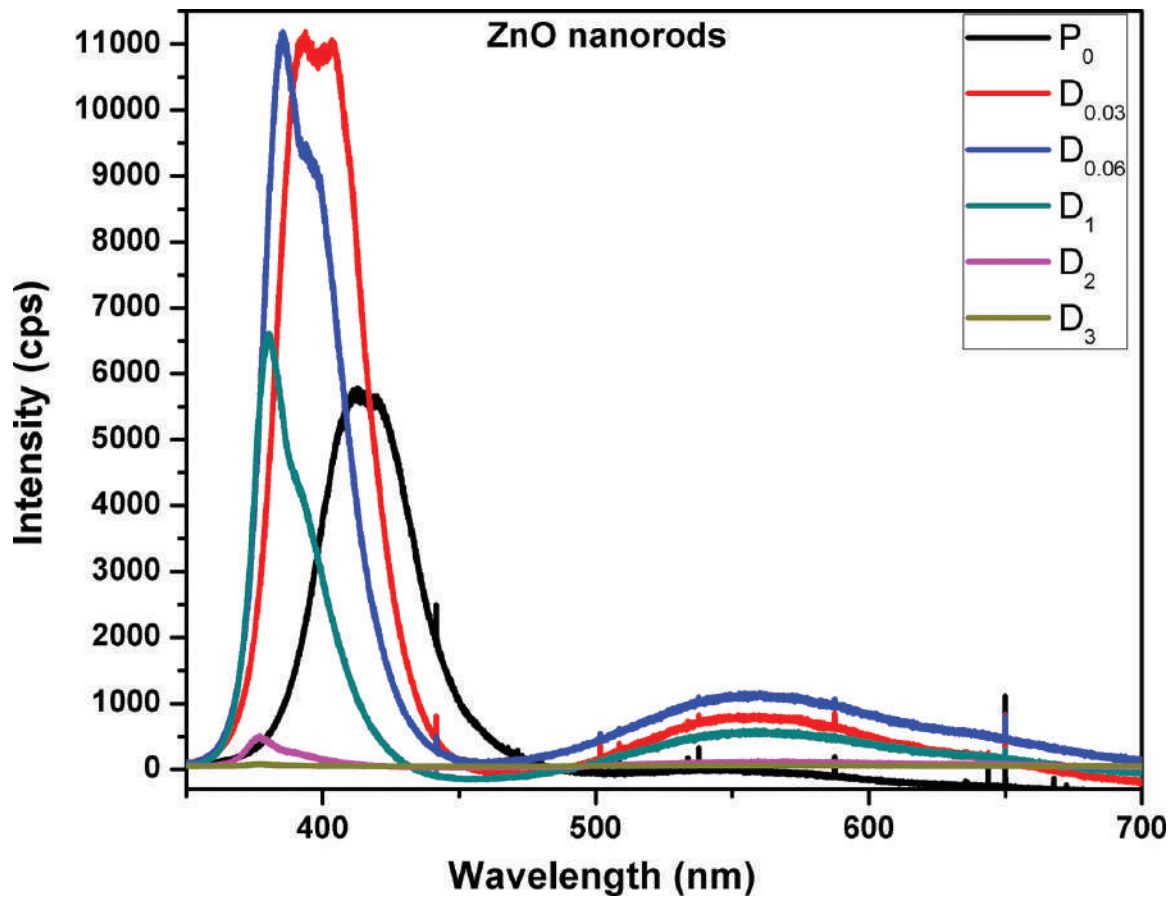


Figure 4. PL spectrum of ZnO nanorods.

2.3. ZnO tetrapods

ZnO tetrapods were synthesized on silicon substrate by vaporizing Zn granule (99.8% purity) in a quartz tube of 30 mm diameter and 100 cm in length at 1200°C in a horizontal tube furnace for 30 min duration at a heating rate of 10°C/min in ambient. **Figure 5** shows the XRD and SEM of ZnO tetrapods.

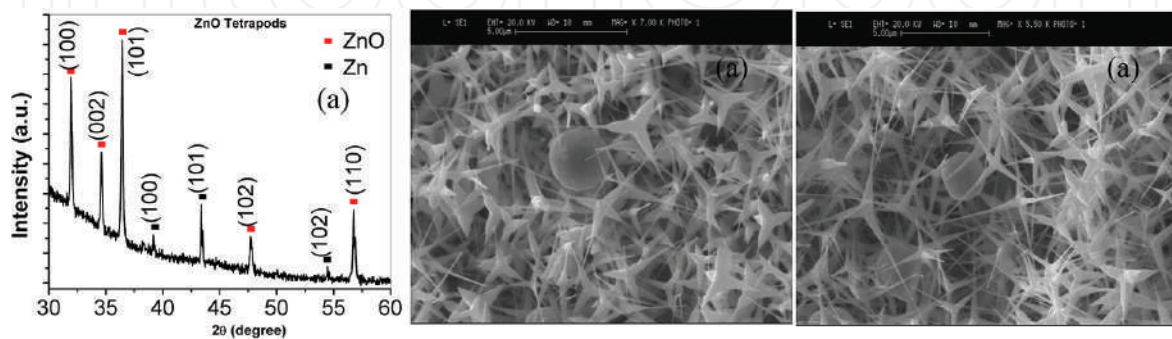


Figure 5. ZnO tetrapods (a) XRD and (b) SEM.

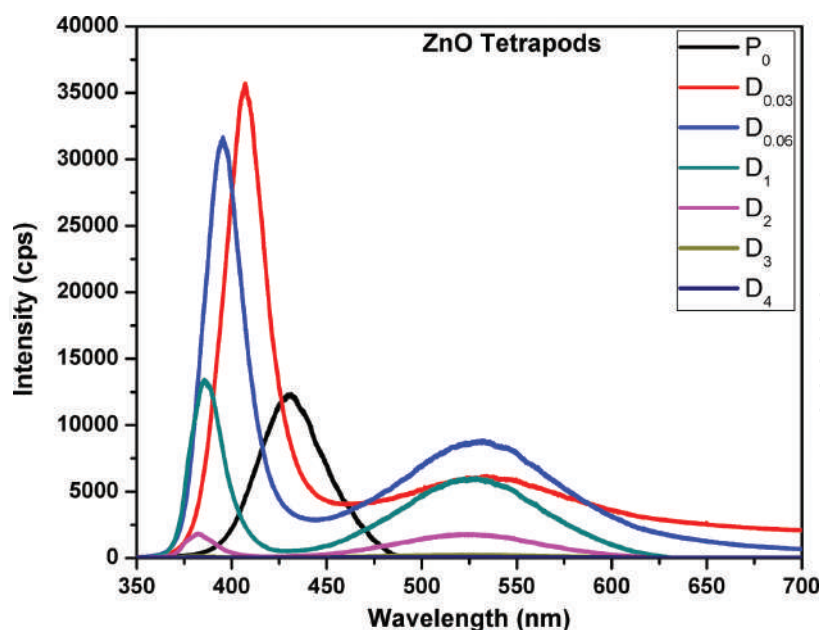


Figure 6. PL spectrum of ZnO tetrapods.

The PL spectrum of ZnO tetrapods is shown in **Figure 6**. The UV emission peak position of ZnO tetrapods moved significantly toward lower wavelength side (from 430 to 380 nm) with the range of about 50 nm when the EI intensity decreased from P_0 to D_4 . The intensity of UV peak is increase with EI ranging from P_0 to $D_{0.06}$, and reaches highest at $D_{0.06}$. Then the UV peak intensity decreases and reaches lowest for the D_4 .

2.4. ZnO bulk material

Bulk ZnO (ZnO powder) was taken from the Sigma Aldrich for the comparative studies to understand the EI effect on ZnO material. **Figure 7** shows the XRD and SEM of ZnO bulk powder. SEM showed micron-sized particles. The PL spectrum of ZnO bulk material is shown in **Figure 8**. The UV emission peak position and intensity variations are similar to the PL results of ZnO nanorods and ZnO tetrapods.

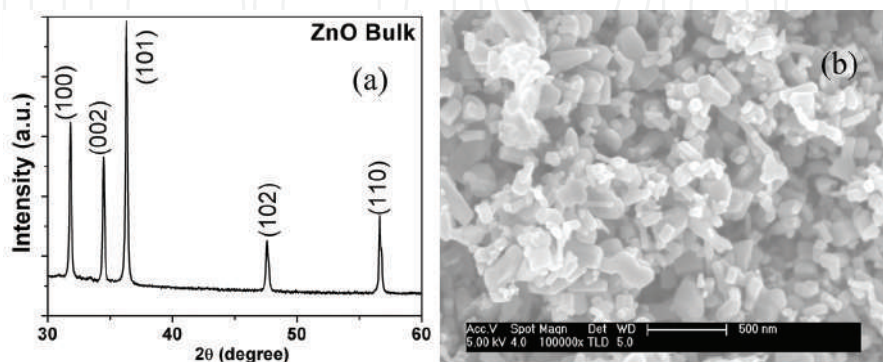


Figure 7. ZnO bulk powder (a) XRD and (b) SEM.

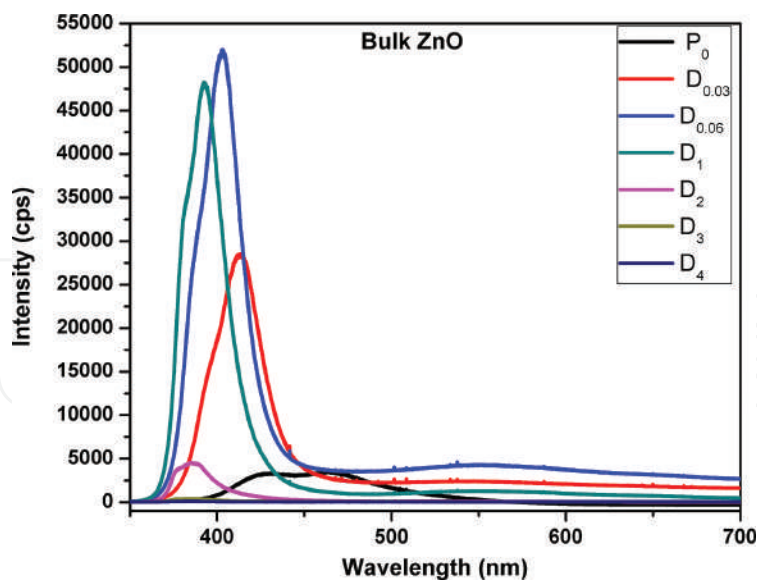


Figure 8. PL spectrum of ZnO bulk powder.

3. Discussion

PL studies show that the UV emission peak position is moved toward higher energy side (blue shift), i.e. lower wavelength side with EI decreases. The blue shift of UV emission peak is observed in all the samples irrespective of their morphology. In the PL spectra of ZnO, recently many research groups are observed that the UV emission peak intensity and peak positions varying with the excitation intensity of laser. In other words, the excitation intensity (EI) strongly influences the PL in ZnO nanostructures including nanocrystals, wires, rods, tetrapods, and ribbons [1, 7, 8, 10]. Hongwei et al. [11] studied the excitation-power dependence of the near-band-edge emission in ZnO inverse opals and nanocrystal films. Zhang et al. [8] studied the effects of excitation intensity (EI) on fluorescence spectra in various ZnO nanostructures, including tetrapod, rod, and sheet-like structures. The EI effects on PL spectra of ZnO nanostructures were explained by many authors using the UV-laser-induced heating effect/laser heating effect. Kurbanov et al. [1] explained UV-laser-induced heating effect using concept of thermal effusivity for ZnO nanocrystals grown on different substrates. In order to understand the local laser heating effects, we have assumed that the laser heating effects increase temperature in the semiconductor material (ZnO nanostructures/thin films). The rising temperature of semiconductor material due localized laser heat effects leads to the changes in optical and vibrational properties of the material [12, 13]. The phonon frequency shifts in ZnO nanostructures/thin films due to laser heating effects can be obtained using Raman spectroscopy. Raman spectroscopy is a nondestructive characterization technique, which is widely used to study the optical and vibrational properties of semiconductor materials including with thin films, hetrostructures, nanocrystals, nanowires, nanoribbons, nanorods, and tetrapods. ZnO is uniaxial crystals with wurtzite structure and it belongs to

$C_{(6\theta)}^4(P6_3mc)$ space group. Group theory predicts the existence of the following Raman modes [14]:

$$\Gamma_{opt} = A_1 + 2B_1 + E_1 + 2E_2$$

where Γ is point of the Brillouin zone and it involved in first-order Raman scattering for perfect ZnO crystals. Both A_1 and E_1 modes are polar. They split into transverse optical (A_1TO , E_1TO) and longitudinal optical (A_1LO , E_1LO) modes. E_2 is nonpolar mode consists of two modes of low- and high-frequency phonons (E_2 low, E_2 high). E_2 (high) is associated with oxygen atoms and E_2 (low) is associated with Zn sublattice [13]. These modes are Raman active according to Raman selection rule. B_1 branch is silent. The phonon frequency shifts in the Raman spectra of ZnO nanostructures are probably due to the optical phonon confinement, defects or impurities in the material, tensile strain, and laser-induced heating [13, 14]. The optical phonon confinement effect is neglected in this work because Bohr exciton radii (≈ 2.34 nm) are smaller than the nanocrystallite size of the grown ZnO nanostructure/thin films.

The PL spectra of ZnO nanostructures with the changes of EI are summarized as follows. In the case of bulk ZnO, the UV peak position moved significantly toward lower wavelength side (from 423.6 to 386.5 nm) with the range of about 37.1 nm when the EI intensity decreased from P_0 to D_4 . The intensity of UV peak is increase with EI ranging from P_0 to $D_{0.06}$, and reaches highest at $D_{0.06}$. Then the UV peak intensity decreases and reaches lowest for the D_4 . Similar behavior is observed in the case of ZnO nanorods and tetrapods. In the case of ZnO thin films, the intensity of UV peak decreases with the decreasing EI. The green emission peak position is not changed with the EI. The green band intensity is fluctuating with the EI. In other words, the changes in EI not affect by green band position, intensity, and width. Moreover, the appearance of green band in the spectrum is directly supporting the existence of oxygen vacancies or Zn interstitials in the ZnO nanostructure/film. **Figure 9** shows the Raman spectra of ZnO nanostructure/film sample excited using 514 nm laser. The spectrum of bulk ZnO exhibits one prominent peak at 439 cm^{-1} (E_2 high) in addition weak peak at 332 and 579 cm^{-1} . The nanorods also show similar spectrum. In the case of thin films, the prominent peak is observed at 438 cm^{-1} (E_2 high) and weak peaks are observed at 331 , 493 , and 577 cm^{-1} . The tetrapods of ZnO show prominent peak at 437 cm^{-1} (E_2 high) in addition to weak peaks at 330 , 376 , and 579 cm^{-1} . In all the cases, the intensity of all the Raman peaks decreases with decreasing EI. The observed values (Raman shift/peak position) are much closed to the previous reports [15, 16]. The Raman peak E_2 high ($439/438/437\text{ cm}^{-1}$ representing bulk/rods/tetrapods, respectively) is corresponding to the wurtzite phase of ZnO. The EI variation of the laser (514 nm) does not produce any change in E_2 high peak and other additional peaks position ($579/578/577\text{ cm}^{-1}$ representing bulk/rods/tetrapods, respectively). The most important peak is observed at $579/578/577\text{ cm}^{-1}$ in all the ZnO nanostructures. In general, the LO frequency modes are used to observe between 574 and 591 cm^{-1} for the relatively large size of ZnO nanocrystals. According to previous reports [17, 18], the $579/578/577\text{ cm}^{-1}$ mode is ascribed to the LO phonon of A_1 or E_1 symmetry. According to Zhang et al. [14], the peak observed at 577 cm^{-1} is a defect induced

mode in ZnO nanostructures. We believe that the 579/578/577 cm^{-1} corresponding to bulk/rods/tetrapods are defect-induced mode associated with the defects such as oxygen vacancies, zinc interstitials, and the free carrier lack [19]. In the most of the samples (see **Figure 9**), ZnO transversal modes and second order modes are absent in the spectra. This leads to understand poor crystallization quality of ZnO nanostructures.

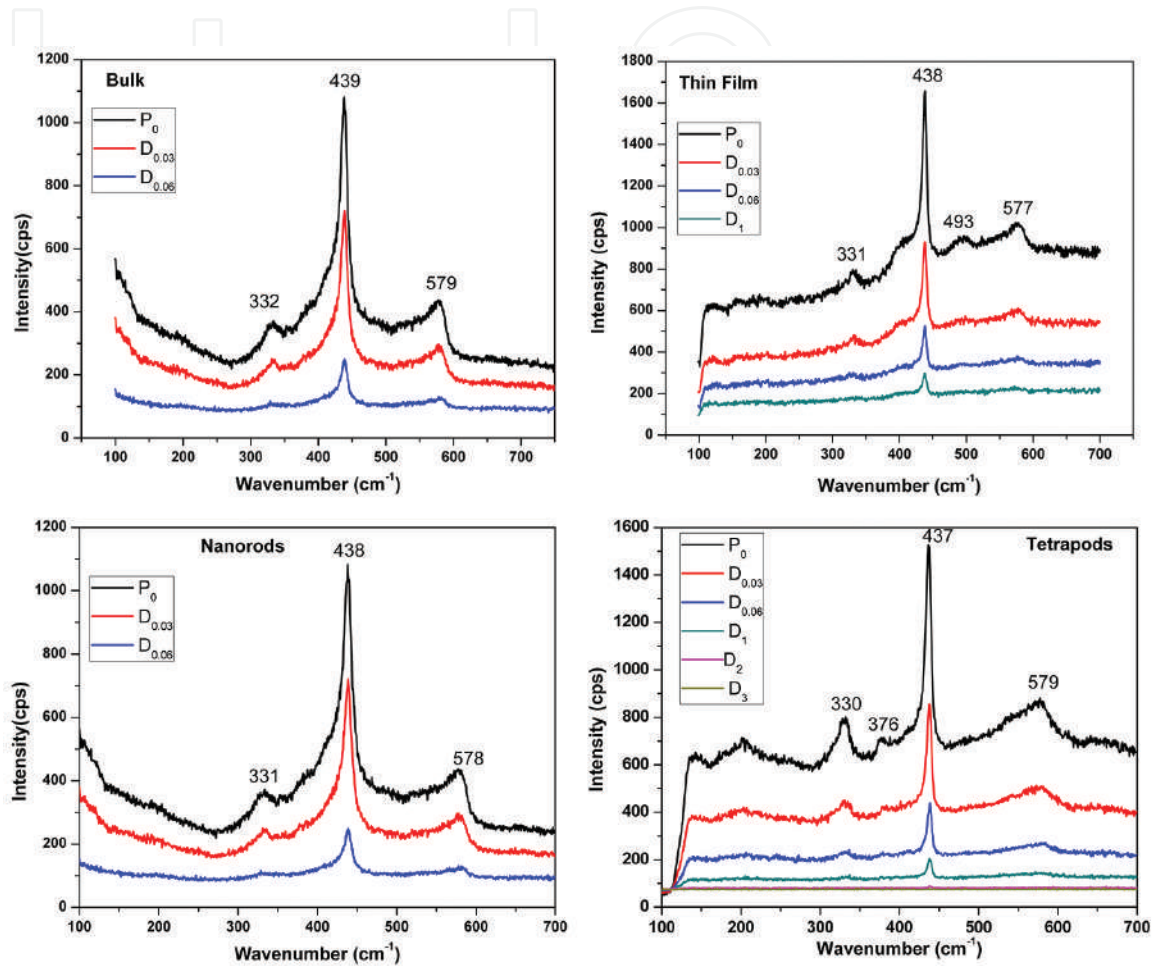


Figure 9. Raman spectrum of ZnO material for bulk, thin films, nanorods, and tetrapods.

Raman studies with 325 nm laser line are conducted on the ZnO nanostructures in order to cross check the laser heating effect because the same laser was used for the PL. The Raman spectra with 321 nm laser are shown in **Figure 10**. No E_2 (high) peak is observed. The LO mode is observed at 579/578/577 cm^{-1} for the different ZnO nanostructures. The intensity of LO is decreases with EI. Neither a blue nor a red shift is observed in LO position with a decrease in EI. According to previous report [13], the huge red shift of LO should be observed for the ZnO nanostructure when the intense local heating induced by UV laser. The observations from **Figure 10**, indirectly tells that the presence of the intrinsic impurity or defects in the sample. After careful analysis of Raman results, we understand that the huge shift of UV peak in PL may not be attributed to local heating induced by UV laser in the ZnO nanostructures. In order to verify this assumption, we recorded the PL and Raman spectra at low temperature for all

the samples using WITec Alpha SNOM instrument with solid state lasers 355 and 532 nm, respectively. We change the instrument to avoid instrumental error. Here, the PL spectrum was recorded at the maximum and minimum of laser EI. The samples were tested in the temperature range of -190 to 30°C (83 – 303 K).

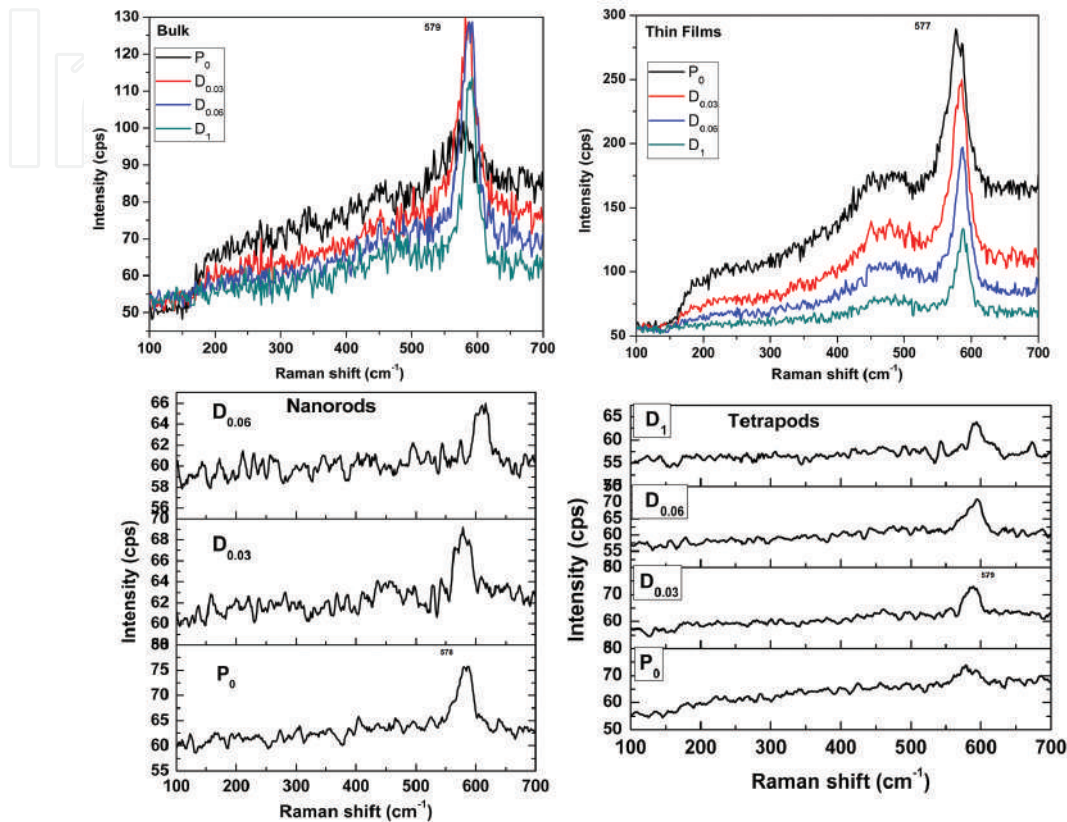


Figure 10. Raman spectrum of ZnO material with 325 nm excitation source for bulk, thin films, rods and tetrapods.

Figure 11 shows the low-temperature PL spectra. It is well known that the low-temperature PL from ZnO material with reasonably good crystalline quality is dominated by UV emission. From **Figure 11**, the origin of the UV emission peak shift explained based on the two major parameters one is laser EI the other one low-temperature variation.

From low-temperature PL, it can be argued that when the sample is in liquid nitrogen reservoir, then the reservoir temperature would be expected to compensate the local heating by laser. Hence, no-shift in the UV band (or the quenching of the UV emission) is expected. However, at liquid nitrogen temperature, the similar blue shift of UV emission has been observed for the samples (thin films, nanorods, and tetrapods) at $E(\text{max})$ and $E(\text{min})$. Moreover, we have tried to measure the surface temperature of the samples using thermocouple as well as IR thermometer during surface illumination by laser. No evidence of the increase in the surface temperature of the samples is observed. It is stated that such shift in UV emission is independent of the deposition parameter, morphology and structural parameters. The PL UV peak emission position blue shift of ZnO material can be understood from **Figure 12**.

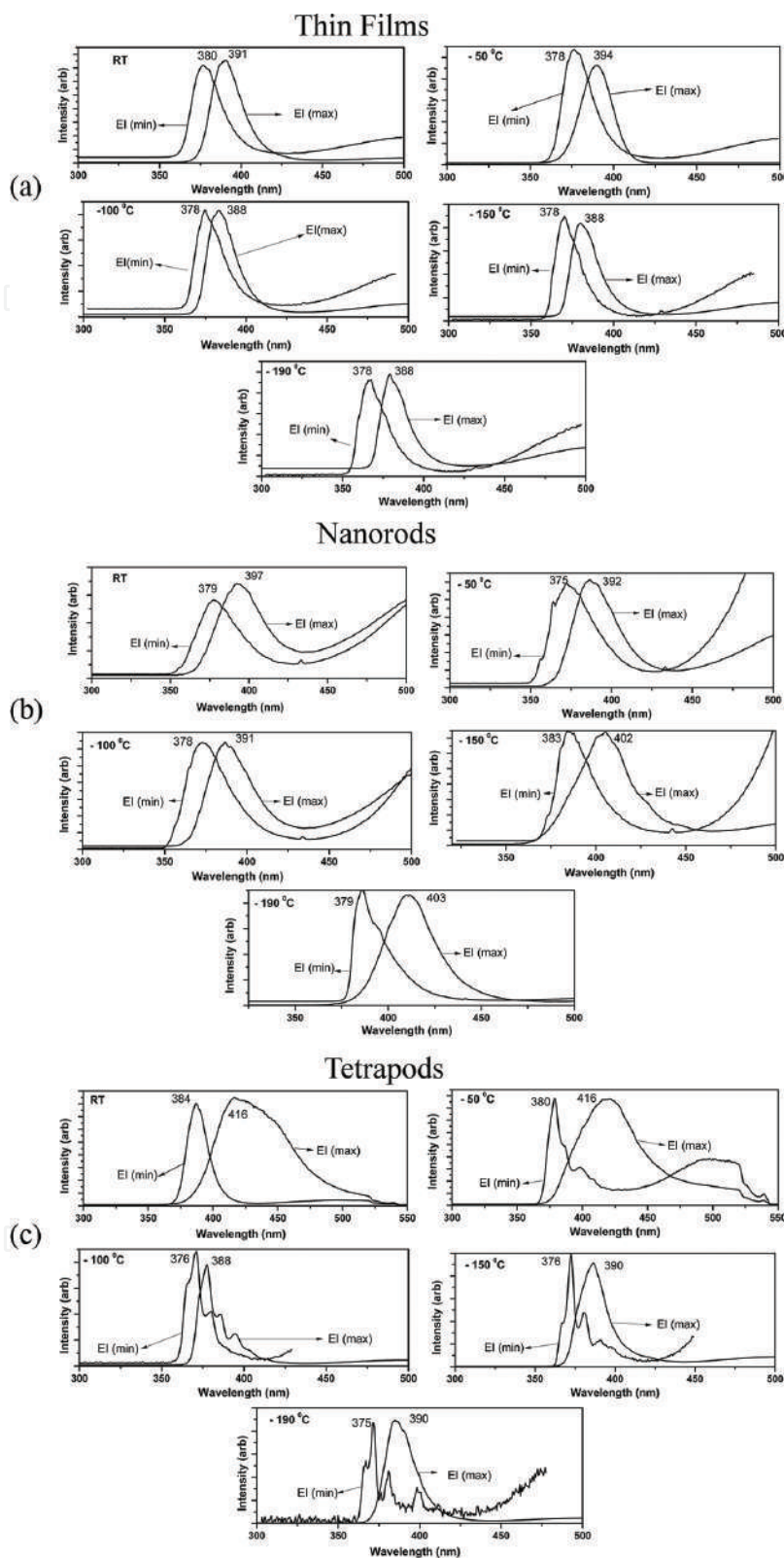


Figure 11. (a) Low-temperature PL of ZnO thin films. (b) Low-temperature PL of ZnO nanorod. (c) Low-temperature PL of ZnO tetrapods.

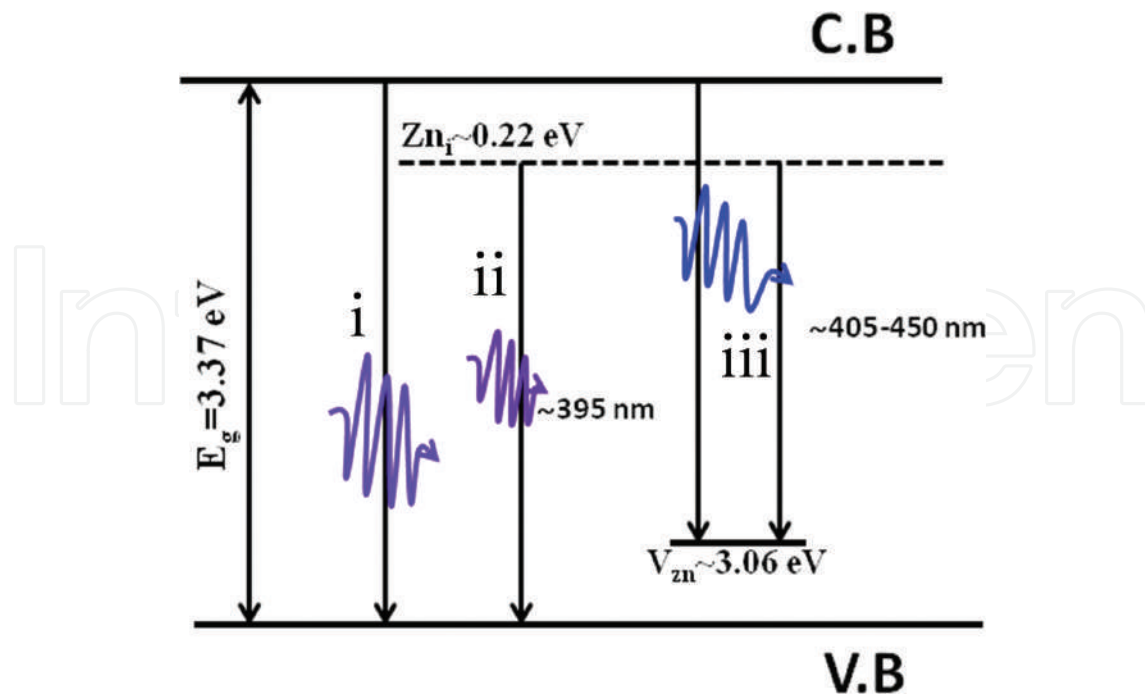


Figure 12. Energy band diagram of ZnO showing the probable transition processes [7].

After careful analysis of the RT and low-temperature PL studies, the shift in the UV emission can be due to intrinsic defect level emissions in ZnO as explained based on the energy band diagram shown in **Figure 12**. From **Figure 12**, the origin of UV emissions in ZnO are attributed to four factors. They are: (i) direct transition from conduction band (CB) to valence band (VB); (ii) transition of zinc interstitial (Zn_i) defect level to VB; (iii) transition from the CB to zinc vacancy (V_{zn}) which is a result of blue-green emission of the material; and (iv) transition from Zn_i to V_{zn} [7, 20]. It is believed that the Zn_i and V_{zn} defects are playing crucial role in the blue shift of UV emission in ZnO. According to PL results, UV emission shifts largely from 377 to 415 nm with EIs for various samples. This UV emission can be due to the transitions (i), (ii), and (iii) involved between defects levels Zn_i , V_{zn} and CB due to which shift in the band-to-band transition is observed for different EIs. Hence, it is understood from the above discussion that defect levels present in the sample may be responsible for the shifts in the UV emission band with different EIs. In this regard, all ZnO samples exhibit the A_1LO Raman band ($\sim 580\text{ cm}^{-1}$) which is ascribed to a defect induced mode [7] as evidenced from the Raman spectrum. Overall, all the samples possess considerable intrinsic defects which may be responsible for the shifts in UV emission band with EIs.

4. Conclusion

The excitation-intensity dependence of the UV emission for various ZnO samples has been studied in detail. The EI effects were studied systematically at room temperature and at liquid nitrogen temperature. It is observed that the UV emission band moves toward higher energy

side (blue shift) when the EI is decreased and vice versa both room temperature as well as at liquid nitrogen temperature. The blue shift of UV emission is only observed for some samples whereas few samples do show a marginal shift with the EI variation. These results give an implication that the shift may not be the intrinsic effect of laser-induced heating as has been claimed by other research groups; rather other mechanism can also be equally responsible. For detailed understanding, Raman measurements are methodically recorded for different EIs. The marginal shift in A_1LO modes observed for different samples with different EIs and systematic analysis of all the results supporting the shift of UV emission. It may also be attributed to the native defects in ZnO nanostructures/thin films apart from laser-induced heating. Result analysis show that the PL properties of the ZnO nanostructures/thin films are a strong function of the excitation intensity. The Raman studies helped to identify the origin of the UV emission peak shift in ZnO nanostructures. These results strongly suggest that heating effect alone cannot explain the observed excitation intensity dependency of luminescence spectra. However, further study is underway for better understanding.

Acknowledgements

The author is thankful to Dr K.K. Nanda, MRC, IISc, Dr G.K. Goswami, MRC, IISc, and Dr M.C. Santhosh Kumar, Department of Physics, NIT Tiruchirappalli for their help and discussion.

Author details

Prasada Rao Talakonda

Address all correspondence to: prasadview@gmail.com

Department of Physics, K L University, Andhra Pradesh, India

References

- [1] S.S. Kurbanov, Kh.T. Igamberdiev, T.W. Kang. The UV-laser induced heating effect on photoluminescence from ZnO nanocrystals deposited on different substrates. *J. Phys. D: Appl. Phys.* 2010;43:115401. DOI:10.1088/0022-3727/43/11/115401.
- [2] M. Kashif, S.M. Usman Ali, M.E. Ali, H.I. Abdulgafour, U. Hashim, M. Willander, Z. Hassan. Morphological, optical, and Raman characteristics of ZnO nanoflakes prepared via a sol-gel method. *Phys. Status Solidi A*, 2012;209:143–147. doi: 10.1002/pssa.201127357.

- [3] Prasada Rao Talakonda, *ZnO Thin films for Optoelectronic Applications*, LAMBERT Academic Publishing, Heinrich-Bocking-Str. 6–8, 66121 Saarbrücken, Deutschland/Germany, 2013, ISBN: 978-3-659-37010-6.
- [4] J.C. Ronfard-Haret. Electric and luminescent properties of ZnO-based ceramics containing small amounts of Er and Mn oxide. *J. Luminesc.* 2003;104:1–12. doi:10.1016/S0022-2313(02)00574-4.
- [5] Khedidja Bouzid, Abdelkader Djelloul, Nouredine Bouzid, Jamal Bougdira. Electrical resistivity and photoluminescence of zinc oxide films prepared by ultrasonic spray pyrolysis. *Phys. Status Solidi A.* 2009;206:106–115. doi: 10.1002/pssa.200824403.
- [6] D.C. Reynolds, D.C. Look, B. Jogai, J.E. Van Nostrand, R. Jones, J. Jenny. Source of the yellow luminescence band in GaN grown by gas-source molecular beam epitaxy and the green luminescence band in single crystal ZnO. *Solid State Commun.* 1998;106:701–704. doi: 10.1016/S0038-1098(98)00048-9.
- [7] T. Prasada Rao, G.K. Goswami, K.K. Nanda. Detailed understanding of the excitation-intensity dependent photoluminescence of ZnO materials: role of defects. *J. Appl. Phys.* 2014;115:213513. doi: 10.1063/1.4881779.
- [8] Zhang YuGang, Zhang LiDe, Effect of excitation intensity on fluorescence spectra in ZnO nanostructures and its origin. *Sci. China. Ser. G-Phys. Mech. Astron.* 2009;52:4–12. doi: 10.1007/s11433-009-0008-2.
- [9] T. Prasada Rao, M.C. Santhosh Kumar. Realization of stable p-type ZnO thin films using Li-N dual acceptors. *J. Alloys Compd.* 2011;509:8676–8682. doi:10.1016/j.jallcom.2011.05.094.
- [10] S. Dhara, P.K. Giri. Rapid thermal annealing induced enhanced band-edge emission from ZnO nanowires, nanorods and nanoribbons. *Funct. Mater. Lett.* 2011;4:25–29. doi: 10.1142/S1793604711001658.
- [11] Hongwei Yan, Yingling Yang, Zhengping Fu, Beifang Yang, Jian Zuo, Shengquan Fu. Excitation-power dependence of the near-band-edge photoluminescence of ZnO inverse opals and nanocrystal films. *J. Luminesc.* 2008;128:245–249. doi: 10.1016/j.jlumin.2007.08.002.
- [12] E. Alarcon-Liado, J. Ibanez, R. Cusco, L. Artus, J.D. Prades, S. Estrade, J.R. Morante, Ultraviolet Raman scattering in ZnO nanowires: quasimodemixing and temperature effects. *J. Raman Spectrosc.* 2011;42:153–159. Doi: 10.1002/jrs.2664.
- [13] K.A. Alim, V.A. Fonoberov, M. Shamsa, A.A. Balandin. Micro-Raman investigation of optical phonons in ZnO nanocrystals. *J. Appl. Phys.* 2005;97:124313. doi: 10.1063/1.1944222.
- [14] R. Zhang, P.G. Yin, N. Wang, L. Guo. Photoluminescence and Raman scattering of ZnO nanorods. *Solid State Sci.* 2009;11:865–869. doi: 10.1016/j.solidstatesciences.2008.10.016.

- [15] S.K. Panda, C. Jacob. Surface enhanced Raman scattering and photoluminescence properties of catalytic grown ZnO nanostructures. *Appl. Phys. A*. 2009;96:805–811. doi: 10.1007/s00339-009-5309-9.
- [16] I. Calizo, K.A. Alim, V.A. Fonoberov, S. Krishnakumar, M. Shamsa, A.A. Balandin, R. Kurtz. Micro-Raman spectroscopic characterization ZnO quantum dots, nanocrystals, and nanowires. *Proc. SPIE*. 2007;6481:64810N. doi: 10.1117/12.713648.
- [17] K.A. Alim, V.A. Fonoberov, A.A. Balandin. Origin of the optical phonon frequency shifts in ZnO quantum dots. *Appl. Phys. Lett.* 2005;86:053103. doi: 10.1063/1.1861509.
- [18] Y. Yang, H. Yan, Z. Fu, B. Yang, J. Zuo. Correlation between 577 cm^{-1} Raman scattering and green emission in ZnO ordered nanostructures. *Appl. Phys. Lett.* 2006;88:191909. doi: 10.1063/1.2202741.
- [19] C. Xu, G. Xu, Y. Liu, G. Wang. A simple and novel route for the preparation of ZnO nanorods. *Solid. State. Commun.* 2000;122:175–179. doi:10.1016/S0038-1098(02)00114-X.
- [20] A.N. Mallika, A. Ramachandra Reddy, K. Sowribabu, K. Venugopal Reddy. Structural and optical characterization of $\text{Zn}_{0.95-x}\text{Mg}_{0.05}\text{Al}_x\text{O}$ nanoparticles. *Ceram. Int.* 2015;41:9276–9284. doi:10.1016/j.ceramint.2015.03.096.

IntechOpen

We are IntechOpen, the world's leading publisher of Open Access books Built by scientists, for scientists

6,300

Open access books available

171,000

International authors and editors

190M

Downloads

Our authors are among the

154

Countries delivered to

TOP 1%

most cited scientists

12.2%

Contributors from top 500 universities



WEB OF SCIENCE™

Selection of our books indexed in the Book Citation Index
in Web of Science™ Core Collection (BKCI)

Interested in publishing with us?
Contact book.department@intechopen.com

Numbers displayed above are based on latest data collected.
For more information visit www.intechopen.com



Photon-Upconverting Materials: Advances and Prospects for Various Emerging Applications

Manoj Kumar Mahata, Hans Christian Hofsäss and Ulrich Vetter

Additional information is available at the end of the chapter

<http://dx.doi.org/10.5772/65118>

Abstract

Rare-earth-doped upconversion materials, featuring exceptional photophysical properties including long lifetime, sharp emission lines, large anti-Stokes shift, low autofluorescence of the background, and low toxicity, are promising for many applications. These materials have been investigated extensively since the 1960s and employed in many optical devices. However, due to rapid development of synthesis strategies for nanomaterials, upconversion materials have been rehighlighted on the basis of nanotechnology. Herein, we discuss the recent advances in upconversion materials. We start by considering energy transfer processes involved in the basic study of upconversion emission phenomena, as well as synthesis strategies of these materials. Progress in different energy transfer processes, which play an important role in determining luminescence efficiency, is then discussed. Newer applications of these materials have been vastly reviewed.

Keywords: upconversion, luminescence, rare earth, 4f-4f transitions, nanomaterials, energy transfer, optical applications, nanophosphor

1. Introduction

Photon upconversion (UC) is a nonlinear optical process which yields high-energy photons through sequential absorption of two or more low-energy photons. The concept of UC was conceived by physicist N. Bloembergen [1] in 1959 to develop an infrared (IR) photon detector for counting infrared photons through the interaction of infrared (IR) photons with rare earth (RE) or transition-metal ions incorporated in crystalline materials. Though, due to the lack of

coherent pumping sources, the prospect of achieving upconversion was not possible. With the advances in lasers and optical technology, the landmark experiment to observe IR to visible upconversion was reported first time by F. Auzel [2] in 1966 and explained energy transfer in $\text{Er}^{3+}\text{-Yb}^{3+}$ and $\text{Tm}^{3+}\text{-Yb}^{3+}$ systems. Since then, research on photon upconversion has inspired the design of near-infrared (NIR) to visible upconverter suitable for a wide range of applications. Later, technological advances in laser and optical tools compelled the application of upconversion lasers for converting low-energy laser radiation to high-energy laser radiation [3]. However, in early days, applications of UC materials in biomedical fields were not clear [4]. One of the major challenges was to control the size and shape of the materials that are suitable in biological environments.

Rare earth elements, including scandium and yttrium, are important in functional materials due to their similar electronic configurations ($[\text{Xe}]4f^{n-1}5d^0-16s^2$). Because of this, they have similar physical and chemical properties in their trivalent ionic state. The energy levels of RE^{3+} from the 4f electronic configuration are abundant and thus allow for many intraconfigurational transitions (**Figure 1**). The intra-4f transitions are forbidden for free RE ions but these rules are partially broken when the REs are embedded in an inorganic lattice. Owing to many energy levels with intraconfigurational transitions, RE-ions act as promising luminescent centers. Moreover, the intrinsic character of RE ions due to shielding of partially filled 4f electrons by completely filled $5s^25p^6$ subshells makes them less sensitive to the environment of the host lattice. Apart from this, long life, sharp emission lines, large anti-Stokes shift, and photostability are the results of their unique 4f energy levels.

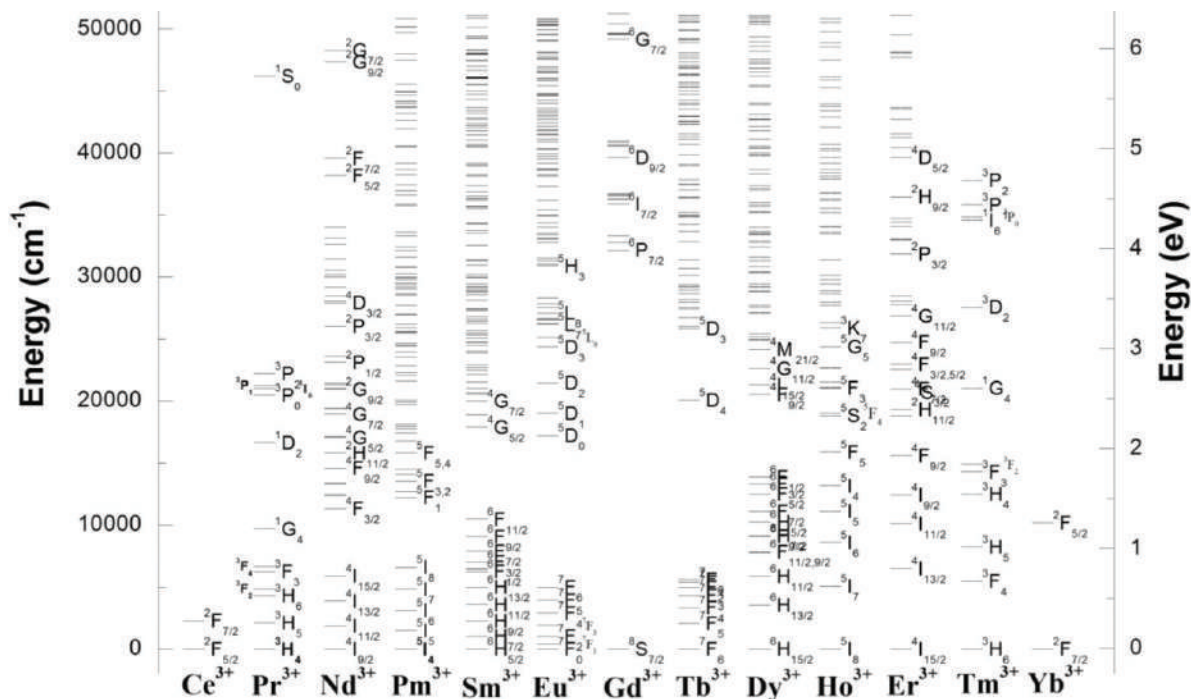


Figure 1. The 4f energy level diagrams, computed using the mean free ion parameters described in Ref. [5]. The levels were cut at $52,000\text{ cm}^{-1}$.

In recent decades, UC materials have attracted much attention because of their special spectroscopic properties [6]. RE-doped luminescent materials have been employed in display devices and solid state lasers for long time. With the development of new synthesis strategies, RE-doped UC materials can be prepared at nanoscale for better prospects [3]. The emission bands of UC nanomaterials are less affected by the particle size unlike quantum dots, whose luminescence is dependent on particle size. Moreover, owing to their high resistance to photobleaching, photoblinking, specific NIR excitation, excellent penetration depth in biosystems without any autofluorescence from the background, UC particles have a wide range of applications in bioimaging and theranostics [7]. In spite of these features, several aspects of the UC nanomaterials are of great concern, such as enhancing UC efficiency, color outputs, and manipulation of energy transfer pathways to achieve desired UC emissions for specific applications.

Here, we review the recent advances in photon-upconverting materials. In this chapter, we discuss the composition of ideal UC materials, synthesis of UC particles, physics of UC followed by their applications and future prospects.

2. Composition of upconversion materials

Upconverting particles are generally composed of a host material doped with optically active sensitizer and activator ions [8]. Controlling the energy transfer processes among these three constituents is of great importance in selecting suitable dopant-host pairs. The host matrices differ in their coordination numbers, distances between dopants, and efficiencies of energy transfer. Thus proper selection of the host matrix is of significant importance. Host matrices must possess low-phonon energies to avoid degradation of efficiency through nonradiative relaxations and should be chemically and thermally stable. Moreover, host materials should have high tolerance for sensitizer and activator ions and high transparency for free migration of NIR photons in the lattice. Fluoride materials meet these criteria and are popular choices as host matrices for UC materials [8]. Among the reported host matrices, the NaREF₄ series has been proven to be highly effective due to their lower phonon energy and excellent chemical stability. In this family, the hexagonal-NaREF₄ series is more efficient than the cubic-NaREF₄ series due to its unique crystal structure. Oxide materials such as ZrO₂, Y₂O₃, vanadates (e.g., YVO₄, GdVO₄), phosphates (e.g., LuPO₄, YPO₄) are also examples of some common host materials because of their high chemical stability, even though they have larger phonon energies than the fluoride materials [6, 8].

The role of sensitizers is to sensitize the activators in the UC materials. An ideal sensitizer should have large absorption cross-section at the desired excitation wavelength and resonant energy levels to those of the activators, with suitable excited energy state located in the NIR region. Among all the RE ions, Yb³⁺ is the best choice as a sensitizer. The absorption cross-section of Yb³⁺ is $9.11 \times 10^{-21} \text{ cm}^{-2}$ at 980 nm, which is relatively large among RE ions [9]. Moreover, the energy level diagram of Yb³⁺ has only one excited state (²F_{5/2}) that matches very well with the f-f transitions of many RE activators, e.g., Er³⁺, Ho³⁺, Tm³⁺, etc. and therefore Yb³⁺

is an excellent sensitizer to transfer energy to other RE ions. For example, the $^2F_{5/2}$ state of Yb^{3+} overlaps the $^4I_{11/2}$ state of Er^{3+} , allowing Yb to Er energy transfer (**Figure 1**).

UC emission increases with doping concentration of activator ions until a critical concentration. Beyond that concentration, quenching among activator ions occurs and decreases the upconversion emission [10]. To get rid of this problem, concentrations of activators are kept low while one or more types of RE ions with high concentration are incorporated as sensitizers. The activators should possess a large number of metastable energy levels. Once ground state electrons are excited to the metastable state, activators are likely to accept energy from nearby sensitizers to be excited at higher excited states. The energy levels of the activators should not be close enough to promote nonradiative relaxations. According to the energy level structures, Er, Tm, and Ho ions in their trivalent state are ideal to minimize nonradiative relaxations, whose transition rate decreases exponentially with increasing energy gap.

3. Synthesis of upconversion materials

In order to achieve high UC efficiency, synthesis of UC materials is very crucial. Recently, various methods have been developed for synthesizing RE-doped UC materials, including thermal decomposition, coprecipitation, hydrothermal, sol-gel, combustion, microwave, microemulsion, and so on [11–20]. The methods are to address specific requirements such as surface modification and monodispersity. The synthesis routes are not mutually exclusive, and often more than one method is combined to produce the suitable UC particles. Some important synthesis processes for preparing UC particles are discussed below.

3.1. Thermal decomposition

Thermal decomposition gives size-controlled well-shaped particles within short reaction time [11]. It usually involves surfactant-assisted decomposition of precursors in high-boiling organic solvents. Then the generated ions are combined into new nuclei at relatively high temperature. The trifluoroacetate and oleate compounds are commonly used organic precursors and polar capping groups such as oleic acid, oleylamine and octadecene are usually used as surfactants. It is believed that the solvents can control the growth of the particles via capping the surface of UC particles. A systematic investigation on the growth mechanism of UC nanocrystals was performed by Mai et al. [12] and inferred the passage of precursors in surfactant solutions through a slow nucleation pathway. They also showed that various sizes and shapes of Er^{3+}/Yb^{3+} doped $NaYF_4$ particles can be obtained by varying reaction time, reaction temperature, and concentration of reagents. Though this method has several important advantages, e.g., strong UC emission, high quality of products and pure phase crystals, it suffers from some disadvantages including operation difficulty, production of toxic materials, and presynthesis of $RE(CF_3COO)_3$ precursors.

3.2. Coprecipitation

The coprecipitation method is developed to overcome the limitations of the thermal decomposition method and considered as a significant method for synthesis of UC particles. It involves the precipitation of two substances simultaneously. In the coprecipitation route, UC nanocrystals are formed with organic surfactants and prevent agglomeration through their adsorption to the surface of the particles [6]. The benefits of the coprecipitation method include absence of toxic by-products, inexpensive equipment, and simple procedure. $\text{Er}^{3+}/\text{Yb}^{3+}$, $\text{Ho}^{3+}/\text{Yb}^{3+}$, and $\text{Tm}^{3+}/\text{Yb}^{3+}$ doped LaF_3 nanoparticles [13] with particle size of 5 nm were prepared by Yi et al. In addition to that, RE-doped LuPO_4 , YbPO_4 , NaYF_4 , NaGdF_4 , and $\text{Y}_3\text{Al}_5\text{O}_{12}$ (YAG) nanoparticles were also produced using this method. Recently, our group has synthesized the $\text{Er}^{3+}/\text{Yb}^{3+}$ doped BaTiO_3 [14] and YVO_4 [15] nanocrystals using the coprecipitation method. Despite the general advantages, this method suffers from the long-time operation of the experimental procedure, which sometimes takes more than 8 h. Moreover, to produce UC particles in industrial scales, this method is not suitable.

3.3. Hydrothermal

Thermal decomposition can only use organic solvents while hydrothermal synthesis which is mainly a solution-based method, can occur in a water-based system with low reaction temperature (around 200°C) in a relatively environment friendly condition [11]. Hydrothermal methods involve heating of the solvent at high pressure above its critical point. This process is convenient to produce controllable size and shape of the inorganic nanoparticles with diverse nanodimensional architectures. For example, yttrium orthovanadate (YVO_4) crystals have been prepared hydrothermally in both acidic and basic media with well-defined microcrystals with clear facets and dispersed nanograins and nanoflakes within 5–50 nm dimension [16]. Prism, disk, rod, and tube like NaYF_4 crystals were prepared by hydrothermal method [17]. An advantage of this route is that experimental parameters such as reaction temperature, reaction time, solvent type, and surfactant type can be varied to control the size and shape of the synthesized particles.

3.4. Sol-gel

The sol-gel method is generally used for the preparation of thin films, oxides, and fluoride nanocrystals [11]. The method is a typical wet-chemical process, starts with liquid solution of molecular precursors and it forms a new sol phase through hydrolysis and polycondensation reactions. With the addition of base, the sol is agglomerated into gel through a large macromolecular network, followed by annealing at high temperature for a few hours. Annealing increases crystallinity and removes the solvents from the gel. Patra et al. [18] prepared Er^{3+} doped TiO_2 and BaTiO_3 using basic acetate and titanium tetraisopropoxide. Patra et al. [19] developed the sol-gel method into sol emulsion-gel method to synthesize $\text{ZrO}_2:\text{Er}^{3+}$ nanoparticles. A thin film of $\text{YVO}_4:\text{Eu}^{3+}$ was fabricated by Cheng et al. [20] through the combination of pechini-type sol-gel method and inkjet printing. The key step in a sol-gel process is the annealing procedure. The quality of the synthesized materials is significantly dependent on the annealing temperature and time. The materials produced via sol-gel method yield high

UC intensity and the method can be applied for production on a large scale. However, there are some shortcomings in this process. For instance, the derived particles are of irregular shapes, sizes, and are not water-soluble.

3.5. Combustion

Compared to thermal decomposition, hydrothermal, and sol-gel methods, combustion synthesis is a high-throughput method of producing UC particles within a very short period of time [7]. A balanced mixture of reducing agent (fuel) and oxidizers (metal nitrates) is usually selected for the reaction to release maximum energy during the reaction time. In this process, a series of controlled explosions take place in the reaction materials in a self-sufficient condition without requiring any extra heat for the total reaction. Generally, the oxide and oxysulfide materials are prepared through this technique. Some reports on producing RE-doped Y_2O_3 , La_2O_2S , Gd_2O_3 , and $Gd_2Ga_5O_{12}$ can be found in the literature [6, 11]. One should keep in mind that the fuel and nitrates are chosen so that they do not produce toxic gases and the reaction should be relatively mild. However, combustion synthesis is a readily scalable, time and energy-saving, low cost, and efficient process that can be extended for commercial purpose.

4. Physics of upconversion

4.1. Upconversion mechanisms

Several mechanisms have been identified to be involved in UC process either alone or in combination [3, 4, 6, 10]. Though much work has been performed to know the energy transfer processes during UC event, only the basic possibilities, namely excited state absorption (ESA), energy transfer UC (ETU), photon avalanche (PA), cooperative UC (CUC), and energy migration-mediated UC (EMU) are given here. **Figure 2** depicts the basic UC processes.

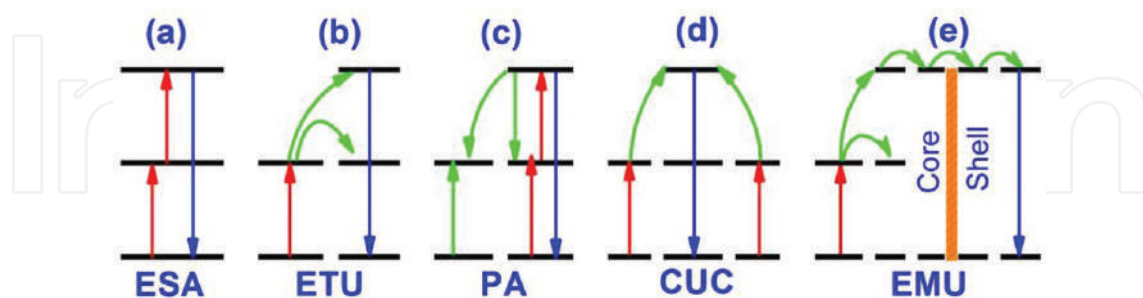


Figure 2. Simplified energy level diagrams describing upconversion processes: (a) ESA, (b) ETU, (c) PA, (d) CUC, and (e) EMU (red: excitation; blue: UC emission; green: energy transfer).

An ESA (**Figure 2a**) process refers to multistep excitation by sequential absorption of one or more low-energy photons from the ground state to intermediate state, and finally populates the intermediate state, from which upconversion emission occurs. The absorption cross-section of the excited ion should have the capability of absorbing the second pump photon. The ESA

process generally occurs at low doping concentration (<1%) of the activator ions, as high doping concentration is likely to degrade the UC emission via nonradiative relaxation processes. Although the ESA process occurs in single RE ions, its efficiency is strongly suppressed due to weak absorption induced by parity-forbidden 4f-4f transitions within RE ions.

The ETU process (**Figure 2b**) is more efficient than ESA and it involves two types of luminescent centers—sensitizer and activator ions. Once the sensitizer is excited, it transfers energy to the nearest activator ion and UC emission is obtained from the activator when it drops back to the ground state or lower excited state. For sufficient energy transfer, the activator and sensitizer should possess resonant energy levels with closeness in spatial distance between them. Because of resonant energy absorption, the excitation lifetime is longer and probability of UC is higher which makes this process an efficient one.

The PA process (**Figure 2c**) is more complex than the ESA and ETU and only occurs after a critical level of pump density. The PA process was first proposed in 1979 using Pr³⁺ ion-based infrared quantum counter. If the pump density is sufficiently high, the intermediate reservoir level of many ions becomes populated initially by a nonresonant ground state absorption process, followed by resonant ESA or ETU from another excited ion to populate the UC emitting level. After this stage efficient cross relaxation takes place between excited and ground-state ions. As a result, population of the reservoir level and the UC emitting level increases and causes an “avalanche” effect of generating more excited ions through feedback looping, making this process the most efficient.

The CUC process (**Figure 2d**) is similar to ETU process and includes two types of luminescent centers—sensitizer and activator. In this process the UC emitting level of the activator is populated via cooperative energy transfer from two adjacent sensitizers. The basic difference between ETU and CUC is that in CUC the activator does not have adequate long-lived intermediate energy levels compatible to that of the sensitizers. CUC occurs mainly in Yb³⁺/RE³⁺ doped UC materials, where Yb³⁺ acts as cooperative sensitizer. The efficiency of CUC is lower than that of the ETU.

Based on energy transfer within NaGdF₄:Yb³⁺,Tm³⁺@NaGdF₄:Ln³⁺ (Ln = Tb, Eu, Dy, and Sm) core-shell nanostructures, the EMU process (**Figure 2e**) was first proposed by Liu and coworkers [21] in 2011. The EMU process involves four types of luminescent centers, namely sensitizer, accumulator, migrators, and activator. The sensitizer/accumulator and the activator are confined in separate layers of the core-shell and connected by migrators [10]. The sensitizer first excited by ground state absorption and transfers its energy to an accumulator, promoting it to higher excited state. The accumulator should possess energy levels with longer lifetimes to accept the energy from the sensitizer. Then, energy migration takes place from higher excited state of accumulator to migrator, followed by migration of the excitation energy through the migrators via core-shell interface [10]. Finally, the migrated energy is trapped by an activator in the shell and emits UC luminescence.

4.2. Excited-state dynamics

The excited-state dynamics of RE ions involved in UC processes has been extensively investigated in several bulk materials and most of these are also applicable to their equivalent nanoscale systems. Quantitatively, the UC process can be described by a set of rate equations [4, 10] by taking into account all the population and depopulation pathways involved in the concerned system.

$$\frac{dN_i}{dt} = \sum \text{population rate} - \sum \text{depopulation rate}$$

As an example of establishing rate equations, the rate equations for UC process upon 980 nm light excitation in $\text{Er}^{3+}\text{-Yb}^{3+}$ system are discussed below [22].

As the absorption cross-section of Yb^{3+} is much larger than that of Er^{3+} at 980 nm excitation wavelength, it is reasonable to consider the energy transfer from Yb^{3+} to Er^{3+} [9]. The three possible energy ETU processes from Yb^{3+} to Er^{3+} are the following (refer to **Figure 3**):

- (a) ETU-1: ${}^2F_{5/2}(\text{Yb}^{3+}) + {}^4I_{15/2}(\text{Er}^{3+}) \rightarrow {}^2F_{7/2}(\text{Yb}^{3+}) + {}^4I_{11/2}(\text{Er}^{3+})$
- (b) ETU-2: ${}^2F_{5/2}(\text{Yb}^{3+}) + {}^4I_{11/2}(\text{Er}^{3+}) \rightarrow {}^2F_{7/2}(\text{Yb}^{3+}) + {}^4F_{7/2}(\text{Er}^{3+})$
- (c) ETU-3: ${}^2F_{5/2}(\text{Yb}^{3+}) + {}^4I_{13/2}(\text{Er}^{3+}) \rightarrow {}^2F_{7/2}(\text{Yb}^{3+}) + {}^4F_{9/2}(\text{Er}^{3+})$

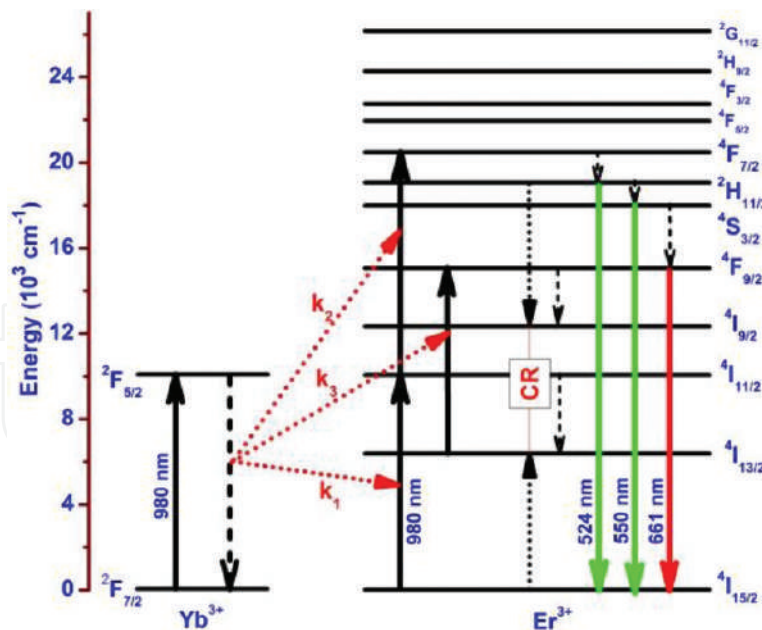


Figure 3. Energy transfer processes relevant for upconversion in $\text{Er}^{3+}\text{-Yb}^{3+}$ system [22].

The Er^{3+} ions raised to the ${}^4F_{7/2}$ level by ETU-2 relaxes nonradiatively to the ${}^2H_{11/2}/{}^4S_{3/2}$ levels and subsequently, radiative transition to the ground state (${}^4I_{15/2}$) yields green UC emission bands. Possible mechanisms for population of the ${}^4I_{13/2}$ level of Er^{3+} are (i) energy back-transfer:

${}^2\text{H}_{11/2}/{}^4\text{S}_{3/2} (\text{Er}^{3+}) + {}^2\text{F}_{7/2} (\text{Yb}^{3+}) \rightarrow {}^4\text{I}_{13/2} (\text{Er}^{3+}) + {}^2\text{F}_{5/2} (\text{Yb}^{3+})$ and (ii) cross-relaxation process of Er^{3+} ions: ${}^2\text{H}_{11/2}/{}^4\text{S}_{3/2} + {}^4\text{I}_{15/2} \rightarrow {}^4\text{I}_{9/2} + {}^4\text{I}_{13/2}$.

The rate equations for Er^{3+} - Yb^{3+} codoped system are as follows:

$$\begin{aligned} \frac{dN_{Er,1}}{dt} &= W_2 N_{Er,2} + C_{40} N_{Er,4} N_{Er,0} - k_3 N_{Er,1} N_{Yb,1} - W_1 N_{Er,1} - \rho_P \sigma_{13} N_{Er,1} \\ \frac{dN_{Er,2}}{dt} &= k_1 N_{Er,0} N_{Yb,1} + \rho_P \sigma_{02} N_{Er,0} - k_2 N_{Er,2} N_{Yb,1} - W_2 N_{Er,2} - \rho_P \sigma_{24} N_{Er,2} \\ \frac{dN_{Er,3}}{dt} &= k_3 N_{Er,1} N_{Yb,1} + \rho_P \sigma_{13} N_{Er,1} + W_4 N_{Er,4} - W'_3 N_{Er,3} \\ \frac{dN_{Er,4}}{dt} &= k_2 N_{Er,2} N_{Yb,1} + \rho_P \sigma_{24} N_{Er,2} - W_4 N_{Er,4} - W'_4 N_{Er,4} - C_{40} N_{Er,4} N_{Er,0} \\ \frac{dN_{Yb,1}}{dt} &= \rho_P \sigma_{Yb} N_{Yb,0} - (k_1 N_{Er,0} + k_2 N_{Er,2} + k_3 N_{Er,1}) N_{Yb,1} - W_{Yb} N_{Yb,1} \end{aligned}$$

where $N_{Er,i}$ ($i = 0, 1, 2, 3, 4$) are the population densities of ${}^4\text{I}_{15/2}$, ${}^4\text{I}_{13/2}$, ${}^4\text{I}_{11/2}$, ${}^4\text{F}_{9/2}$ and ${}^2\text{H}_{11/2}/{}^4\text{S}_{3/2}$ levels of Er^{3+} . $N_{Yb,i}$ ($i = 0, 1$) are the population densities of the ${}^2\text{F}_{7/2}$ and ${}^2\text{F}_{5/2}$ levels of Yb^{3+} . W_1 , W_2 , and W_4 are the nonradiative decay rates of the ${}^4\text{I}_{13/2}$, ${}^4\text{I}_{11/2}$, and ${}^2\text{H}_{11/2}/{}^4\text{S}_{3/2}$ states, respectively; W'_3 and W'_4 are the radiative decay rates of the ${}^4\text{F}_{9/2}$ and ${}^2\text{H}_{11/2}/{}^4\text{S}_{3/2}$ states, respectively. The W_{Yb} is the radiative decay rate of the excited ${}^2\text{F}_{5/2}$ state of the Yb^{3+} ion. The k_1 , k_2 , and k_3 are the energy transfer rates of ETU-1, ETU-2, and ETU-3, respectively. The C_{40} is the cross-relaxation rate for ${}^2\text{H}_{11/2}/{}^4\text{S}_{3/2} + {}^4\text{I}_{15/2} \rightarrow {}^4\text{I}_{9/2} + {}^4\text{I}_{13/2}$; σ_{ij} is the absorption cross-section between levels i and j of Er^{3+} ; σ_{Yb} is the absorption cross-section between levels ${}^2\text{F}_{5/2}$ and ${}^2\text{F}_{7/2}$ of Yb^{3+} and ρ_P is the pump constant which is proportional to the incident pump power, I_p . If the absorption cross-section of Er^{3+} is low compared to that of Yb^{3+} at 980 nm, the contribution of ground state absorption and ESA processes of Er^{3+} states can be neglected in comparison to the ETU (by Yb^{3+}) and relevant terms can be excluded from the rate equations. The energy transfer rates can be calculated using Judd-Ofelt theory [23, 24]. The multiphonon nonradiative relaxation rates can be derived using the modified energy gap law [4]. Once the transition rates are known, the characteristics of UC, namely, luminescence lifetime, spectral ratios, and quantum yields can be determined by solving these rate equations.

The rate equation model for UC process is generally made for theoretical analysis, but only very few reports are available on the use of this approach in UC nanomaterials mainly due to the complex nature of the involved UC process at the nanoscale and most of the spectroscopic characteristics of UC nanoparticles are determined experimentally. The investigation into the

time-resolved photoluminescence behavior of UC emissions is often used to check the validity of the proposed model of UC processes, and the rate constants are extracted from the fittings [10]. The lifetime of the activator's excited state is shorter than those of the sensitizers. The ETU processes lengthen the lifetime of the activators due to energy transfer from the sensitizers. Thus, the apparent lifetime of the activators is dependent on the sensitizers. The measured lifetime in UC luminescence and downconversion luminescence (the excited states are directly excited) is different. However, in the nanomaterials several factors such as surface quenching effect, particle size, and surface structure affect the lifetime and deviate from the theoretical value. The UC process shows pump power-dependent UC luminescence due to its nonlinear character. The combination of pump power dependent of UC with the steady-state rate equations yields useful information on the UC kinetics. Theoretical models proposed by Pollnau et al. and Suyver et al. [25, 26] are used vastly to know the nature of UC, i.e., the number of photons absorbed in the UC processes. The UC emission intensity (I) is proportional to n th orders of the pump power density (P): $I \propto P^n$, where ' n ' is the number of photons absorbed in the particular UC process. Thus, the slope of the plot of $\ln[I]$ vs. $\ln[P]$ reveals the nature of the UC process. The pump power dependence of the UC emission is valid in low power density and becomes complicated at high pump power due to the competition between linear decays and UC processes. In most of the cases, the slope value decreases with increasing excitation power and at very high pump power, the UC processes sometimes become pump independent due to saturation of some intermediate levels.

4.3. Photophysical processes

Basic understanding of the main photophysical processes of UC emission is necessary not only for design and optimization of performance of UC materials but also the proper interpretation of experimental results. Although the three major steps photon absorption, subsequent energy transfer, and emission of UC are key processes, various nonradiative processes that compete with the radiative processes play vital roles in determining UC efficiency. Luminescence intensities are connected to the quantum-mechanical transition rates that depend on the details of the energy states that take part for the particular UC emission. The details of the initial and final states involved in the UC emission can be determined by Judd-Ofelt theory [23, 24]. This theory is based on the approximation that all the Stark manifolds have equal population and the host matrix element is isotropic. This approach facilitates to estimate the radiative rates for RE^{3+} ions theoretically by using the experimental parameters of optical absorption or emission spectra. The radiative decay rate, W_{rad} (photons/s) for an electric dipole allowed transition between two manifolds of RE^{3+} ion can be described as [10]:

$$W_{rad} = \frac{4e^2\omega^3}{3\hbar c^3} \frac{1}{2J+1} n \left(\frac{n^2+2}{3} \right)^2 \sum_{\lambda=2,4,6} \Omega_{\lambda} |\langle SLJ || U^{(\lambda)} || S'L'J' \rangle|^2$$

where $|SLJ\rangle$ and $|S'L'J'\rangle$ are the initial and final states of the transition, respectively. e , ω , \hbar , c , and n are the electronic charge, average angular frequency of the optical transition, reduced Planck constant, speed of light, and refractive index, respectively. $[(n^2+2)/3]^2$ is the Lorentz local field

correction factor, and $(2J + 1)$ is the degeneracy manifold of the initial state. $|\langle SLJ || U^{(\lambda)} || SL'J' \rangle|^2$ are the squared matrix elements of the electric dipole operator between the initial and final manifolds. The Ω_λ ($\lambda = 2, 4, 6$) are Judd–Ofelt parameters that can be obtained from the optical absorption characterization of the material and give the influence of the host matrix on the electric dipole transition probabilities. In order to understand the UC mechanism involving 4f electrons more precisely, the magnetic dipole transitions which are weakly affected by the crystal field of the host should be combined to the Judd–Ofelt rates. With magnetic dipole transitions factored in, the Hamiltonian of a free ion (RE^{3+}) can be treated in quantifying the magnetic part of the UC emission in RE^{3+} .

Within a sensitizer-activator pair, the excitation energy of the sensitizer is transferred resonantly to adjacent activator. The resonant energy transfer process may be radiative or nonradiative. The nonradiative energy transfer takes place via long-range dipole-dipole interactions while the former one requires emission and reabsorption of a photon [10]. According to Dexter’s theory [27], the resonant energy transfer probability W_{SA} between the sensitizer and activator ions can be expressed using the spectral overlap of the emission of sensitizer and absorption of activator. The energy transfer probability is given by [3]:

$$W_{SA} = \frac{3h^4 c^4}{64\pi^5 n^4 \tau_s} \frac{Q_{abs}}{r_{SA}^6} \int \frac{f_{em}^S(E) f_{em}^A(E)}{E^4} dE$$

where h , c , n , r_{SA} , and τ_s are Planck’s constant, the speed of light, the refractive index, the sensitizer-activator distance, and the intrinsic lifetime of the sensitizer, respectively; Q_{abs} is the integrated absorption cross-section of the activator ion, $f_{em}^A(E)$ and $f_{em}^S(E)$ are the normalized spectral functions of the absorption band of the activator at intermediate levels ($\int f_{em}^A(E) dE = 1$) and the emission band of the sensitizer at excited states ($\int f_{em}^S(E) dE = 1$), respectively [3, 10]. Therefore, the sensitizer-activator separation (r_{SA}) and the spectral overlap (the integration part) are the two key parameters governing the energy transfer. Another requirement to get efficient energy transfer is the high absorbance (Q_{abs}) of the activator ion at the emission wavelength of the sensitizer ion.

If there is an energy mismatch between the energy levels of the sensitizer and activator ions, the resonant energy transfer probability, W_{SA} decreases exponentially with the magnitude of the mismatch and the energy transfer will be no more resonant. Nevertheless, energy transfer in such case is compensated by the nonradiative, phonon-assisted processes, known as phonon-assisted energy transfer [3, 10].

5. Applications

UC materials have been extensively used in solid-state-lasers and waveguide amplifiers for a long time [3]. Applications in rewritable optical storage and nondestructive optical memory

devices are examples of some recent developments of exploiting UC materials in practical use [3]. Furthermore, the applications of these materials in biological field have been considered after the tremendous progress in preparation of UC nanomaterials with controllable particle size and shape. Recently, a diagnosis method for Ebola virus has been proposed by Tsang et al. using UC nanoparticles [28]. Therefore, advances of UC materials in newer applications will now be discussed in this section.

5.1. Lighting and displays

As a source of three primary colors—red, green and blue, UC emission offers many attractive features for display devices. An eminent advantage is the ability to operate displays with very high brightness and saturated colors without deterioration of the light emitting materials. Such displays are appropriate for high-brightness ambient lighting conditions.

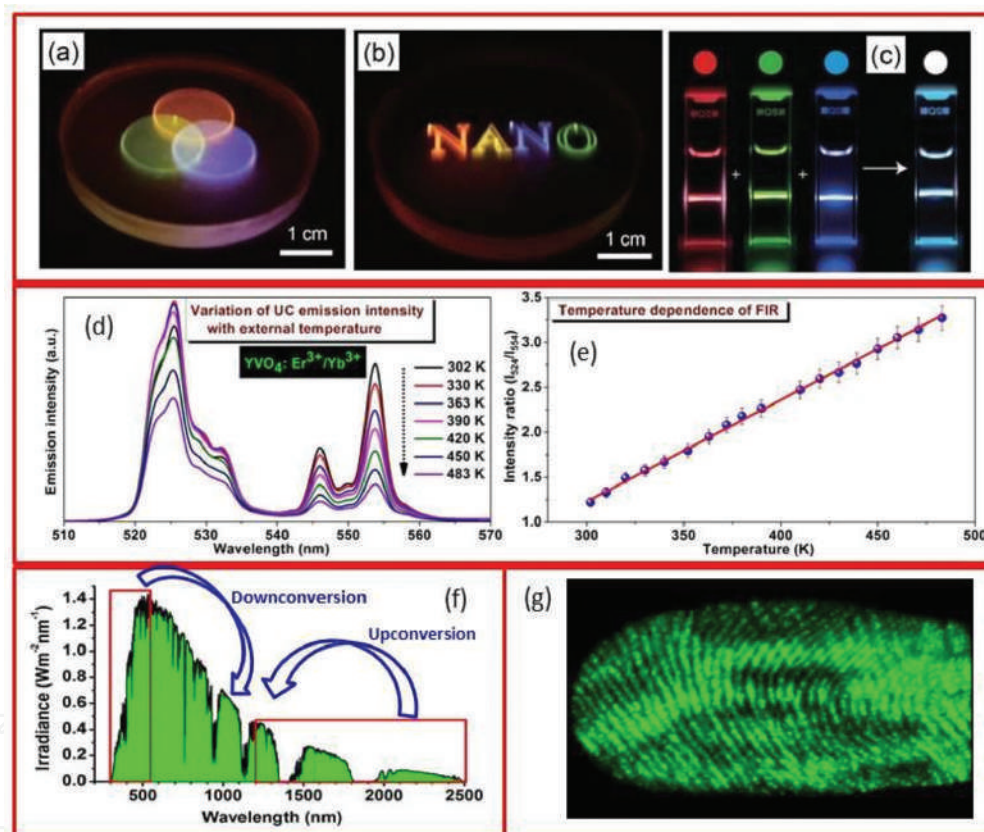


Figure 4. Luminescence color images generated in a RE-doped nanocrystal/polydimethylsiloxane composite monolith show the ability to display (a) additive colors [29], (b) three-dimensional objects [29], (c) volumetric three-dimensional display generated by combining three sets of conventional upconversion nanoparticles featuring monochromatic RGB emission (red, KMnF₃:Yb/Er; green, NaYF₄:Yb/Er; blue, NaYF₄:Yb/Tm) [29], (d) variation of UC emission intensity of green bands (524 nm and 554 nm) with external temperature of YVO₄:Er³⁺/Yb³⁺ particles [36], (e) plot of fluorescence intensity ratio (FIR) as a function of external temperature [36], (f) AM1.5G solar irradiance spectrum (1000 W m⁻²) and available for downconversion or downshifting (about 16% up to 500 nm) and upconversion (about 16% in the range of 1.2–2.5 μm), and (g) fresh fingerprint on glass by dry powdering with YVO₄:ErYb particles illuminated at 980 nm light [47]. Figures reproduced with permission from: (a–c) Ref. [29], Nature Publishing Group; (d and e) Ref. [36], Elsevier; and (g) Ref. [47], Optical Society of America.

The ability of dispersion of UC materials in polymers has further extended their applications in displays. For instance, NaYF₄:Er(Tm),Yb-PMMA nanocomposite producing white, blue, and green lights have been designed by Lin and his group [29] through *in situ* photopolymerization. Downing et al. [30] and Wang et al. [31] have shown that UC materials can be employed for three-dimensional displays. A very recent work by Deng et al. [32] shows the modulation of UC emission color of multilayer core-shell structure by controlling the pulse duration of the excitation laser. **Figure 4(a–c)** exhibits the volumetric three-dimensional display using pulse duration sensitive nanocrystals.

5.2. Temperature sensing

The luminescence from lanthanide-doped materials is an interesting solution to collect information about temperature in hazardous environment, microelectronic and photonic devices. Temperature sensing has been studied from the last decade using luminescent microcrystalline compounds at the tip of scanning thermal probe, at the tip of optical fiber or on the silica-on-silicon waveguides [33]. Although there were some drawbacks due to micron-sized particles; because the material may act as a thermal insulator and light scattering by rough surfaces of the bigger particles degrades the resolution of temperature sensing. The most important feature of UC nanoparticle-based thermometry is that these particles can be employed inside the cells. The temperature sensing of RE-doped UC materials is determined by two commonly used methods, i.e., decay time and fluorescence intensity ratio (FIR) methods. Besides these two major techniques, there are some other reports on temperature sensing based on temperature-dependent variation in emission bandwidth, variation of intensities of Stark sublevels, valley-to-peak intensity ratio, etc. [34, 35]. The most accepted method used for temperature sensing is based on the FIR technique which includes temperature-dependent variation of intensity ratio, emitted from two thermally coupled levels. The FIR method, in principle, uses low excitation power or short pulsed excitation in order to reduce the self-heating of the nanoparticles. The most studied RE element for temperature sensing application is Er³⁺, which has well-known thermally coupled ²H_{11/2} and ⁴S_{3/2} levels. The sensor sensitivity is defined as the ratio in which the FIR changes with the temperature and is considered as the standard figure-of-merit. **Figure 4d** shows the upconversion spectra of an Er³⁺, Yb³⁺ codoped YVO₄ powder recorded within 302–483 K [36]. The change in emission intensity from thermally coupled electronic multiplets is clearly observed. **Figure 4e** shows the plot of intensity ratio versus absolute temperature. As expected the system shows Boltzmann distribution of populations of the ²H_{11/2} and ⁴S_{3/2} levels. Among the luminescent thermometers proposed till now at submicron scale, only a few of them successfully illustrated the temperature sensing with a scanning microscope, e.g., thermal sensors using Er³⁺/Yb³⁺ codoped fluoride glass [37] and NaYF₄:Er³⁺/Yb³⁺ nanoparticles [38]. Temperature sensing performance up to 2000 K using metal-nanoparticle decorated, (Gd,Yb,Er)₂O₃ nanorods exploiting FIR technique and blackbody radiation has been reported recently by Carlos and his group [39].

5.3. Solar cell

Nonabundance of fossil fuel and public nonwillingness to accept nuclear power have encouraged researchers to search for alternative energy sources. Solar energy, a contemporary nonconventional source of energy is an obvious natural target due to its availability in large quantities. Crystalline silicon (c-Si) semiconductor was the key material for the earlier solar cells for converting solar energy into electricity. But the production of solar energy is still limited due to low efficiencies of power conversion. The multijunction semiconductor-based solar cells have maximum conversion efficiency 37.5% while the commercial silica-based solar cells have within 15–20% [40]. On the other hand, the dye-sensitized solar cells (DSSCs) yield conversion efficiencies below 12% [41]. The spectral mismatch between the incident photon energy of solar radiation and the band gap of c-Si semiconductor is one of the most important reasons for the low efficiency. Most of the solar energy is lost in several ways, including conversion to heat energy passing through the solar cell and thus it limits the efficiency [42, 43]. In order to enhance spectral response, wavelength converting layers are added to the solar cells. This layer is capable of absorbing the spectral range where photosensitive materials do not absorb well, although the addition of extra layers may modify the reflection, refraction and other optical responses in a negative or positive way. The photons of lower energy (UV/blue) can be converted into NIR through downconversion processes and NIR light can be upconverted by sequential absorption of two or more low-energy photons into visible or UV, which partially minimizes the optical mismatch in solar cells (**Figure 4f**). At the same time, the thermalization effect due to the carriers is greatly decreased and the conversion efficiency of the solar cell is enhanced. Nevertheless, examination of some available reports demonstrates that downshifting can add 1–2 absolute% to the conversion yield and upconversion 0.5–1% in silicon cells while in DSSC, the conversion yield is increased by 1–1.5% for downshifting and 0.2–0.5% for upconversion [44]. However, it is expected that these numbers will be increased in forthcoming years, especially if plasmonics are used to increase the UC efficiency.

5.4. Security

The unique properties of UC materials make them useful in security ink applications such as latent fingerprint and quick response code printing [45, 46]. Many UC particles are easily dispersible in well-known solvents, allowing printing or coating them onto various substrates. Moreover, multicolor emissions from UC layers upon IR excitation are useful for complex security patterns, giving another level of security or data protection. Earlier, we demonstrated the latent fingerprint detection (**Figure 4g**) using $\text{YVO}_4:\text{Er}/\text{Yb}$ particles by a dry powdering method on a glass slide [47], which shows green fingerprint images upon 980 nm light illumination. The advantage of this technique is that it gives nearly no background and ridges can be detected clearly. The lifetimes of UC nanocrystals under a single-wavelength excitation vary from μs to ms and can be utilized for multiplexing in the time domain which is extendable to security and data storage technology including anticounterfeiting applications [48, 49].

5.5. Biomedical

With unique upconversion properties, UC nanoparticles yield high photostability, high sensitivity, and low optical background noise due to the absence of autofluorescence under NIR radiation which are suitable for bioimaging and biodetection [7, 28, 50, 51]. Moreover, NIR excitation enables deep penetration in tissue without damaging the biological specimens. Such properties of RE-doped UC nanomaterials are appropriate for a wide range of potential biological applications, including photodynamic therapy (PDT), drug delivery, biological imaging, and sensing. Most important point to be concerned for biomedical applications of UC nanomaterials is that the toxicity of the nanoparticles should be evaluated and must be nontoxic in nature for biological applications.

5.5.1. Biological imaging

The UC nanoparticle-based bioimaging has been widely used in cell, tissue, and small animal imaging due to their high contrast, absence of autofluorescence, and photostability against photobleaching and photoblinking [7, 50, 51]. The UC emissions are bright enough to be imaged at moderate excitation power of CW laser and can be used for single-molecule imaging. *In vitro* cellular imaging using RE-doped UC nanoparticles as targets has been demonstrated recently for colon cancer cells [52], ovarian cancer cells [53], HeLa cells [54], breast carcinoma cells [55], etc. In 2006, Lim and his coworkers [56] carried out pioneering work on live organism imaging on *Caenorhabditis elegans* worms using $Y_2O_3:Er,Yb$ nanoparticles. The imaging of the digestive system of the worm under NIR excitation showed track of movement of the nanoparticles in intestines. Besides organism imaging, *in vivo* imaging of small mammals has been studied using $NaYF_4:Er,Yb$ nanoparticles by Chatterjee et al. [52] and demonstrated that the luminescence from the nanoparticles can be clearly observed upon NIR excitation even when the nanoparticles are placed ~10 mm beneath the skin of the animal and the study opens up a new perspective for bioimaging.

5.5.2. Biological sensing and detection

In biological sensing and detection [28, 57], UC luminescence is turned on or off by chromophoric complexes, decorated with the UC nanoparticles and the techniques are based on mainly two processes: fluorescence resonance energy transfer (FRET) and non-FRET [7]. The energy transfer in FRET takes place between donor and acceptor at a very short distance, typically shorter than 10 nm. Wang et al. [58] reported detection of avidin using human biotin-functionalized $NaYF_4:Er/Yb$ and gold nanoparticles. Recently, Liu and his coworkers [59] proposed a highly sensitive biosensing platform based on UC nanoparticles and graphene as donor-acceptor system. On the other hand, in non-FRET based biological sensing, RE-doped UC nanoparticles are used as reporters and the luminescence from the nanoparticles is observed directly. Van de Rijke et al. [60] used $Y_2O_3:S:Er,Yb$ nanoparticles in the detection of nucleic acids and observed four-fold increase in the detection limit compared to conventional reporter.

5.5.3. Photodynamic therapy

The UC nanoparticles have recently been developed for application in cancer photodynamic therapy (PDT) [61–63]. For photodynamic therapy, three primary elements—excitation light, photosensitizer, and reactive oxygen species (ROS) are required. The photosensitizers are excited to the higher energy states under the irradiation of suitable NIR (**Figure 5**). The photosensitizer then returns to lower energy state producing energy which is transferred to the nearby oxygen and creates ROS that damages the cancer cells in the vicinity. Zhang et al. [64] first time designed the UC nanoparticles, coated with layer of mesoporous silica shell where the photosensitizers were doped for photodynamic therapy for the treatment of bladder cancer cells. Yan and his group [65] constructed $\text{NaGdF}_4:\text{Yb,Er}@\text{CaF}_2$ core/shell UC nanoparticles loaded with hematoporphyrin and silicon phthalocyanine dihydroxide molecules, and showed excellent PDT efficiency in HeLa cancer cells upon NIR irradiation.

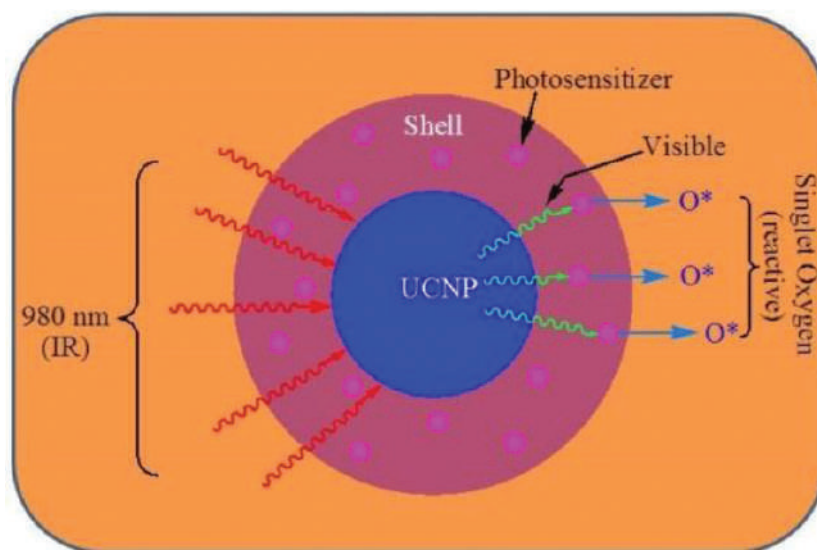


Figure 5. Schematic diagram of UC-based photodynamic therapy. The upconversion nanoparticles emit visible light which further excites the photosensitizers, resulting in the production of ROS and causes damage to the nearby cancer cells.

6. Summary and outlook

In summary, we presented an overview of the synthesis, properties, and recent development of RE-doped UC materials in various emerging applications. The UC materials show potential for a wide range of energy-related applications covering from lighting and display technologies to photovoltaic. At the same time, UC nanoparticles have proven to be effective in biological applications due to their unique optical and chemical properties such as absence of autofluorescence, low-toxicity, low photodamage to the biological cells, and high tissue-penetration depth of the excitation light. In spite of these benefits, there remain some limitations at the fundamental level associated with the practical use of UC materials. For example,

the efficiency of UC materials is restricted and to date, the maximum internal quantum yield has been obtained as 7.6% for $\text{LiLuF}_4:\text{Yb,Tm}@\text{LiLuF}_4$ [66] nanoparticles under NIR excitation. Another challenge for UC nanoparticles is surface engineering which is required for biomedical application and surface modification generally decreases the luminescence efficiency. Additionally, for biological applications, the UC nanoparticles should be the smallest (<10 nm) and the problem associated with smaller nanoparticles is that the upconversion efficiency decreases with decreasing particle size. However, manipulation of local environment around the RE ions in UC particles along with plasmons, quantum dots, dyes, or other dopants with a strong absorption might be effective ways to enhance the quantum yield. Therefore, more significant benefits of UC materials through constant and thriving research are yet to come in future for fundamental understanding as well as in emerging applications.

Acknowledgements

This work has been supported from the European Commission (“Interweave” – Erasmus Mundus project).

Author details

Manoj Kumar Mahata*, Hans Christian Hofsäss and Ulrich Vetter

*Address all correspondence to: mmahata@phys.uni-goettingen.de

Second Institute of Physics, University of Goettingen, Goettingen, Germany

References

- [1] Bloembergen N. Solid state infrared quantum counters. *Phys. Rev. Lett.* 1959;2:84–85. DOI: 10.1103/PhysRevLett.2.84
- [2] Auzel F. Upconversion and anti-Stokes processes with f and d ions in solids. *Chem. Rev.* 2004;104:139–173. DOI: 10.1021/cr020357g
- [3] Zhou B., Shi B., Jin D., Liu X. Controlling upconversion nanocrystals for emerging applications. *Nature Nanotech.* 2015;10:924–936. DOI: 10.1038/NNANO.2015.251
- [4] Zheng W., Huang P., Tu D., Ma E., Zhua H., Chen X. Lanthanide-doped upconversion nano-bioprobes: electronic structures, optical properties, and biodetection. *Chem. Soc. Rev.* 2015;44:1379–1415. DOI: 10.1039/c4cs00178h
- [5] Walrand C. G., Binnemans K. Rationalization of crystal-field parametrization. In: Gscheidner Jr. K. A., Eyring L., editors. *Handbook on the Physics and Chemistry of*

- Rare Earths. 23rd ed. Netherland: Elsevier Science B.V.; 1996. p. 121–283. DOI: 10.1016/S0168-1273(96)23006-5
- [6] Sun L. D., Dong H., Zhang P. Z., Yan C. H. Upconversion of Rare Earth Nanomaterials. *Annu. Rev. Phys. Chem.* 2015;66:619–642. DOI: 10.1146/annurev-physchem-040214-121344
- [7] Lin M., Zhao Y., Wang S. Q., Liu M., Duan Z. F., Chen Y. M. et al. Recent advances in synthesis and surface modification of lanthanide-doped upconversion nanoparticles for biomedical applications. *Biotechnol. Adv.* 2012;30(6):1551–1561. DOI: 10.1016/j.biotechadv.2012.04.009
- [8] Haase M., Schäfer H. Upconverting nanoparticles. *Angew. Chem. Int. Ed.* 2011;50:5808–5829. DOI: 10.1002/anie.201005159
- [9] Huang F., Liu X., Ma Y., Kang S., Hu L., Chen D. Origin of near to middle infrared luminescence and energy transfer process of Er³⁺/Yb³⁺ co-doped fluorotellurite glasses under different excitations. *Sci. Rep.* 2015;5:8233(1–6). DOI: 10.1038/srep08233
- [10] Nadort A., Zhao J., Goldys E. M. Lanthanide upconversion luminescence at the nanoscale: fundamentals and optical properties. *Nanoscale.* 2016;8:13099–13130. DOI: 10.1039/C5NR08477F
- [11] Chang H., Xie J., Zhao B., Liu B., Xu S., Ren N. et al. Rare earth ion-doped upconversion nanocrystals: synthesis. *Nanomaterials.* 2015;5:1–25. DOI: 10.3390/nano5010001
- [12] Mai H., Zhang Y., Sun L., Yan C. Size- and phase-controlled synthesis of monodisperse NaYF₄:Yb,Er nanocrystals from a unique delayed nucleation pathway monitored with upconversion spectroscopy. *J. Phys. Chem. C.* 2007;111:13730–13739. DOI: 10.1021/jp073919e
- [13] Yi G. S., Chow G. M. Colloidal LaF₃:Yb,Er, LaF₃:Yb,Ho and LaF₃:Yb,Tm nanocrystals with multicolor upconversion fluorescence. *J. Mater. Chem.* 2005;15:4460–4464. DOI: 10.1039/B508240D
- [14] Mahata M. K., Kumar K., Rai V. K. Structural and optical properties of Er³⁺/Yb³⁺ doped barium titanate phosphor prepared by co-precipitation method. *Spectrochim. Acta A.* 2014;124:285–291. DOI: 10.1016/j.saa.2014.01.014
- [15] Mahata M. K., Koppe T., Hofsäss H., Kumar K., Vetter U. Host sensitized luminescence and time-resolved spectroscopy of YVO₄:Ho³⁺ nanocrystals. *Phys. Procedia.* 2015;76:125–131. DOI: 10.1016/j.phpro.2015.10.023
- [16] Wu H., Xu H., Su Q., Chen T., Wu M. Size- and shape-tailored hydrothermal synthesis of YVO₄ crystals in ultra-wide pH range condition. *J. Mater. Chem.* 2011;13:1223–1228. DOI: 10.1039/B210713

- [17] Zeng J. H., Su J., Li Z. H., Yan R. X., Li, Y. D. Synthesis and upconversion luminescence of hexagonal-phase $\text{NaYF}_4:\text{Yb}^{3+}, \text{Er}^{3+}$ phosphors of controlled size and morphology. *Adv. Mater.* 2005;17:2119–2123. DOI: 10.1002/adma.200402046
- [18] Patra A., Friend C. S., Kapoor R., Prasad P. N. Fluorescence upconversion properties of Er^{3+} -doped TiO_2 and BaTiO_3 nanocrystallites. *Chem. Mater.* 2003;15:3650–3655. DOI: 10.1021/cm020897u
- [19] Patra A., Friend C. S., Kapoor R., Prasad P. N. Upconversion in $\text{Er}^{3+}:\text{ZrO}_2$ nanocrystals. *J. Phys. Chem. B.* 2002;106:1909–1912. DOI: 10.1021/jp013576z
- [20] Cheng Z. Y., Xing R. B., Hou Z. Y., Huang S. S., Lin J. Patterning of light-emitting $\text{YVO}_4:\text{Eu}^{3+}$ thin films via inkjet printing. *J. Phys. Chem. C.* 2010;114:9883–9888. DOI: 10.1021/jp101941y
- [21] Wang F., Deng R. R., Wang J., Wang Q. X., Han Y., Zhu H., et al. Tuning upconversion through energy migration in core-shell nanoparticles. *Nat. Mater.* 2011;10:968–973. DOI: 10.1038/nmat3149
- [22] Mahata M. K., Koppe T., Mondal T., Bruesewitz C., Kumar K., Rai V. K., et al. Incorporation of Zn^{2+} ions into $\text{BaTiO}_3:\text{Er}^{3+}/\text{Yb}^{3+}$ nanophosphor: an effective way to enhance upconversion, defect luminescence and temperature sensing. *Phys. Chem. Chem. Phys.* 2015;17:20741–20753. DOI: 10.1039/c5cp01874a
- [23] Judd B. Optical absorption intensities of rare-earth ions. *Phys. Rev.* 1962;127(3):750–761. DOI: 10.1103/PhysRev.127.750
- [24] Ofelt G. Intensities of crystal spectra of rare-earth ions. *J. Chem. Phys.* 1962;37 :511–520. DOI: 10.1063/1.1701366
- [25] Pollnau M., Gamelin D., Lüthi S., Güdel H., Hehlen M. Power dependence of upconversion luminescence in lanthanide and transition-metal-ion systems. *Phys. Rev. B: Condens. Matter.* 2000;61:3337–3346. DOI: 10.1103/PhysRevB.61.3337
- [26] Suyver J. F., Aebischer A., García-Revilla S., Gerner P., Güdel H. U. Anomalous power dependence of sensitized upconversion luminescence. *Phys. Rev. B.* 2005;71:125123. DOI: 10.1103/PhysRevB.71.125123
- [27] Dexter D. L. A theory of sensitized luminescence in solids. *J. Chem. Phys.* 1953;21:836–850. DOI: 10.1063/1.1699044
- [28] Tsang M. K., Ye W. W., Wang G., Li J., Yang M., Hao J. Ultrasensitive detection of Ebola virus oligonucleotide based on upconversion nanoprobe/nanoporous membrane system. *ACS Nano.* 2016;10(1):598–605. DOI: 10.1021/acsnano.5b05622
- [29] Boyer J. C., Johnson N. J. J., van Veggel F. C. J. M. Upconverting lanthanide-doped NaYF_4 -PMMA polymer composites prepared by in situ polymerization. *Chem. Mater.* 2009;21(10):2010–2012. DOI: 10.1021/cm900756h

- [30] Downing E., Hesselink L., Ralston J., Macfarlane R. A three-color, solid-state, three-dimensional display. *Science*. 1996;273(5279):1185–1189. DOI: 10.1126/science.273.5279.1185
- [31] Wang F., Han Y., Lim C. S., Lu Y. H., Wang J., Xu J., et al. Simultaneous phase and size control of upconversion nanocrystals through lanthanide doping. *Nature*. 2010;463:1061–1065. DOI: 10.1038/nature08777
- [32] Deng R., Qin F., Chen F., Huang W., Hong M., Liu X. Temporal full-colour tuning through non-steady-state upconversion. *Nat. Nanotechnol.* 2015;10:237–242. DOI: 10.1038/nnano.2014.317
- [33] Henry D. M., Herringer J. H., Djeu N. Response of 1.6 μm Er:Y₃Al₅O₁₂ fiber-optic temperature sensor up to 1520. *Appl. Phys. Lett.* 1999;74:3447. DOI: 10.1063/1.12412
- [34] Soni A. K., Dey R., Rai V. K. Stark sublevels in Tm³⁺–Yb³⁺ codoped Na₂Y₂B₂O₇ nanophosphor for multifunctional application. *RSC Adv.* 2013;5:34999–35009. DOI: 10.1039/C4RA15891
- [35] Li L., Xu W., Zheng L., Qin F., Zhou Y., Liang Z., et al. Valley-to-peak intensity ratio thermometry based on the red upconversion emission of Er³⁺. *Opt. Exp.* 2016;24(12):13244–13249. DOI: 10.1364/OE.24.013244
- [36] Mahata M. K., Kumar K., Rai V. K. Er³⁺–Yb³⁺ doped vanadate nanocrystals: a highly sensitive thermographic phosphor and its optical nanoheater behavior. *Sensor Actuat. B-Chem.* 2015;209:775–780. DOI: 10.1016/j.snb.2014.12.039
- [37] Peng H. S., Stich M. I. J., Yu J. B., Sun L. N., Fischer L. H., Wolfbeis O. S. Luminescent europium(III) nanoparticles for sensing and imaging of temperature in the physiological range. *Adv. Mater.* 2010;22:716–719. DOI: 10.1002/adma.200901614
- [38] Vetrone F., Naccache R., Zamarron A., Juarranz de la Fuente A., Sanz-Rodríguez F., Maestro L. M., et al. Temperature sensing using fluorescent nanothermometers. *ACS Nano*. 2010;4:3254–3258. DOI: 10.1021/nn100244a
- [39] Debasu M. L., Ananias D., Pastoriza-Santos I., Liz-Marzan L. M., Rocha J., Carlos L. D. All-in-one optical heater-thermometer nanoplatform operative from 300 to 2000 K based on Er³⁺ emission and blackbody radiation. *Adv. Mater.* 2013;25:4868–4874. DOI: 10.1002/adma.201300892
- [40] Green M. A., Emery K., Hishikawa Y., Warta W., Dunlop E. D. Progress in photovoltaics: research and applications. *Photovoltaics*. 2012;20:606–614. DOI: 10.1002/pip.2267
- [41] Yella A., Lee H. W., Tsao H. N., Yi C. Y., Chandiran A. K., Nazeeruddin M. K., et al. Porphyrin-sensitized solar cells with cobalt (II/III)-based redox electrolyte exceed 12 percent efficiency. *Science*. 2011;334:629–634. DOI: 10.1126/science.1209688

- [42] Hill S. P., Dilbeck T., Baduell E., Hanson K. Integrated photon upconversion solar cell via molecular self-assembled bilayers. *ACS Energy Lett.* 2016;1(1):3–8. DOI: 10.1021/acsenergylett.6b00001
- [43] Rodríguez-Rodríguez H., Imanieh M. H., Lahoz F., Martín I. R. Analysis of the upconversion process in Tm³⁺ doped glasses for enhancement of the photocurrent in silicon solar cells. *Sol. Energ. Mat. Sol. Cells.* 2016;144:29–32. DOI: 10.1016/j.solmat.2015.08.017
- [44] Bünzli J. C. G., Chauvin A. S. Lanthanides in Solar Energy Conversion. In: Bünzli J. C. G., Pecharsky V. K., editors. *Handbook on the Physics and Chemistry of Rare Earths*. 44th ed. Amsterdam: Elsevier Science, B.V.; 2014. p. 169–281. DOI: 10.1016/B978-0-444-62711-7.00261-9
- [45] Wang J., Wei T., Li X., Zhang B., Wang J., Huang C., et al. Near-infrared-light-mediated imaging of latent fingerprints based on molecular recognition. *Angew. Chem. Int. Ed.* 2014;53:1616–1620. DOI: 10.1002/anie.201308843
- [46] Meruga J. M., Baride A., Cross W., Kellar J. J., May P. S. Red-green-blue printing using luminescence-upconversion inks. *J. Mater. Chem. C.* 2014;2:2221–2227. DOI: 10.1039/C3TC32233E
- [47] Mahata M. K., Tiwari S. P., Mukherjee S., Kumar K., Rai V. K. YVO₄:Er³⁺/Yb³⁺ phosphor for multifunctional applications. *J. Opt. Soc. Am. B.* 2014;31(8):1814–1821. DOI: 10.1364/JOSAB.31.001814
- [48] Gorris H. H., Wolfbeis O. S. Photon-upconverting nanoparticles for optical encoding and multiplexing of cells, biomolecules, and microspheres. *Angew. Chem. Int. Ed.* 2013;52:3584–3600. DOI: 10.1002/anie.201208196
- [49] Kumar P., Singh S., Gupta B.K. . Future prospects of luminescent nanomaterial based security inks: from synthesis to anti-counterfeiting applications. *Nanoscale.* 2016;8:14297–14340. DOI: 10.1039/C5NR06965C
- [50] Liu Y., Su Q., Zou X., Chen M., Feng W., Shi Y. et al. Near-infrared in vivo bioimaging using a molecular upconversion probe. *Chem. Commun.* 2016;52:7466–7469. DOI: 10.1039/C6CC03401B
- [51] Tan G. R., Wang M., Hsu C.Y., Chen N., Zhang Y. Small upconverting fluorescent nanoparticles for biosensing and bioimaging. *Adv. Opt. Mater.* 2016;4(7):984–997. DOI: 10.1002/adom.201600141
- [52] Chatterjee D. K., Rufaihah A. J., Zhang Y. Upconversion fluorescence imaging of cells and small animals using lanthanide doped nanocrystals. *Biomaterials.* 2008;29:937–943. DOI: 10.1016/j.biomaterials.2007.10.051
- [53] Boyer J. C., Manseau M. P., Murray J. I., van Veggel F. C. J. M. Surface modification of upconverting NaYF₄ nanoparticles doped with PEG-phosphate ligands for NIR (800 nm) biolabeling within the biological window. *Langmuir.* 2010;26:1157–1164. DOI: 10.1021/la902260j

- [54] Cheng L., Yang K., Li Y. G., Chen J. H., Wang C. Y., Shao M. W., et al. Facile preparation of multifunctional upconversion nanoprobe for multimodal imaging and dual-targeted photothermal therapy. *Angew. Chem.* 2011;123:7523–7528. DOI: 10.1002/anie.201101447
- [55] Yang Y. M., Shao Q., Deng R. R., Wang C., Teng X., Cheng K., et al. In vitro and in vivo uncaging and bioluminescence imaging by using photocaged upconversion nanoparticles. *Angew. Chem. Int. Ed.* 2012;51:3125–3129. DOI: 10.1002/anie.201107919
- [56] Lim S. F., Riehn R., Ryu W. S., Khanarian N., Tung C. K., Tank D., et al. In vivo and scanning electron microscopy imaging of upconverting nanophosphors in *Caenorhabditis elegans*. *Nano Lett.* 2006;6:169–174. DOI: 10.1021/nl0519175
- [57] Li H., Shi L., Sun D., Li P., Liu Z. Fluorescence resonance energy transfer biosensor between upconverting nanoparticles and palladium nanoparticles for ultrasensitive CEA detection. *Biosens. Bioelectron.* 2016;86:791–798. DOI: 10.1016/j.bios.2016.07.070
- [58] Wang L. Y., Yan R. X., Huo Z. Y., Wang L., Zeng J. H., Bao J. et al. Fluorescence resonant energy transfer biosensor based on upconversion-luminescent nanoparticles. *Angew. Chem. Int. Ed.* 2005;44:6054–6057. DOI: 10.1002/anie.200501907
- [59] Liu J., Liu Y., Liu Q., Li C., Sun L., Li F. Iridium(III) complex-coated nanosystem for ratiometric upconversion luminescence bioimaging of cyanide anions. *J. Am. Chem. Soc.* 2011;133:15276–15279. DOI: 10.1021/ja205907y
- [60] van de Rijke F., Zijlmans H., Li S., Vail T., Raap A. K., Niedbala R. S. et al. Up-converting phosphor reporters for nucleic acid microarrays. *Nature Biotechnol.* 2001;19:273–276. DOI: doi: 10.1038/85734
- [61] Dong H., Tang S., Hao Y., Yu H., Dai W., Zhao G. et al. Fluorescent MoS₂ quantum dots: ultrasonic preparation, up-conversion and down-conversion bioimaging, and photodynamic therapy. *ACS Appl. Mater. Interfaces.* 2016;8(5):3107–3117. DOI: 10.1021/acsami.5b10459
- [62] Lu F., Yang L., Ding Y., Zhu J. J. Highly emissive Nd³⁺-sensitized multilayered upconversion nanoparticles for efficient 795 nm operated photodynamic therapy. *Adv. Funct. Mater.* 2016;26(26):4778–4785. DOI: 10.1002/adfm.201600464
- [63] Chen J., Zhao J. X. Upconversion nanomaterials: synthesis, mechanism, and applications in sensing. *Sensors.* 2012;12:2414–2435. DOI: 10.3390/s120302414
- [64] Zhang P., Rogelj S., Nguyen K., Wheeler D. Design of a highly sensitive and specific nucleotide sensor based on photon upconverting particles. *J. Am. Chem. Soc.* 2006;128:12410–12411. DOI: 10.1021/ja0644024

- [65] Qiao X. F., Zhou J. C., Xiao J. W., Wang Y. F., Sun L. D., Yan C. H. Triple-functional core-shell structured upconversion luminescent nanoparticles covalently grafted with photosensitizer for luminescent, magnetic resonance imaging and photodynamic therapy in vitro. *Nanoscale*. 2012;4:4611–4623. DOI: 10.1039/C2NR30938F
- [66] Huang P., Zheng W., Zhou, S., Tu D., Chen Z., Zhu H. et al. Lanthanide-doped LiLuF_4 upconversion nanoprobe for the detection of disease biomarkers. *Angew. Chem. Int. Ed.* 2015;53(5):1252–1257. DOI: 10.1002/anie.201309503

IntechOpen

We are IntechOpen, the world's leading publisher of Open Access books Built by scientists, for scientists

6,300

Open access books available

171,000

International authors and editors

190M

Downloads

Our authors are among the

154

Countries delivered to

TOP 1%

most cited scientists

12.2%

Contributors from top 500 universities



WEB OF SCIENCE™

Selection of our books indexed in the Book Citation Index
in Web of Science™ Core Collection (BKCI)

Interested in publishing with us?
Contact book.department@intechopen.com

Numbers displayed above are based on latest data collected.
For more information visit www.intechopen.com



Luminescent Glass for Lasers and Solar Concentrators

Meruva Seshadri, Virgilio de Carvalho dos Anjos and
Maria Jose Valenzuela Bell

Additional information is available at the end of the chapter

<http://dx.doi.org/10.5772/65057>

Abstract

Rare earth-doped glasses find applications in numerous photonic devices including color displays, infrared solid-state lasers, and indicators, among many. In this chapter, we will present and discuss several luminescent glasses doped with rare earth ions in their trivalent form (RE^{3+}) with general background and technological perspectives. Initially, we begin with a short introduction of RE^{3+} electronic energy-level structure in solids followed by the discussion of structural feature of glass lasers. While the lasing properties are mainly governed by the solubility of the ions and phonon interactions, the issue of ion interactions in solid hosts will be addressed since they hardly depend on the type of materials. Spectroscopic properties of Nd^{3+} -doped phosphate glasses are discussed in the framework of Judd-Ofelt theory. Rare earth-doped optical amplifiers are tackled from a technological point of view, as well as luminescent solar concentrators for enhancement of solar efficiency.

Keywords: glasses, rare earth ions, luminescence, optical amplifiers, solar concentrators

1. Introduction

A large number of ions from the lanthanide (rare earth) and actinide groups of periodic table exhibit laser action when doped into a large number of host crystals or glasses. The construction of high-power crystalline lasers requires substantial crystal sizes. In practice, crystals are grown by the small seed crystals while pulling the larger crystal from the melt. These methods are very difficult if larger crystals are needed. When glasses are used as host media, the

environments of the ions vary much more than in a crystalline material because of the random structural character of the glass matrix. All glass lasers until present date have used trivalent lanthanides as the active ions. Glass plays many varied roles in rare earth laser systems, as it can be made with uniformly distributed rare earth concentrations and has great potential as a laser host medium. In addition, rare earth-doped fibers have received growing attention recently. They can be used as amplifiers in optical communication systems and as optical sources. Glass lasers are substantially inhomogeneously broadened, and usually present more broader line width than Nd:YAG ones. The laser transition line width and shape typically vary from one glass to another glass matrix. In this way, innovation of glass lasers remains a vibrant area in the development of science and technology. The luminescent glass materials are used to develop solid-state lasers operating in visible and NIR regions due to their potential applications in the fields of medical, eye safe lasers, atmosphere pollution monitoring, energy converters and telecommunications. Sharp fluorescent lines, strong absorption bands, and reasonable high quantum efficiency will determine the adequacy of laser material.

In this contribution, the introduction consists of brief review of electronic energy-level structure of RE^{3+} in solids, structural features, and general considerations in laser glasses. Laser glasses and amplifiers are studied to know the spectroscopic parameters using spectroscopic techniques. Especially, the current achievements on Nd³⁺-doped phosphate glass lasers will be discussed and numerous data will be presented. Er³⁺-doped glass fiber amplifiers subject will also be addressed. Finally, we will discuss rare earth-based luminescence concentrators for photovoltaic applications.

1.1. Rare earth ions as luminescent centers

Trivalent rare earth ions are well known for their special optical properties, which result from the fact that the electronic transitions within the 4f shell occur at optical frequencies. The 4f shell is shielded by the completely filled 5s and 5p shells, so the frequencies of the transitions are almost independent of the host. Generally, the electric dipole transitions are forbidden due to equal parity of the electronic levels within the 4f shell. Those transitions are possible in solids that have slightly mixed odd-parity wave functions. As a result, the absorption and emission cross sections are small ($\sim 10^{-20}$ or 10^{-21} cm²), and the lifetime of the luminescent level is relatively long ranging from microseconds to several milliseconds. The influence of the electric field around the ions removes the degeneracy of the 4f levels, resulting in a Stark splitting of the levels. **Figure 1** shows the energy levels of the trivalent lanthanide ions (4f configurations). This figure provides useful information to predict and/or to make a proper assignment of the emission spectra corresponding to trivalent rare earth ions in crystals or glasses.

The energy levels of the 4f shell arise from spin-spin and spin-orbit interactions and are often denoted using Russell-Saunders notation $^{2S+1}L_J$ [1, 2], in which S is the total spin angular momentum, L is the total orbital angular momentum, and J is the total angular momentum. There exist 14 rare earth elements all having a different number of electrons in the incompletely filled 4f shell. However, due to the shielding by the outer lying shells, the magnitude of the splitting is small, resulting in relatively narrow lines.

Table 1 displays some important emission transitions of rare earth ions and their technological interest. More general views about the spectra and energy levels of rare earth ions can be found in literature [9–12]. The large number of excited states that are suitable for optical pumping and subsequent decay to metastable states having high quantum efficiencies and narrow emission lines is favorable for achieving laser action.

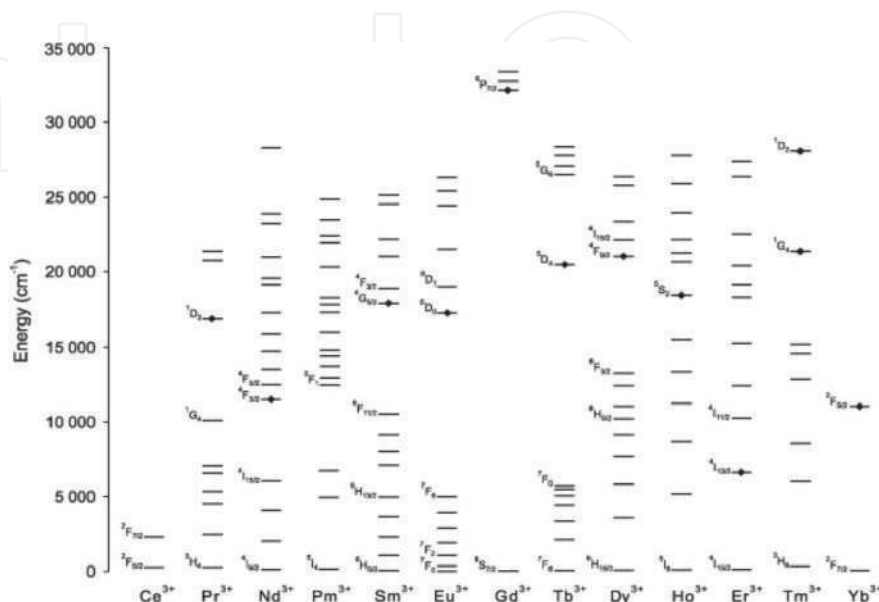


Figure 1. Schematic energy levels of rare earth ions.

RE ³⁺ ions	Transitions	Wavelength (nm)	Application
Pr ³⁺	¹ G ₄ → ³ H ₅	1300	Optical amplifier [3]
Nd ³⁺	⁴ F _{3/2} → ⁴ I _{11/2}	1064	Solid-state lasers [4]
Eu ³⁺	⁵ D ₀ → ⁷ F ₂	615	Displays, lighting [5]
Tb ³⁺	⁵ D ₄ → ⁷ F ₅	545	Lighting [6]
Dy ³⁺	⁶ F _{11/2} + ⁶ H _{9/2} → ⁶ H _{15/2}	1300	Optical amplifier [7]
Er ³⁺	⁴ I _{13/2} → ⁴ I _{15/2}	1530	Optical amplifier [8]
Tm ³⁺	³ H ₄ → ³ F ₄	1480	Optical amplifier [7]
Yb ³⁺	² F _{5/2} → ² F _{7/2}	980	Sensitizer [6]

Table 1. Important emission lines of some lanthanide ions.

1.2. Glasses for lasers and amplifiers: structural features

Glasses are widely used nowadays and present several applications in different fields of life. There are several definitions for glassy materials. Grouping them one can define glass as an inorganic product of melting which has been cooled to a solid without crystallization [13]. It means that glass looks like an undercooled liquid. An undercooled liquid can crystallize at any moment but at room temperature it is not possible. Therefore, glass is an amorphous

material as it does not exhibit long range order of atoms in a lattice. The transition of a glass melt to a crystallized state at the crystallization temperature does not take place if the cooling of the glass is fast. Below the crystallization temperature, glass behaves like a fluid down to the transformation temperature. Below this temperature, glass has the properties of a solid. Glass can also be defined as an amorphous solid lacking completely, in long range, periodic atomic structure and exhibiting a region of glass transformation behavior.

In general, glasses can be prepared either from high quality, chemically pure components or from a mixture of far less pure minerals. The batch materials can be divided into five categories depending on the property of components used in the glass preparation: (1) *glass formers*, (2) *flux*, (3) *property modifier*, (4) *colorant*, and (5) *fining agent*. Every glass contains one or more components, which serve as the primary source of the structure. The same component may be classified into different categories when used for different purposes. For example, alumina serves as a glass former in aluminate glasses but in most silicate glasses, it works as property modifier [14]. Zachariasen [15] noted that those crystalline oxides that form open, continuous networks tended to form glasses and those glass-forming networks were associated with ions with particular coordination numbers (CN). The primary glass formers in commercial oxide glasses are silica (SiO_2), boric oxide (B_2O_3), and phosphoric oxide (P_2O_5), in addition to other compounds GeO_2 , Bi_2O_3 , As_2O_3 , Sb_2O_3 , TeO_2 , Al_2O_3 , Ga_2O_3 , and V_2O_5 which act as glass formers under certain circumstances.

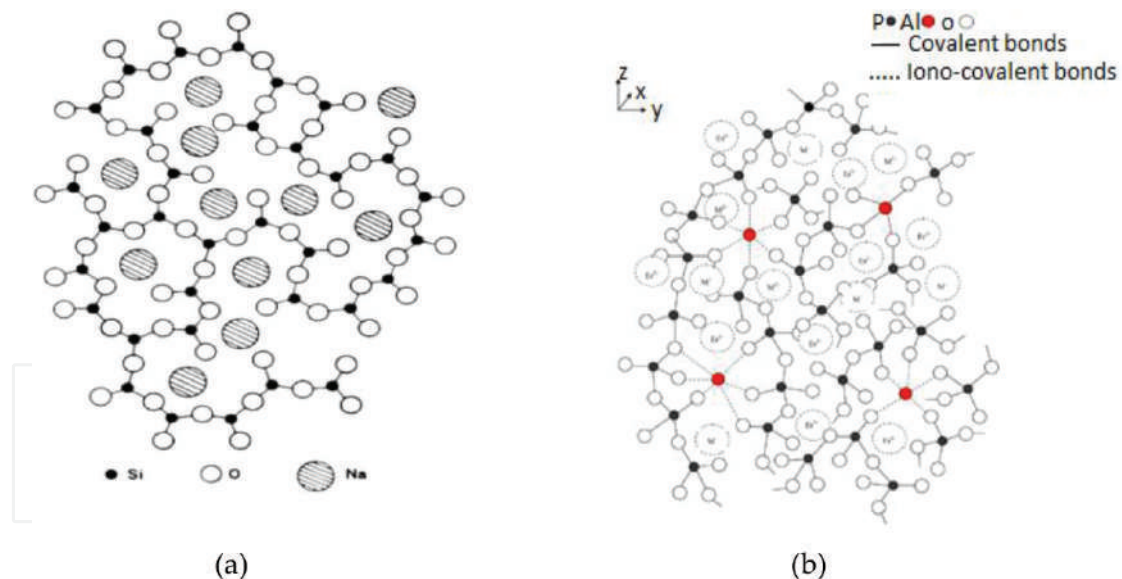


Figure 2. Schematic representation of (a) random network of alkali silicate and (b) glass structure of different atomic neighborhoods (3D).

These oxide glass formers play an important structural role in glasses when used as network or intermediate oxide modifiers. Thus, the oxide network modifiers will create strong bridging oxygen (BO) bonds in between the glass-forming polyhedra and weak nonbridging oxygen (NBO) bonds (see in **Figure 2a**). Moreover, the oxide modifiers will control many useful properties, lowering the melting temperature that is highly useful for developing

technologically used glasses. The intermediate oxides also modify glass properties due to their coordination numbers and bond strengths in between the network formers and network modifiers. **Table 2** reports some of the oxide-based modifier glasses for realization of structure influence on various properties.

Glass composition	D (g/cm ³)	T _g (°C)	n _d	τ (ms)
60SiO ₂ -20Al ₂ O ₃ -20Li ₂ O [16]	2.40	693	1.531	2.65
20Na ₂ O [16]	2.45	811	1.507	2.45
20MgO [16]	2.55	827	1.548	2.43
20CaO [16]	2.61	868	1.557	2.37
20ZnO [16]	2.84	742	1.573	2.51
20La ₂ O ₃ [16]	4.08	863	1.709	2.01
71SiO ₂ -14Al ₂ O ₃ -15MgO [17]	2.44	831	1.520	2.48
10CaO [17]	2.61	829	1.549	–
10BaO [17]	2.86	841	1.549	2.39
15SrO [17]	2.73	834	1.549	–
TBZN–0.05Ho ₂ O ₃ [18]	4.248	286	–	17.4
0.1Ho ₂ O ₃	4.212	288	–	18.2
0.5Ho ₂ O ₃	4.137	290	–	17.0
1.0Ho ₂ O ₃	3.949	292	–	15.1
1.5Ho ₂ O ₃	4.116	295	–	14.5

Table 2. Density (D), transition temperature (T_g), refractive index (n_d), and lifetime of respective ions (τ_{599 nm(Sm³⁺)} [16, 17]; τ_{660 nm(Ho³⁺)} [18]) in different oxide modifier-based glass compositions.

Owing to superior physical properties such as high thermal expansion coefficients, low melting and softening temperatures, and high ultraviolet transmission, phosphate glasses have several important attributes over conventional silicate and borate glasses. However, the poor chemical durability of these early optical glasses has temporarily discouraged for their further development. Interest in the amorphous alkali phosphates was stimulated in the 1950s by their use in a variety of industrial applications, including sequestering agents for hard water treatments and dispersants for clay processing and pigment manufacturing [19]. Studying such materials, Van Wazer [20] established the foundations for much of our current understanding of the nature of phosphate glasses. Kordes and co-workers [21, 22] re-examined the alkaline earth phosphate glasses, including UV-transmitting compositions and observed some “anomalous” trends in properties.

Phosphate glasses have unique characteristics that include high transparency, high thermal stability, low refractive index and dispersion, and high gain density due to high solubility for lanthanide ions and hence find growing field of applications [23–26]. An important step in

laser glasses occurred in 1967 when phosphate-based compositions were first explored [27]. Several phosphate glasses find considerable applications in optical data transmission, detection, and sensing [28]. The phosphate glasses also find applications in fast ion conductors, optical filters, reference electrodes, stable storage medium for immobilizing high-level nuclear waste [29] and as additives in the manufacturing of insulating polymeric cables. Certain phosphate vitreous electrolytes are being used increasingly in electrochemical sensors, in prototype batteries, and in electrochemical devices. There have been many excellent reviews of structural studies on phosphate glasses including that of Van Wazer [20, 30, 31]. A schematic structure of different atomic neighborhoods (covalent and ionocovalent) in rare earth (Er^{3+})-doped phosphate glass is shown **Figure 2b**.

The large concentration of lasing atoms can be doped easily into different glasses, which can be made in different shapes and sizes depending on technological needs. The high-power laser threshold is possible from the ions-doped glasses compared to the same ions-doped crystal due to their large absorbing capability of incident energy and energy level broadening. The electronic transitions of rare earth ions have 4f-4f and 4f-5d configurations, which are weakly affected by the host material, since the 4f electrons are effectively screened by outer, filled electron shells. Thus, these transitions cause absorption and fluorescence patterns from the ultraviolet (UV) to infrared regions and they are narrow. Two important aspects of the optical behavior of rare earth ions are determined by the host material. One is the electric dipole transitions which occur between 4f states are strictly forbidden for an isolated ion, since the parity of the electronic configuration must change with an electric dipole transition. However, the strengths of these electric dipole transitions remains relatively weak due the perturbative nature of the admixing states, and as consequence, the radiative lifetimes of excited rare earth ions can be relatively long ($\sim 10^{-3}$ ms). Another aspect is related to the nonradiative rates originated from relaxation of the excited states of the rare earth ions, which is determined by the host material. Recently, Babu et al. [32] had studied different fluorophosphate glasses doped with 0.5 mol% of Er^{3+} ions through the Judd-Ofelt and McCumbers theories for potential broadband optical fiber lasers and amplifiers. Praseodymium (Pr^{3+})-doped high-aluminum phosphate (HAP) glasses with excellent chemical durability for thermal ion-exchanged optical waveguide have been investigated by Tian et al. [33]. In order to improve the solar cell efficiency, potential downconversion was studied in $\text{GeS}_2\text{-Ga}_2\text{S}_3\text{-CsCl}$ glass for modifying solar spectrum and are found quantum yield to be below 1200 and 1650 nm are 51 and 76%, respectively [34].

2. Limiting factors in rare earth-doped glasses

2.1. RE^{3+} ions solubility in glasses

Higher concentration of RE^{3+} ions in glasses lead to clusters. Thus, the clusters of rare earth ion serve as luminescent quenchers, either by increasing ion-ion interactions between rare earth ions or by forming rare earth compounds that are not optically active. Therefore, much effort has been done into developing suitable host glass compositions for various rare earth doping

levels. Some of the technological limitations for the development of new glasses are due to the rare earth ion density required for laser action. Currently, high-power lasers used Nd³⁺-doped phosphate glasses and their nominal Nd doping levels in the range of about 3–4.2 × 10²⁰ cm⁻³.

2.2. Phonon interaction

Since the multiphonon decay process is essentially a competing process to the fluorescence, a low multiphonon decay rate can lead to an increased fluorescence efficiency for many important rare earth transitions. The efficiency of nonradiative transition rate depends on the energy gap between the ground and excited states, as well as the vibrational energy of the oscillators. The nonradiative transition decay rate can be expressed in terms of multiphonon relaxation, concentration quenching, energy transfer to another doping impurity such as transition metal ions or other rare earth ions, and energy transfer to hydroxyl groups OH⁻ [35]. The quenching efficiency is strongly dependent on the number of vibrational quanta that are needed to bridge the gap between the lowest emitting level and the highest nonemitting level of the lanthanide ion. Generally, hosts with low phonon energy tend to have a low multiphonon decay rate; thus, selection of lower phonon hosts such as fluoride or tellurite glasses can reduce the contribution of multiphonon relaxation and allow important radiative transitions.

2.3. Ion-ion interaction

Ion-ion interaction is due to multipolar interactions between neighbor rare earth ions. The analysis of ion-ion interaction and energy transfer provides essential information to the applications of laser glasses and display devices. In such process, the excitation energy transfers from an excited donor to a nearby unexcited activator (acceptor). Many theories have been put forward to give formulas for the rate of energy transfer by electric dipole-dipole interaction ($n = 6$), electric dipole-quadrupole interaction ($n = 8$), and quadrupole-quadrupole interactions ($n = 10$). These transfer mechanisms differ from one another in the dependence of the transfer rate on donor-acceptor distance, but common to all is the condition that an overlap between the donor emission spectrum and the acceptor absorption spectrum is essential for the transfer to occur. Such resonant transfer is analyzed most frequently through luminescence measurements: donor molecules are excited in the presence of acceptor ions, and the luminescence yield of donor and/or acceptor and the decay time of donor luminescence are measured as functions of the acceptor concentration. A more detailed description of ion-ion interactions is given by Inokuti-Hirayama theory [36], which explicitly deals with the dynamics of energy migration.

Among many energy transfer theories, Förster [37] and Dexter [38] theory on energy transfer is one of the most widely employed and the probability rate of energy transfer can be determined as [39] follows:

$$W_{DA}(R) = \frac{6c g_{low}^D}{(2\pi)^4 n^2 R^6 g_{up}^D} \sum_{m=0}^{\infty} e^{-(2\bar{n}+1)S_0} \frac{S_0^m}{m!} (\bar{n} + 1)^m \int \sigma_{emis}(\lambda_m^+) \sigma_{abs}(\lambda) d\lambda = \frac{C_{DA}}{R^6} \quad (1)$$

where R is the distance of separation between donor and acceptor, C_{DA} is the energy transfer constant (cm^6/s), and $\bar{n} = [1/e(\hbar\omega_0/KT) - 1]$ is the average occupation of phonon mode at temperature T . Then, the energy transfer constant is expressed as follows:

$$C_{DA} = \frac{6cg_{low}^D}{(2\pi)^4 n^2 g_{up}^D} \sum_{m=0}^{\infty} e^{-(2\bar{n}+1)S_0} \frac{S_0^m}{m!} (\bar{n} + 1)^m \int \sigma_{emis}(\lambda_m^+) \sigma_{abs}(\lambda) d\lambda \quad (2)$$

The critical radius of the interaction can be obtained by the product of energy transfer constant and intracenter lifetime of the donor excited level (i.e., $R_C^6 = C_{DA} \times \tau_D$).

In addition to the aforementioned mechanisms, in glasses containing only one RE^{3+} species (for example Nd^{3+} , Er^{3+}), a number of different ion-ion interactions occur such as energy migration, cross-relaxation among others. The most important are outlined below.

2.4. Energy migration

Energy migration is strongly dependent on rare earth ion concentration and due to the dipole-dipole Förster and Dexter interactions. An excited ion in the metastable state can interact with the nearby ground state ion then promoting it to the excited level (see **Figure 3**). The successive energy transfers between the ions increase the probability of nonradiative decay that lead to decrease the fluorescence efficiency [40, 41].

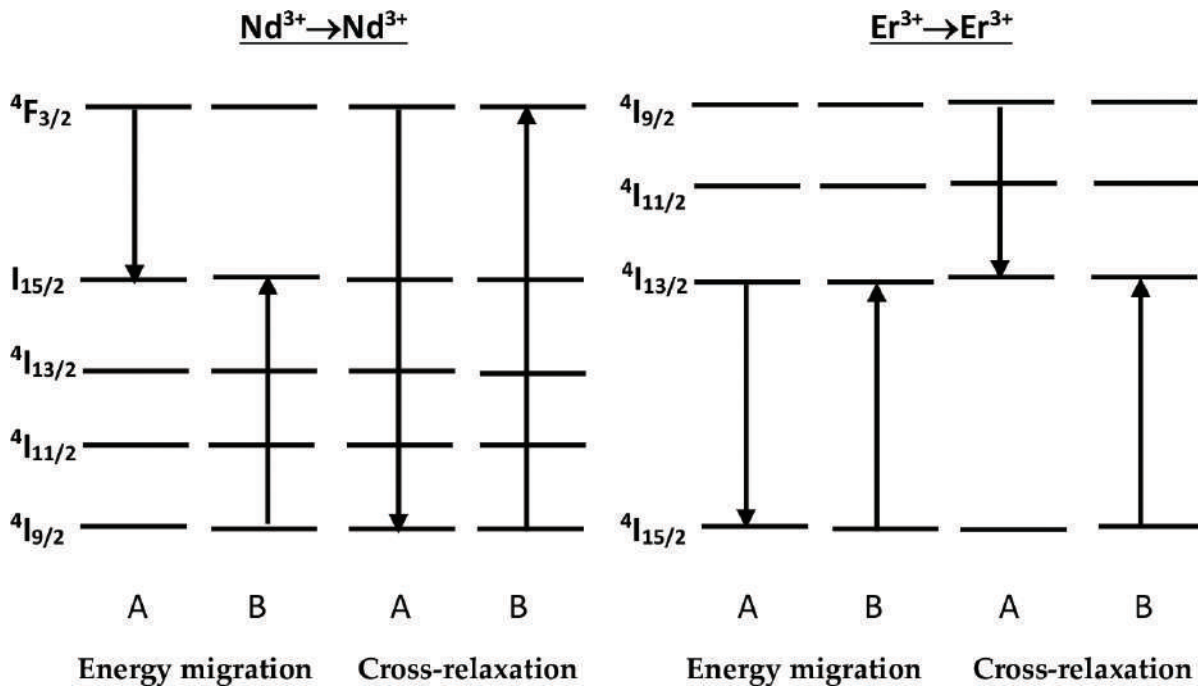


Figure 3. Schematic diagram of ion-ion interaction in the case of Nd^{3+} and Er^{3+} ions.

2.5. Cross relaxation

Cross relaxation involves the same RE ions and their schematic representation, which is shown in **Figure 3**. An excited state of ion A that gives half its energy to ion B is in its ground state. So that both ions end up in the intermediate energy level, from which they relax rapidly to the ground state through nonradiative relaxation. This relaxation is usually observed for Nd³⁺-doped glasses that cause concentration quenching.

2.6. Upconversion mechanisms

By *Excited State Absorption (ESA)*: The simplest representation of upconversion mechanism in trivalent Er³⁺ ion through the ground-state absorption (GSA)/excited state absorption (ESA) is shown in **Figure 4a**. The first excitation photon is absorbed by the ground-state N₀ and populates the intermediate-state N₁. Provided the lifetime of N₁ is long enough, a second incident photon can be absorbed, exciting further the ion from its intermediate-state N₁ to a higher-lying excited state N₂, from which upconversion luminescence arises.

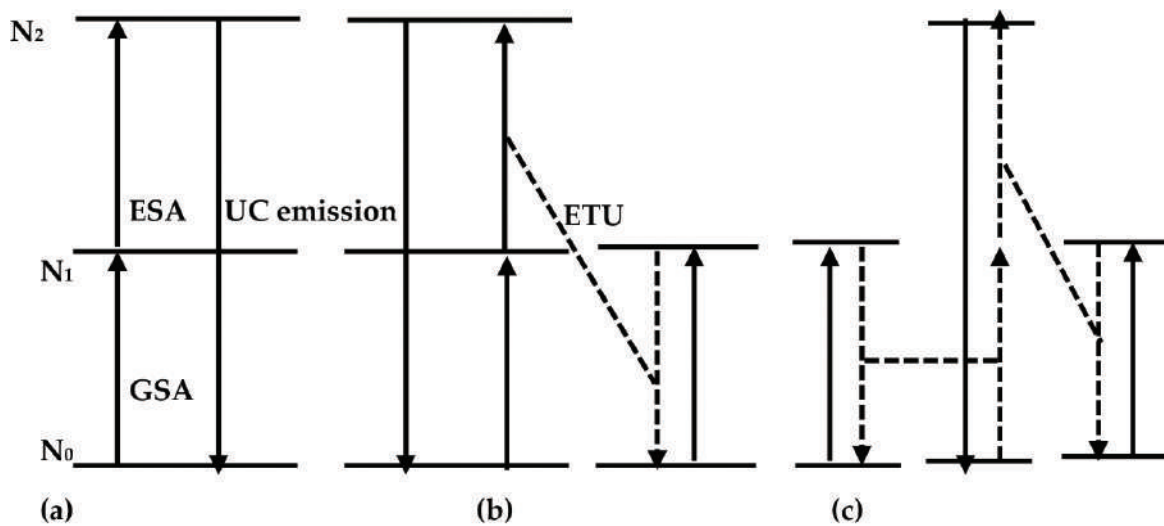


Figure 4. Schematic representation of upconversion mechanisms. (a) GSA/ESA process; (b) ETU process; (c) cooperative process.

By *sensitized energy transfer upconversion (ETU)*: Sensitized energy transfer upconversion was first introduced by Auzel who called ETU from Addition of Photon for Energy Transfer (APTE) from (the French 'Addition de Photons par Transferts d 'Energie'). Upconversion involves nonradiative energy transfers between a sensitizer (e.g., Yb³⁺) and an activator (e.g., Er³⁺, Ho³⁺, Tm³⁺). Usually, sensitizer has a strong absorption cross section at the excitation wavelength. Once the sensitizer is excited (after absorption of an incident photon), it relaxes to a lower-energy state (the ground state in the case of Yb³⁺) by transferring its energy to a neighboring activator, raising the latter to a higher-energy state (see **Figure 4b**). These energy transfer processes are generally based on electric dipole-dipole interactions.

By *cooperative luminescence*: **Figure 4c** shows the schematic representation upconversion by cooperative luminescence. Two excitation photons sequentially absorbed by two different ions (e.g., two Yb^{3+} ions, but the two ions do not need to be the same species), moving both of them into their excited state. Then, both ions decay simultaneously to their ground state, with the emission of one single photon that contains the combined energies of both ions. The cooperative emission occurs from a virtual level, and it explains why the emission probability is rather low.

3. Spectroscopic properties of Nd^{3+} -doped phosphate glasses

3.1. Judd-Ofelt theory and intensity parameters

Optical spectroscopy often used to measure optical absorption of trivalent rare earth ions in UV-vis-NIR regions, from which the effect of a host matrix on the local environment of a given rare earth cation with its first neighbor anions such as oxygen can be elucidated using the theory proposed by Judd [42] and Ofelt [43]. Each observed transition corresponds to a transition between two spin-orbit coupling levels. The Judd-Ofelt theory has been applied for the interpretation of these transitions by the three mechanisms: (1) magnetic dipole transitions, (2) induced electric dipole transitions, and (3) electric quadrupole transitions. The quantitative analysis of the intensities of these f-f transitions in the rare earth ions has been provided independently by Judd [42] and Ofelt [43]. The basic idea of Judd and Ofelt is that the intensity of f-f electric dipole transitions can arise from the admixture into the $4f^N$ configuration of opposite parity (e.g., $4f^{N-1}n^1d^1$ and $4f^{N-1}n^1g^1$). According to Judd-Ofelt theory, the intensity of magnetic and electric dipole transition is represented as follows:

$$f_{\text{cal}} = f_{ed} + f_{md} \quad (3)$$

This means that experimentally measured oscillator strengths could be expressed to a good approximation in terms of absorption of light by electric dipole (f_{ed}) and magnetic dipole mechanisms. But, the order of magnitude of magnetic dipole oscillator strengths (f_{md}) is found to be very low for the observed intensities of rare earth ions and thus will not be considered further. The calculated oscillator strengths are therefore approximately equal to electric dipole oscillator strengths, that is

$$f_{\text{cal}} = f_{ed} = \sum_{\lambda=2,4,6} T_{\lambda} \nu \left| \left\langle (S, L) J \left\| U^{\lambda} \right\| (S', L') J' \right\rangle \right|^2 \quad (4)$$

where ν is the mean energy of the transition $\psi J \rightarrow \psi' J'$, and $\|U^{\lambda}\|^2$ is the squared reduced matrix element of the unit tensor operator of the rank, λ (=2, 4 and 6). T_2 , T_4 , and T_6 are related to the

radial part of $4f^N$ wave functions, the refractive index of the medium, and the ligand-field parameters that characterize the environment of the ion. These quantities are treated as parameters and are determined from the experimental oscillator strengths.

The intensity of an absorption band is expressed in terms of a quantity called the “oscillator strength.” Experimentally, the oscillator strength (f) is a measure of the intensity of an absorption band and is proportional to the area under the absorption peak. The area under an absorption peak is a better measure of the intensity than the molar absorptivity at the peak maximum, because the area is the same for both the resolved and unresolved band. The oscillator strength (f) of each absorption band is expressed in terms of absorption coefficient $\alpha(\lambda)$ at a particular wavelength λ and is given by [44]

$$f_{\text{exp}} = \frac{mc^2\nu^2}{N\pi e^2} \int \varepsilon(\nu) d\nu \quad \text{or} \quad f_{\text{exp}} = 4.32 \times 10^{-9} \int \varepsilon(\nu) d\nu \quad (5)$$

where m and e are the mass and charge of the electron, c is the velocity of light, and N is the density of the absorbing ions obtained from the rare earth ion concentration and glass density values, respectively. $\int \varepsilon(\nu) d\nu$ represents the area under the absorption curve. The molar absorptivity $\varepsilon(\nu)$ of an absorption band at energy ν (cm^{-1}) is given by

$$\varepsilon(\nu) = (Cl)^{-1} \log\left(\frac{I_0}{I}\right) \quad (6)$$

where C concentration of rare earth ions per unit volume, l optical path length, and $\log\left(\frac{I_0}{I}\right)$ is the optical density.

As an example, optical absorption measurements were made at room temperature in the wavelength region 300–900 nm for an Nd^{3+} -doped phosphate glass using JASCO V-630, UV-vis spectrophotometer. **Figure 5** shows (a) absorption and (b) emission spectra of Nd^{3+} -doped phosphate glass. The validity of Judd-Ofelt theory is determined by the root-mean-square (δ_{rms}) deviation between the measured and calculated oscillator strengths by the relation [45].

$$\delta_{\text{rms}} = \left[\frac{\sum (f_{\text{exp}} - f_{\text{cal}})^2}{P} \right]^{1/2} \quad (7)$$

Using the experimental oscillator strengths (f_{exp}), a best set of Judd-Ofelt intensity parameters Ω_λ ($\lambda = 2, 4,$ and 6) for the Nd^{3+} ion-doped glass were determined using the procedure followed in Ref. [46]. The Judd-Ofelt intensity parameters represent the square of the charge displacement due to the induced electric dipole transition. The advantage of Ω_λ parameters is that a

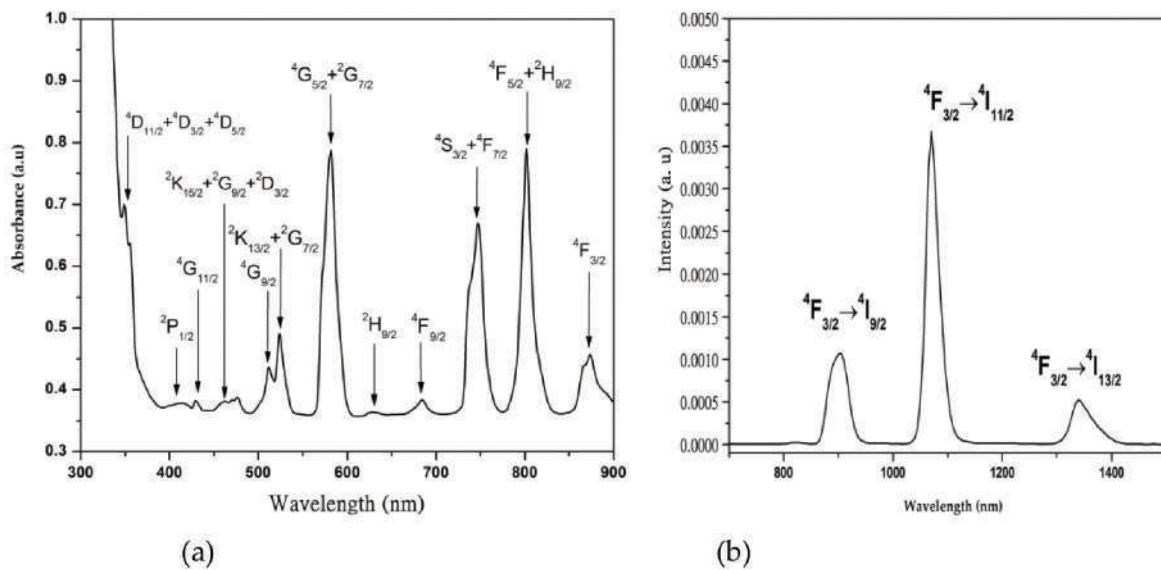


Figure 5. (a) Absorption and (b) emission spectra of Nd³⁺-doped phosphate glass [33].

set of parameters is needed for describing both the absorption and emission processes. The Ω_λ parameters are important for the investigation of the local structure and bonding in the vicinity of rare earth ions. Reisfeld [47] indicated that Ω_2 parameter is sensitive to both asymmetry and covalency at rare earth sites. Oomen and van Dongen [48] pointed out that the rigidity or long range effects of glass hosts were responsible for changes in Ω_6 . The Ω_4 parameters are affected by factors causing changes in both Ω_2 and Ω_6 . **Table 3** shows Judd-Ofeldt intensity parameters Ω_λ ($\lambda = 2, 4,$ and 6) for the Nd³⁺-ion doped various phosphate glasses.

Glass matrix	Ω_2	Ω_4	Ω_6	Ω_4/Ω_6
40P ₂ O ₅ -20Al ₂ O ₃ -40Na ₂ O [49]	4.70	6.0	5.40	1.11
41P ₂ O ₅ -17K ₂ O-9.5CaO-8Al ₂ O ₃ -24aF ₂ [50]	5.40	7.03	6.51	1.07
58.5P ₂ O ₅ -17K ₂ O-14.5SrO ₂ -9Al ₂ O ₃ [51]	6.74	3.86	6.35	0.60
75NaPO ₃ -24LiF ₃ [52]	3.44	4.14	6.28	0.65
(65P ₂ O ₅ -15Na ₂ O)-15Li ₂ O [45]	4.32	3.66	6.00	0.61
(65P ₂ O ₅ -15Na ₂ O)-15Na ₂ O [45]	5.42	4.93	8.06	0.61
(65P ₂ O ₅ -15Na ₂ O)-15K ₂ O [45]	7.68	8.96	11.71	0.76
(65P ₂ O ₅ -15Na ₂ O)-7.5Li ₂ O-7.5Na ₂ O [45]	4.01	3.69	5.92	0.62
(65P ₂ O ₅ -15Na ₂ O)-7.5Li ₂ O-7.5K ₂ O [45]	6.42	6.15	8.96	0.69
(65P ₂ O ₅ -15Na ₂ O)-7.5Na ₂ O-7.5K ₂ O [45]	4.90	3.88	6.18	0.63

Table 3. Judd-Ofeldt intensity parameters (Ω_λ , $\lambda = 2, 4,$ and 6×10^{-20} cm²) in 1 mol% Nd₂O₃-doped phosphate glasses.

The covalency between the rare earth ion and the surrounding oxygen in the glass modifies the intensity of hypersensitive transitions (HST), as suggested by Reisfeld and co-worker [47,

48]. This can be observed more clearly in RE³⁺-doped alkali- and mixed alkali-based glasses. For example, in Nd³⁺ ion, the transition ⁴I_{9/2} → ⁴G_{5/2} + ²G_{7/2} is found to be hypersensitive by selection rule, ΔJ ≤ 2, ΔL ≤ 2, and ΔS = 0. The observed oscillator strengths of the hypersensitive transition are higher when compared to other bands (see inset **Figure 5a**). **Figure 6** shows variation of J-O parameter, Ω₂ with (a) oscillator strength (b) energy (cm⁻¹) of HST transition of Nd³⁺ ion for alkali, mixed alkali phosphate glasses. From **Figure 6a**, among the alkali glass matrices, the oscillator strength of HST is found to be lower in lithium phosphate glass matrix and higher in potassium glass matrix. But the oscillator strength of HST is found to be higher in lithium-potassium phosphate glass matrix among the mixed alkali glass matrices. Thus, the results of oscillator strength show that potassium is playing active role in enhancing the oscillator strengths of Nd³⁺ ion in potassium phosphate glass matrices (K, Li-K, and Na-K) compared to other glass matrices. In lithium phosphate glass matrix, oscillator strength of HST indicates the lower crystal field symmetry at Nd³⁺ ion site.

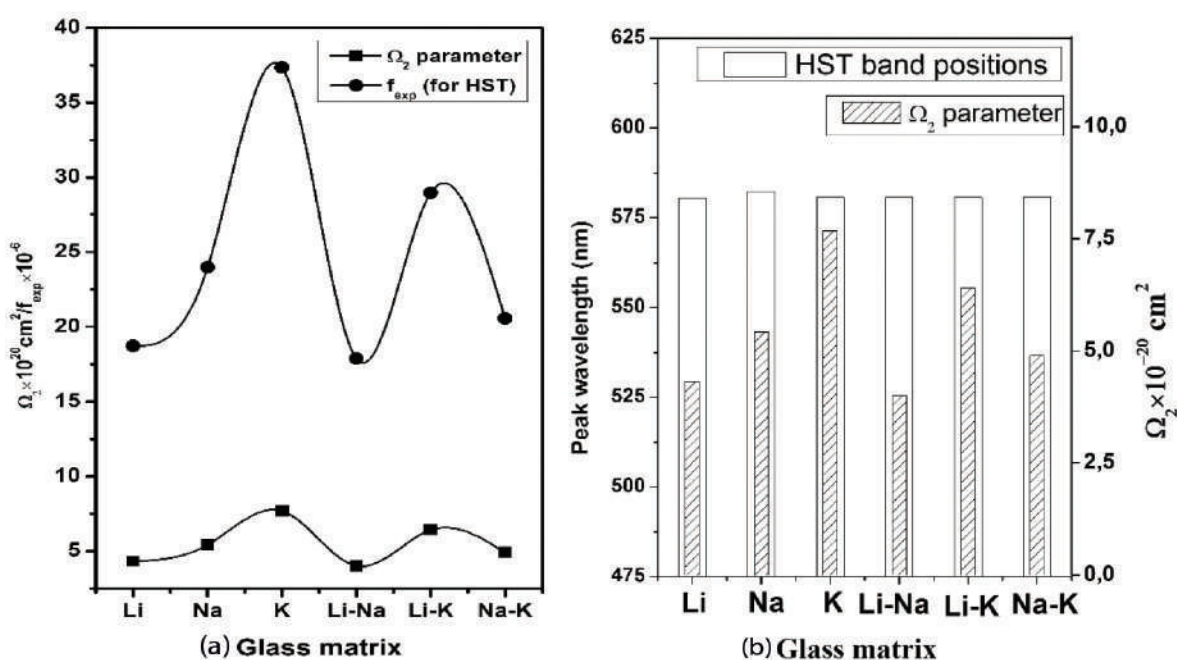


Figure 6. Variation of (a) Ω₂ with oscillator strength (f_{exp}) of HST and (b) Ω₂ with band position (E_{exp}) of HST in alkali and mixed alkali phosphate glasses [45].

The hypersensitive transition can also give the information regarding the covalency nature of rare earth-ligand interaction, which can be determined by the shift of hypersensitive band position to lower or higher wavelength due to nephelauxetic effect. From **Figure 6b**, it is observed that for lithium to sodium glass matrices, the peak wavelength of HST shifts toward higher wavelength side and the Ω₂ parameter also increases indicating that the structural changes are not influencing the covalence bond. For lithium to potassium and lithium-potassium glass matrices, the peak wavelength of HST does not change but the Ω₂ parameter increased indicating that the some structural changes are influencing the Nd-O bond. For sodium to potassium and sodium-potassium glass matrices, the peak wavelength of HST shifts

toward lower wavelength side but Ω_2 parameter increased (for Na to K) and decreased (for Na to Na-K) indicating that the structural changes are influencing the Nd-O bond.

Due to the zero values of certain reduced matrix elements $\|U^\lambda\|$ of Nd^{3+} ion, certain lasing transitions can be uniquely characterized by the ratio of intensity parameters Ω_4 and Ω_6 , which is known as spectroscopic quality factor (χ) and are shown in **Table 2**. If $\chi < 1$, the ${}^4\text{F}_{3/2} \rightarrow {}^4\text{I}_{11/2}$ transition shows stronger intensity than that of ${}^4\text{F}_{3/2} \rightarrow {}^4\text{I}_{9/2}$ transition. From the **Table 2** data, the obtained χ value is < 1 for Nd^{3+} -doped phosphate glasses, indicating that the intensity of ${}^4\text{F}_{3/2} \rightarrow {}^4\text{I}_{11/2}$ transition at 1064 nm will be stronger for various phosphate glasses [53].

3.2. Fluorescence analysis and radiative properties

The emission spectra of Nd^{3+} -doped phosphate glass recorded at room temperature in the wavelength region 800–1500 nm under excitation wavelength, 514.5 nm of Ar^{3+} laser are shown in **Figure 5b**. Emission spectra show three emission peaks due to the transitions, ${}^4\text{F}_{3/2} \rightarrow {}^4\text{I}_{9/2}$, ${}^4\text{F}_{3/2} \rightarrow {}^4\text{I}_{11/2}$, and ${}^4\text{F}_{3/2} \rightarrow {}^4\text{I}_{13/2}$ nearly centered at 902, 1069, and 1340 nm, respectively. The stimulated emission cross section is an important parameter and its value is related to the rate of energy extraction from the optical material. The Judd-Ofelt theory can be applied to laser glasses and can successfully account for the induced emission cross sections that are observed.

The efficiency of a laser transition is evaluated by considering the stimulated emission cross section, and it is related to the radiative transition probability. It can be obtained from the emission spectra using Fuchtbauer-Ladenburg method [54]

$$\sigma_p = \frac{\lambda_p^4}{8\pi c n^2 \Delta\lambda_{\text{eff}}} A_{\text{rad}}(J \rightarrow J') \quad (8)$$

where λ_p is peak wavelength, and $\Delta\lambda_{\text{eff}}$ is the effective line width. The effective line width $\Delta\lambda_{\text{eff}}$ is obtained from

$$\Delta\lambda_{\text{eff}} = \int \frac{I(\lambda)}{I_{\text{max}}} d\lambda \quad (9)$$

where $I(\lambda)$ is the integrated fluorescence intensity and I_{max} is the peak fluorescence intensity. The radiative transition probability $A_{\text{rad}}(\psi J, \psi' J')$ for emission from an initial excited state ψJ to a final ground state $\psi' J'$ is

$$A_{\text{rad}}(J \rightarrow J') = \frac{64\pi^4 e^2}{3h(2J+1)\lambda^3} \left[\frac{n(n^2+n)^2}{9} S_{\text{ed}} \right] \quad (10)$$

Where the factor $\frac{n(n^2 + 2)^2}{9}$ represents the local field correction term for the ion in a medium, ν is the energy of transition, and n is the refractive index of the glass.

The radiative lifetime (τ_R) of an excited state $\psi'J'$ is calculated from

$$\tau_R(J) = \frac{1}{\sum_{J'} A(J \rightarrow J')} \quad (11)$$

The fluorescence branching ratio, β_R , predicts the relative intensity of lines from a given excited states and characterizes the lasing potency of that particular transition. In order to choose suitable lasing transition, one has to select the transition having branching ratio >0.5 and the energy difference of about 3000 cm^{-1} between the emitting level and the next lower level. The fluorescence branching ratio (β_R) is given by

$$\beta_R(J \rightarrow J') = \frac{A(J \rightarrow J')}{\sum_{J'} A(J \rightarrow J')} \quad (12)$$

Table 4 shows critical parameters to the laser designer such as branching ratios and radiative life times, peak stimulated emission cross sections of 1062 nm laser line in various phosphate glasses.

Glasses	τ_{exp} (μs)	τ_{rad} (μs)	η (%)	β_{rad} (%)	$\Delta\lambda$ (nm)	σ_p (cm^2)
55P ₂ O ₅ -17K ₂ O-11.5BaO-6BaF ₂ -9Al ₂ O ₃ [55]	210	189	90	59	25.1	6.23
58.5P ₂ O ₅ -17K ₂ O-14.5MgO-9Al ₂ O ₃ [56]	262	249	74	68	28.8	4.41
57P ₂ O ₅ -14.5K ₂ O-28.5BaO [57]	178	430	41	53	29.3	2.78
0.4MgO-0.4BaF ₂ -0.1Al(PO ₃) ₃ -0.1Ba(PO ₃) ₃ (wt.%) [58]	185	308	60	49	32	2.97
APG1 [59]	385	361	106	–	27.8	3.4
APG2 [59]	464	456	101	–	31.5	2.4
HAP4 [60]	350	–	–	–	27.0	3.6
HAP3 [60]	380	372	102	–	27.9	3.2
Q89 [61]	350	–	–	–	21.2	3.8

τ_{exp} : radiative life time; τ_{rad} : radiative lifetime from J-O theory; η : quantum efficiency; β : branching ratio; σ_p : peak emission cross section ($\times 10^{22} \text{ cm}^2$). (APG1, APG2, HAP4, HAP3, and Q89 are commercial phosphate glasses).

Table 4. Laser emission properties at 1060 nm of Nd³⁺-doped phosphate glasses

4. Rare earth-doped optical amplifiers

Rare earth-doped fibers have received growing attention recently. They can be used as amplifiers in optical communication systems and as optical sources. Optical amplifiers amplify an incident weak light signal through the process of stimulated emission. The main ingredient of any optical amplifier is the optical gain realized when the amplifier is optically pumped to achieve population inversion. The optical gain, in general, depends mainly on the doping material, on the frequency (or wavelength) of the incident signal, and also on the local beam intensity at any point inside the amplifier. By a proper choice of the doping materials, the amplifier characteristics such as the operating wavelength and the gain bandwidth can be modified. Many different dopants such as erbium (Er^{3+}), holmium (Ho^{3+}), neodymium (Nd^{3+}), samarium (Sm^{3+}), thulium (Tm^{3+}), and ytterbium (Yb^{3+}) can be used to realize fiber amplifiers operating at different wavelengths covering a wide region extending over 0.5–3.5 μm and the most commonly used hosts are silicate, phosphate, fluoride, and tellurite glasses. **Figure 7** shows working of active fibers within a specific wavelength range determined by various rare earth ions. Specially, optical telecommunication transmission [wavelength division multiplexing (WDM)] systems work in the conventional C-band (1530–1565 nm) telecommunication window. This band can easily be observed in erbium (Er^{3+}) ions among the rare earths and is the most useful dopant for commercial optical amplifiers and erbium-doped fiber amplifiers (EDFAs) that are made from silicate and phosphate glass matrices. The schematic representation of Er^{3+} -doped fiber amplifiers (EDFA) is shown in **Figure 8**. An erbium-doped fiber is pumped optically by an infrared laser sources at 980 or 1480 nm and are compatible with InGaAs and InGaAsP laser diodes. The three-level pumping process in EDF is illustrated in **Figure 9**.

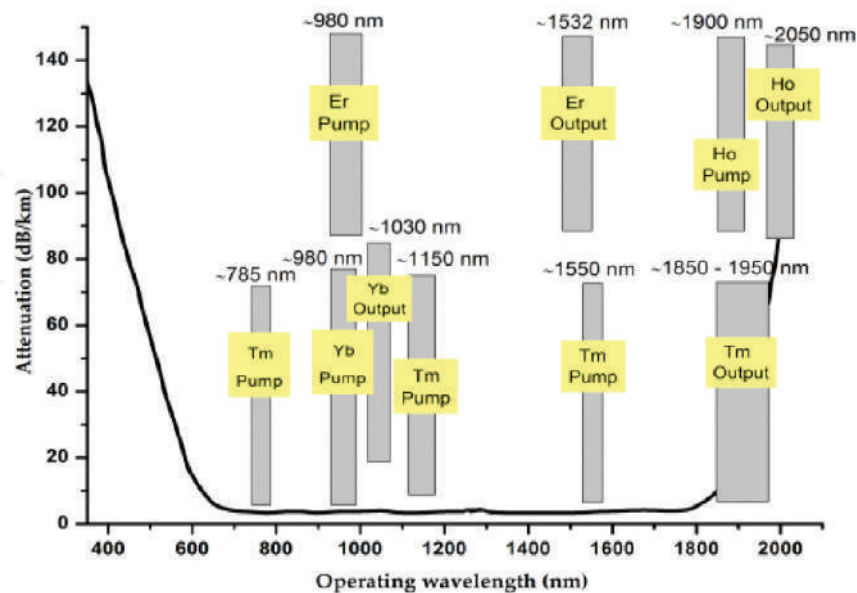


Figure 7. Rare earth-doped fibers working wavelength ranges.

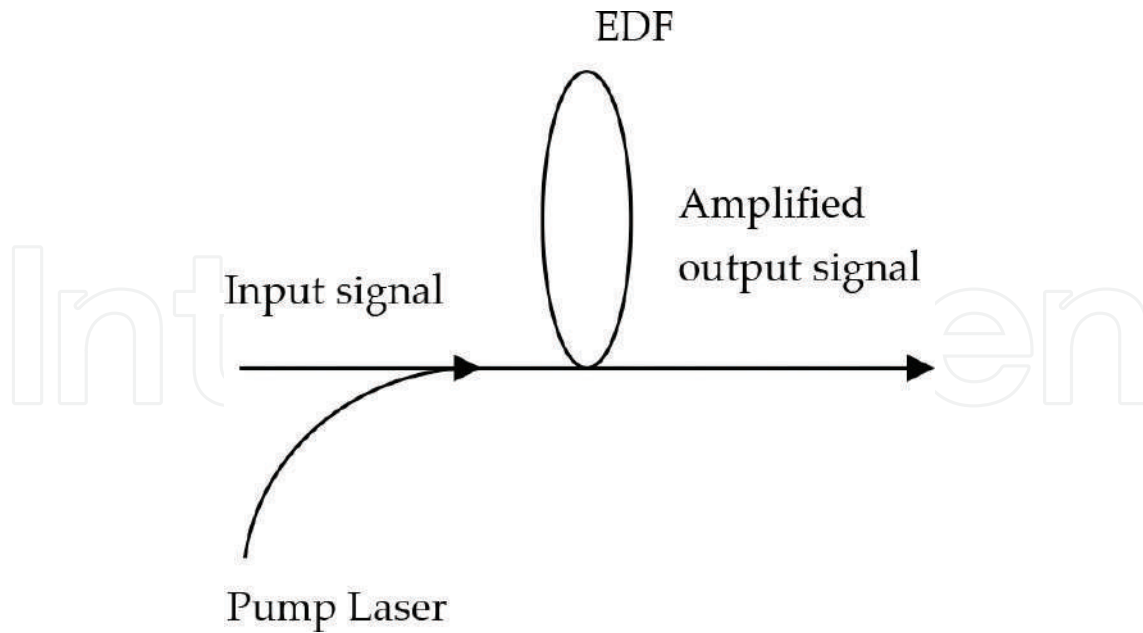


Figure 8. Erbium-doped fiber amplifier (EDFA).

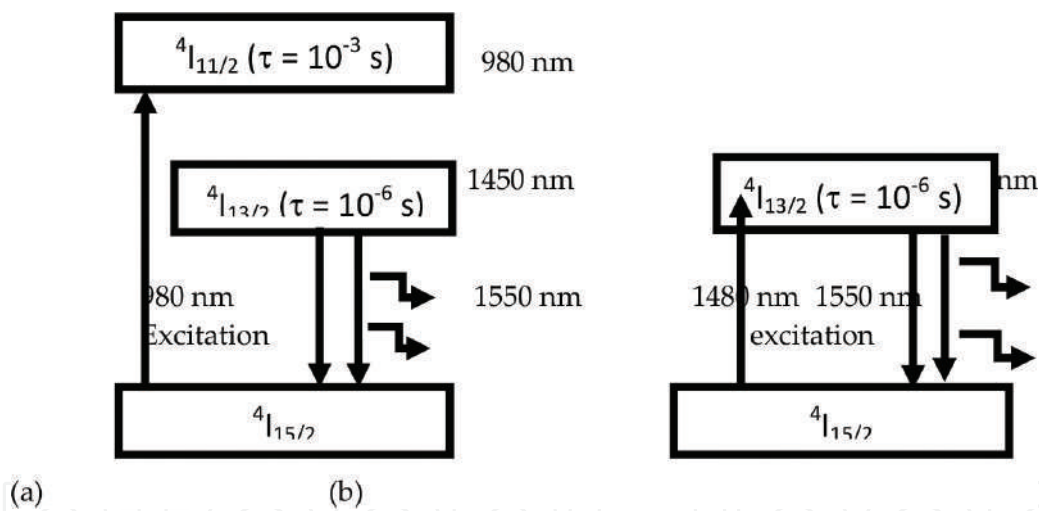


Figure 9. Simplified energy band diagram of Er^{3+} -doped silica fiber. (a) Three-level process. (b) Two-level process.

When a laser source tuned at 980 nm is used to pump the EDF, the Er^{3+} ions move from ground level ($4I_{15/2}$) to excited level ($4I_{11/2}$). The ions stay excited level only about 10^{-6} s and after that they decay into a metastable level through multirelaxation process. In this process, the energy loss is turned into mechanical vibrations in the fiber. Finally, ions stay in the order of 10^{-3} s in metastable level, which is longer than the ion lifetime in the excited level and decay to the ground level with emission of photons in the 1530 nm wavelength region. Therefore, under 980 nm pumping, almost all the ions will be accumulated in the metastable level, and the three-level system can be simplified into two levels for most of the practical applications, as shown in **Figure 9b**. Whereas in the case of 1480 nm wavelength pumping, ions excited from ground

level to the metastable level directly. Therefore, 1480 nm pumping is more efficient than 980 nm pumping because it does not involve the nonradiative transition and is often used for high-power optical amplifiers. However, amplifiers with 1480 nm pump usually have higher noise than the ones pumped at 980 nm.

Optical pumping provides the necessary population inversion between the energy levels E_1 and E_2 , which in turn provides the optical gain defined as $g = \sigma(N_2 - N_1)$, where σ is the transition cross section. Normally, in laser and amplifiers, the gain coefficient decreases as signal power increases and is called as gain saturation. The gain coefficient can be defined as [62] follows:

$$G = G_0 \left(\frac{P_s}{P_s - P} \right), \quad (13)$$

where G_0 is the small-signal gain coefficient at a given wavelength, P is the signal power, and P_s is the saturated signal power. The absorption and broadened gain spectra of EDFA (see **Figure 10**) are the advantages for Wavelength Division Multiplexing (WDM) applications.

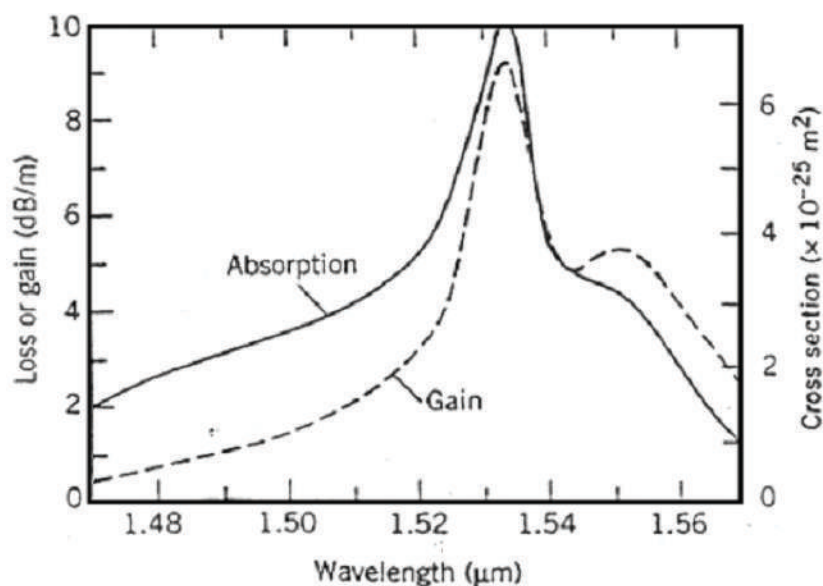


Figure 10. Absorption and gain spectra of EDFA.

Wave division multiplexing optical transmission system requires a flat gain spectrum of EDFA across the whole usable bandwidth. It is difficult to achieve the gain flatness in WDM system because EDFA has the narrow high gain in the C-hand wavelength region (1530–1570 nm) centered at 1550 nm. In recent decades, many glass hosts for Er^{3+} ions have been investigated to realize the optical amplifier. For the flattened gain performance of optical amplifier, Er^{3+} -doped fluoride [63], tellurite [64], and bismuth [65] based glasses are capable of realizing a flat gain over a broadband width of 1530–1560 nm.

5. Luminescent solar concentrators (LSC)

A schematic of luminescent solar concentrator (LSC) is shown in **Figure 11a**. LSC is working based on the absorption of sun light by a transparent material that has been doped with high quantum efficiency luminescent ions and subsequently re-emit by transparent material. The resulting luminescence is propagate by total internal reflection in transparent material and concentrated onto the solar cell, which attached to the edge of the transparent material to convert trapped emission light into electricity. The LSC was first proposed in late 1970s [66]. A typical design consists of a polymer plate doped with a luminescent material, such as a fluorescent organic dye, with solar cells optically matched to the plate edges. In recent decades, luminescent transparent material extends to availability of inorganic luminescence materials such as semiconductor quantum dots (QDs) [67], rare earth-doped materials [68] and semiconductor polymers [69]. Particularly, rare earth-doped glasses are still great interest due to their potential use as solid-state lasers and luminescence solar concentrators.

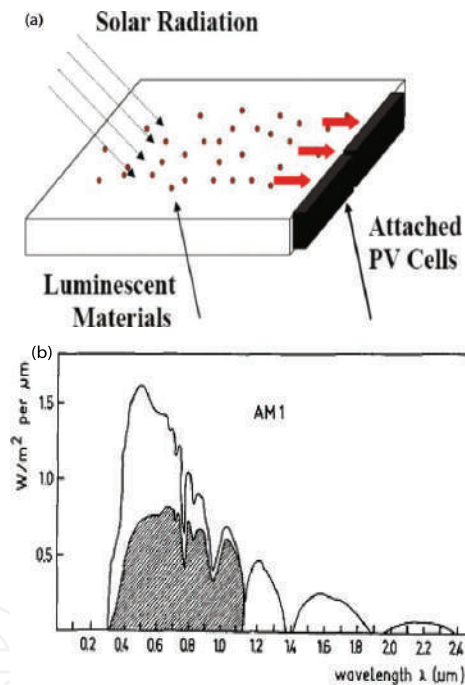


Figure 11. (a) Schematic diagram of luminescent solar concentrator. (b) Emission of solar radiation.

Figure 11b shows emission spectra of (AM1) solar radiation. It is known that the efficiency of solar cell is mainly limited by the loss of photons with much higher energy than the band gap of the photovoltaic solar cell. Normally, photovoltaic cells are made with silicon, which absorb photons only with energy greater than 1.1 eV and it is improving the performance of LSC. The luminescent material usually absorbs all wavelengths below 950 nm. Above 950 nm, the luminescence consists of a strong emission band in the range from 950 to 1000 nm [70]. This region is more reliable to increase the spectral response of the Si Photo-voltaic cell in LSC (see shaded region in figure). In addition the number of photons in the LSC is double while

extending the absorption from visible (300–600 nm) out to the NIR (300–900 nm) range. The extending wavelength increased nonradiative recombination due to increasing molecular dimensions and decreasing probability of radiative transitions [71]. This leads to decrease in fluorescence quantum yield (FQY). In rare earth-doped materials, the FQY vary greatly depending on host materials and concentration, but values >90% have been reported in glass substrates [71]. The FQY is defined as follows:

$$\eta_{FQY} = \frac{\text{No. of emitted photons}}{\text{No. of absorbed photons}} \times 100\% \quad (14)$$

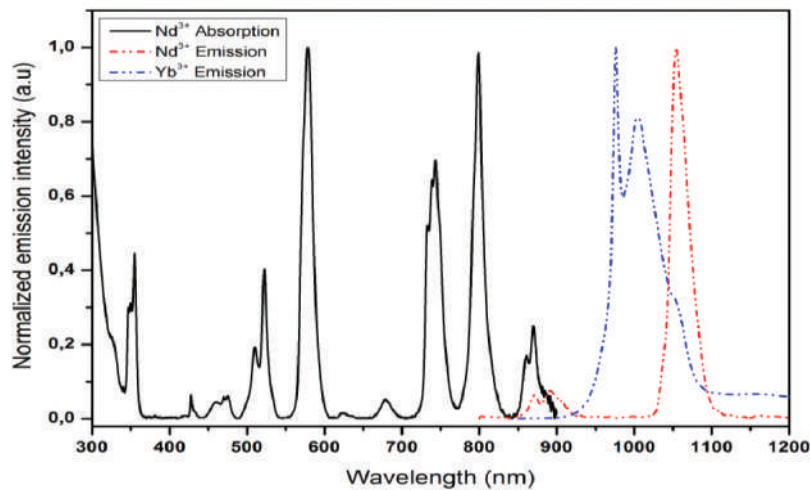


Figure 12. Absorption and emission spectra of Nd^{3+} and Yb^{3+} ions.

A high quantum yield (~95–100%) is essential for good LSC performance. Rare earth ions such as neodymium (Nd^{3+}) and ytterbium (Yb^{3+}) in glassy hosts exhibit high FQY (~90%) values due to range at 800–1300 nm (Nd^{3+}) and 1000 nm (Yb^{3+}) emission peaks. When $\text{Nd}^{3+}/\text{Yb}^{3+}$ co-doped glasses are used as LCS, Nd^{3+} acts as sensitizer due to its numerous absorption bands in visible region, and Yb^{3+} acts as activator due to its single emission peak at ~1000 nm. Moreover, this material absorbs 20% of the solar spectrum in the range 440–980 nm range [72]. **Figure 12** shows absorption (for Nd^{3+}) and emission (for Nd^{3+} , Yb^{3+}) spectra for realizing the LCS. It is observed that the emission peak at ~1000 nm is matched perfectly to the maximum spectral response of a Si-Solar cell.

6. Conclusions

In summary, this chapter consists of a brief discussion on electronic energy-level structure of RE^{3+} in solids, structural features, and general considerations in lasers glasses such concentration quenching, phonon interaction, ion-ion interaction, and upconversion mechanisms. Judd-Ofelt intensity parameters (Ω_λ , $\lambda = 2, 4, \text{ and } 6$) on Nd^{3+} -doped phosphate glasses and relevant

theory were considered. We also included a study on the covalency between rare earth ion and the surrounding oxygen in the glass that increases the intensity of hypersensitive transitions for the case of alkali- and mixed alkali phosphate-based glasses. Laser parameters such as emission cross sections (σ_p), radiative lifetime (τ), branching ratios (β), peak bandwidth ($\Delta\lambda$), and quantum efficiency on Nd³⁺-doped phosphate glasses are reported. Laser emission process in three-level and two-level-based silica-EDFA was discussed as well as significant features of rare earth-doped luminescent solar concentrators.

Acknowledgements

The authors would like to thank to Conselho Nacional de Desenvolvimento Científico e Tecnológico (CNPq) and Coordenação de Aperfeiçoamento de Pessoal de Nível Superior (CAPES), PNPd/CAPES, and FAPEMIG.

Author details

Meruva Seshadri*, Virgilio de Carvalho dos Anjos and Maria Jose Valenzuela Bell

*Address all correspondence to: seshumeruva@gmail.com

Departamento de Física – ICE, Laboratorio de Espectroscopia de Materiais, Universidade Federal de Juiz de Fora, Juiz de Fora, Minas Gerais, Brazil

References

- [1] Moulton P.F. Laser Hand Book, 5th ed. M. Bass and M. L. Stitch. Netherland Publishers: Amsterdam; 1985. 203 p.
- [2] Sutton D. Electron Spectra of Transition Metal Complexes. McGraw-Hill Publishing Company Ltd: New York; 1969.
- [3] Belançon M.P., Marconi J.D., Ando M.F., Barbosa L.C. Near-IR emission in Pr³⁺ single doped and tunable near-IR emission in Pr³⁺/Yb³⁺ codoped tellurite tungstate glasses for broadband optical amplifiers. *Opt. Mater.* 2014; 36: 1020–1026. doi:10.1016/j.optmat.2014.01.014
- [4] Balakrishna A., Rajesh D., Ratnakaram Y.C. Structural and optical properties of Nd³⁺ in lithium fluoro-borate glass with relevant modifier oxides. *Opt. Mater.* 2013; 35: 2670–2676. doi:10.1016/j.optmat.2013.08.004

- [5] Vishwakarma A.K., Jayasimhadri M. Significant enhancement in photoluminescent properties via flux assisted Eu^{3+} doped BaNb_2O_6 phosphor for white LEDs. *J. Alloys Compound*. 2016; 683: 379–386. doi:10.1016/j.jallcom.2016.05.052
- [6] Gao Y., Hu Y., Ren P., Zhou D., Qiu J. Phase transformation and enhancement of luminescence in the Tb^{3+} - Yb^{3+} co-doped oxyfluoride glass ceramics containing NaYF_4 nanocrystals. *J. Eur. Ceramic Soc*. 2016; 36: 2825–2830. doi:10.1016/j.jeurceramsoc.2016.04.027
- [7] Guo H., Liu L., Wang Y., Hou C., Li W., Lu M., Zou K., Peng B. Host dependence of spectroscopic properties of Dy^{3+} - doped and Dy^{3+} , Tm^{3+} -codoped Ge-Ga-SCdI_2 chalcogenide glasses. *Opt. Express*. 2009; 17: 15350–15358. doi:10.1364/OE.17.015350
- [8] Seshadri M., Chillce E.F., Marconi J.D., Sigoli F.A., Ratnakaram Y.C., Barbosa L.C. Optical characterization, infrared emission and visible up-conversion in Er^{3+} doped tellurite glasses. *J. Non-Cryst. Solids*. 2014; 402: 141–148. doi:10.1016/j.jnoncrsol.2014.05.024
- [9] Diek G.H. *Spectra and Energy Levels of Rera Earth Ions in Crystals*. New York, Wiley: 1968.
- [10] Peacock R.D. Rare earths. In: *Structure and Bond*, vol. 22. Springer, Berlin: 1975; p. 83.
- [11] Reisfeld R. Radiative and nonradiative transition of rare earths in glasses. In: *Structure and Bond*, vol. 22. Springer, Berlin: 1975; p. 123.
- [12] Wybourne B.G. *Spectroscopy Properties of Rare earths*. New York, Wiley: 1965.
- [13] ASTM Standards on Glass and Glass Products, prepared by ASTM Committee C14, American Society for Testing Materials, April 1955.
- [14] Shelby J.E. *Introduction to Glass Science and Technology*, 2nd ed. Royal Society of Chemistry; Cambridge: 2005; 291 p.
- [15] Zachariasen W.H. The atomic arrangement in glasses. *J. Am. Chem. Soc*. 1932; 54: 3841–3851.
- [16] Herrmann A., Kuhn S., Tiegel M., Russel C., Korner J., Klopfel D., Hein J., Kaluza M.C. Structure and fluorescence properties of ternary aluminosilicate glasses doped with samarium and europium. *J. Mater. Chem. C*. 2014; 2: 4328–4337. doi:10.1039/C4TC00036F
- [17] Tiegel M., Herrmann A., Russel C., Korner J., Klopfel D., Hein J., Kaluza M.C. Magnesium aluminosilicate glasses as potential laser host material for ultrahigh power laser systems. *J. Mater. Chem. C*. 2013; 1: 5031–5039. doi:10.1039/C3TC30761A
- [18] Seshadri M., Barbosa L.C., Radha M. Study on structural, optical and gain properties of 1.2 and 2.0 μm emission transitions in Ho^{3+} doped tellurite glasses. *J. Non-Cryst. Solids*. 2014; 406: 62–72. doi:10.1016/j.jnoncrsol.2014.09.042

- [19] Van Wazer J.R. Phosphorous and Its Compounds, vol. 1. New York, Interscience; 1958.
- [20] Kordes E., Vogel W., Feterowsky R. Physical chemistry studies About the properties and Feinban of phosphate glasses. *Z. Elektrochem.* 1953; 57: 282.
- [21] Kordes E., Nieder R. *Glasstech.* 1968; 41: 41.
- [22] Kordes E., Vogel W., Feterowsky R. *Z. Elektrochem.* 1953; 57: 282.
- [23] Hench L.L. *Bioceramics. J. Am. Ceram. Soc.* 1991; 74: 1487.
- [24] Volksch G., Hoche T., Szabo I., Holand W., *Glasstech. Ber. Glass Sci. Technol.* 1998; 71: 500.
- [25] Pinheiro A.S., Freitas A.M., Silva G.H., Bell M.J.V, Anjos V., Carmo A.P., Dantas N.O. Laser performance parameters of Yb³⁺ doped UV-transparent phosphate glasses. *Chem. Phys. Lett.* 2014; 592: 164–169. doi:10.1016/j.cplett.2013.12.022
- [26] Silva G.H., Anjos V., Bell M.J.V., Carmo A.P., Pinheiro A.S. Dantas N.O. Eu³⁺ emission in phosphate glasses with high UV transparency. *J. Lumin.* 2014; 154: 294–297. doi: 10.1016/j.jlumin.2014.04.043
- [27] Deutschbein O., Pautrat C., Svirchevsky I.M. Phosphate glasses: New laser materials. *Rev. Phys. Appl.* 1967; 1: 29.
- [28] Abd El-Ati M.I., Higazy A.A. Electrical conductivity and optical properties of gamma-irradiated niobiumphosphate glasses. *J. Mater. Sci.* 2000; 35: 6175. doi:10.1023/A:1026768925365
- [29] Pinheiro A.S., da Costa Z.M., Bell M.J.V., Anjos V., Dantas N.O., Reis S.T. Thermal characterization of iron phosphate glasses for nuclear waste disposal. *Opt. Mater.* 2011; 33: 1975–1979. doi:10.1016/j.optmat.2011.03.050
- [30] Martin S.W. J. Review of the Structures of Phosphate Glasses. *Solid State Chem.* 1991; 28: 163.
- [31] Belliveau T.F., Simkin D.J. On the coordination environment of rare earth ions in oxide glasses: Calcium titanosilicate and sodium aluminosilicate glasses. *J. Non-Cryst. Solids.* 1989; 110: 127. doi:10.1016/0022-3093(89)90249-4
- [32] Babu S., Seshadri M., Reddy Prasad V., Ratnakaram Y.C. Spectroscopic and laser properties of Er³⁺ doped fluoro-phosphate glasses as promising candidates for broad-band optical fiber lasers and amplifiers. *Mater. Res. Bulletin.* 2015; 70: 935–944. doi: 10.1016/j.materresbull.2015.06.033
- [33] Tian Y.M., Shen L.F., Pun E.Y.B., Lin H. High-aluminum phosphate glasses for single-mode waveguide-typed red light source. *J. Non-Cryst. Solids.* 2015; 426: 25–31. doi: 10.1016/j.jnoncrysol.2015.06.015

- [34] Fan B., Point C., Adam J.L., Zhang X., Fan X., Ma H. Near-infrared down-conversion in rare earth-doped chloro-sulfide glass GeS₂-Ga₂S₃-CsCl: Er, Yb. *J. Appl. Phys.* 2011; 110: 13107. doi:10.1063/1.3665638
- [35] Ehrmann P.R., Campbell J.H. Nonradiative energy losses and radiation trapping in neodymium-doped phosphate laser glasses. *J. Am. Ceram. Soc.* 2002; 85: 1061–1069. doi:10.1111/j.1151-2916.2002.tb00223.x
- [36] Goncalves R.R., Carturan G., Montagna M., Ferrari M., Zampedri L., Pelli S., Righini G.C., Ribeiro S.J.L., Messaddeq Y. Erbium-activated HfO₂-based waveguides for photonics *Opt. Mater.* 2004; 25: 131–139. doi:10.1016/S0925-3467(03)00261-1
- [37] Förster T. Zwischenmolekulare Energiewanderung und Fluoreszenz. *Ann. Phys.* 1948; 2: 55–75.
- [38] Dexter D.L. A theory of sensitized luminescence in solids. *J. Chem. Phys.* 1953; 21: 836–850. doi:10.1063/1.1699044
- [39] Tarelho T.V.G. Gomes L., Ranieri I.M. Determination of microscopic parameters for nonresonant energy-transfer processes in rare earth-doped crystals. *Phys. Rev. B.* 1997; 56: 14344. doi:10.1103/PhysRevB.56.14344
- [40] de Sousa D. F., Batalioto F., Bell M.J.V., Oliveira S.L., Nunes L.A.O. Spectroscopy of Nd³⁺ and Yb³⁺ codoped fluorindogallate glasses. *J. Appl. Phys.* 2001; 90: 3308–3313. doi:10.1063/1.1397289
- [41] Batalioto F., de Sousa D.F., Bell M.J.V., Lebullenger R., Hernandez A.C., Nunes L.A.O. Optical measurements of Nd³⁺/Yb³⁺ codoped fluorindogallate glasses. *J. Non-Cryst. Solids.* 2000; 273: 233–238. doi:10.1016/S0022-3093(00)00132-0
- [42] Judd B.R. Optical absorption intensities of rare earth ions. *Phys. Rev.* 1962; 127: 750. doi:10.1103/PhysRev.127.750
- [43] Ofelt G.S. Intensities of crystal spectra of rare earth ions. *J. Chem. Phys.* 1962; 37: 511. doi:10.1063/1.1701366
- [44] Broer L.F.J., Gorter C.J., Hoogschagen J. The intensities and multiple character in the spectra of rare earth ions. *Physica* 1945; XI: 231–250.
- [45] Seshadri M., Venkata Rao K., Lakshmana Rao J., Koteswara Rao K.S.R., Ratnakaram Y.C. Spectroscopic investigations and luminescence spectra of Nd³⁺ and Dy³⁺ doped different phosphate glasses. *J. Lumin.* 2010; 130: 536–543. doi:10.1016/j.jlumin.2009.10.027
- [46] Ratnakaram Y.C., Thirupathi Naidu D., Vijaya Kumar A., Rao J.L. Characterization of Tm³⁺ doped mixed alkali borate glasses - Spectroscopic investigations. *J. Phys. Chem. Solids.* 2003; 64 (12): 2487–2495. doi:10.1016/j.jpics.2003.06.001
- [47] Reisfeld R., Jorgensen C.K. *Lasers and excited states of rare earths.* Berlin, Springer-Verlag; 1977.

- [48] Oomen E.W.J.L., Van Dongen A.M.A. Europium (III) in oxide glasses: dependence of the emission spectrum upon glass composition. *J. Non-Cryst. Solids*. 1989; 111: 205–213. doi:10.1016/0022-3093(89)90282-2
- [49] Martins V.M., Messias D.N., Doualan J.L., Braud A., Camy P., Dantas N.O., Catunda T., Pilla V., Andrade A.A., Moncorgé R. Thermo-optical properties of Nd³⁺ doped phosphate glass determined by thermal lens and lifetime measurements. *J. Lumin.* 2016; 162: 104–107. doi:10.1016/j.jlumin.2015.02.013
- [50] Linganna K., Dwaraka Viswanath C.S., Narro-Garcia R., Ju S., Han W.T., Jayasankar C.K., Venkatramu V. Thermal and optical properties of Nd³⁺ ions in K-Ca-Al fluorophosphate glasses. *J. Lumin.* 2015; 166: 328–334. doi:10.1016/j.jlumin.2015.05.024
- [51] Upendra Kumar K., Babu P., Jang K.H., Jin Seo H., Jayasankar C.K., Joshi A.S. Spectroscopic and 1.06m laser properties of Nd³⁺-doped K-Sr-Al phosphate and fluorophosphate glasses. *J. Alloys and Compd.* 2008; 458: 509–516. doi:10.1016/j.jallcom.2007.04.035
- [52] Binnemans K., Van Deun R., Gorller-Walrand C., Adam J.L. Optical properties of Nd³⁺-doped fluorophosphate glasses. *J. Alloys and Compounds*. 1998; 275–277: 455–460. doi:10.1016/S0925-8388(98)00367-3
- [53] Tian C., Chen X., Shuibao Y. Concentration dependence of spectroscopic properties and energy transfer analysis in Nd³⁺ doped bismuth silicate glasses. *Solid State Sci.* 2015; 48: 171–176. doi:10.1016/j.solidstatesciences.2015.08.008
- [54] Seshadri M., Barbosa L.C., Cordeiro C.M.B., Radha M., Sigoli F.A., Ratnakaram Y.C. Study of optical absorption, visible emission and NIR-Vis luminescence spectra of Tm³⁺/Yb³⁺, Ho³⁺/Yb³⁺ and Tm³⁺/Ho³⁺/Yb³⁺ doped tellurite glasses. *J. Lumin.* 2015; 166: 8–16. doi:10.1016/j.jlumin.2015.04.022
- [55] Balakrishnaiah R., Babu P., Jayasankar C.K., Joshi A.S., Speghini A., Bettinelli M. Optical and luminescence properties of Nd³⁺ ions in K-Ba-Al phosphate and fluorophosphate glasses. *J. Phys.: Condens. Matter*. 2006; 18: 165–179. doi:10.1088/0953-8984/18/1/012
- [56] Surendra babu S., Babu P., Jayasankar C.K., Joshi A.S., Speghini A., Bettinelli M. Luminescence and optical absorption properties of Nd³⁺ ions in K-Mg-Al phosphate and fluorophosphate glasses. *J. Phys.: Condens. Matter*. 2006; 18: 3975–3991. doi:10.1088/0953-8984/18/16/007
- [57] Ajroud M., Haouari M., Ben Ouada H., Maaref H., Brenier A., Garapon C. Investigation of the spectroscopic properties of Nd³⁺-doped phosphate glasses. *J. Phys.: Condens. Matter*. 2000; 12: 3181–3193. doi:10.1088/0953-8984/12/13/324
- [58] Choi J.H., Margaryan A., Margaryan A., Shi F.G. Judd-Ofelt analysis of spectroscopic properties of Nd³⁺-doped novel fluorophosphate glass. *J. Lumin.* 2005; 114: 167–177. doi:10.1016/j.jlumin.2004.12.015
- [59] Advanced Optics, SCHOTT North America Inc., Duryea, PA, USA.

- [60] HOYA Corporation USA, Optics Division, 3285 Scott Blvd., Santa Clara, CA 95054 USA.
- [61] KIGRE, Inc., 100 Marshland Road, Hilton Head, SC 29926, USA.
- [62] Iizuka K. Lab instruction notes for "Erbium Doped Fiber Amplifiers". University of Toronto; Canada: 1998.
- [63] Wang J.S., Vogel E.M., Snitzer E. Terullite glass: a new candidate for fiber devices. *Opt. Mater.* 1994; 3(3): 187–203. doi:10.1016/0925-3467(94)90004-3
- [64] Mori A., Ohishi Y., Sudoi S. Erbium-doped tellurite-based fiber laser and amplifier. *Electron. Lett.* 1997; 33(10); 863–865.
- [65] Sugimoto N., Ochiai K., Ohara S., Hayashi H., Fukasawa Y., Hirose T., Reyes M. Highly efficient and short length Lanthanum codoped B₂O₃-based EDF for extended L-band amplification. In: *Proceedings of Optical Amplifiers and their applications. 2002, OAA'02, PD 5, Vancouver, 2002.*
- [66] Weber W.H., Lambe J. Luminescent greenhouse collector for solar radiation. *Appl. Opt.* 1976; 15(10): 2299–2300. doi:10.1364/AO.15.002299
- [67] Barnham K., Marques J.L., Hassard J., O'Brien P. Quantum-dot concentrator and thermodynamic model for the global redshift. *Appl. Phys. Lett.* 2000; 76(9): 1197–1199. doi:10.1063/1.125981
- [68] Werts M.H.V., Hofstraat J.W., Geurts F.A.J., Verhoeven J.W. Fluorescein and eosin as sensitizing chromophores in near-infrared luminescent ytterbium(III), neodymium(III) and erbium(III) chelates. *Chem. Phys. Lett.* 1997; 276(3/4): 196–201. doi:10.1016/S0009-2614(97)00800-2
- [69] Sholin V., Olson J.D., Carter S.A. Semiconducting polymers and quantum dots in luminescent solar concentrators for solar energy harvesting. *J. Appl. Phys.* 2007; 101: 1231141–1231149. doi:10.1063/1.2748350
- [70] Brenda C.R., Wilson L.R., Richards B.S. Advanced material concepts for luminescent solar concentrators. *IEEE J. Selected Topics in Quant. Electron.* 14(5): 2008; 1321–1322.
- [71] Goetzberger A., Greubel W. Solar energy conversion with fluorescent collectors. *Appl. Phys.* 1977; 14: 123–139. doi:10.1007/BF00883080
- [72] Reisfeld R. Future technological applications of rare earth doped materials. *J. Less Common Mater.* 1983; 93: 243–251. doi:10.1016/0022-5088(83)90163-7

We are IntechOpen, the world's leading publisher of Open Access books Built by scientists, for scientists

6,300

Open access books available

171,000

International authors and editors

190M

Downloads

Our authors are among the

154

Countries delivered to

TOP 1%

most cited scientists

12.2%

Contributors from top 500 universities



WEB OF SCIENCE™

Selection of our books indexed in the Book Citation Index
in Web of Science™ Core Collection (BKCI)

Interested in publishing with us?
Contact book.department@intechopen.com

Numbers displayed above are based on latest data collected.
For more information visit www.intechopen.com



Luminescent Devices Based on Silicon-Rich Dielectric Materials

Santiago A. Cabañas-Tay, Liliana Palacios-Huerta,
Mariano Aceves-Mijares, Antonio Coyopol,
Sergio A. Pérez-García, Liliana Licea-Jiménez,
Carlos Domínguez and Alfredo Morales-Sánchez

Additional information is available at the end of the chapter

<http://dx.doi.org/10.5772/64894>

Abstract

Luminescent silicon-rich dielectric materials have been under intensive research due to their potential applications in optoelectronic devices. Silicon-rich nitride (SRN) and silicon-rich oxide (SRO) films have been mostly studied because of their high luminescence and compatibility with the silicon-based technology. In this chapter, the luminescent characteristics of SRN and SRO films deposited by low-pressure chemical vapor deposition are reviewed and discussed. SRN and SRO films, which exhibit the strongest photoluminescence (PL), were chosen to analyze their electrical and electroluminescent (EL) properties, including SRN/SRO bilayers. Light emitting capacitors (LECs) were fabricated with the SRN, SRO, and SRN/SRO films as the dielectric layer. SRN-LECs emit broad EL spectra where the maximum emission peak blueshifts when the polarity is changed. On the other hand, SRO-LECs with low silicon content (~39 at.%) exhibit a resistive switching (RS) behavior from a high conduction state to a low conduction state, which produce a long spectrum blueshift (~227 nm) between the EL and PL emission. When the silicon content increases, red emission is observed at both EL and PL spectra. The RS behavior is also observed in all SRN/SRO-LECs enhancing an intense ultraviolet EL. The carrier transport in all LECs is analyzed to understand their EL mechanism.

Keywords: silicon-rich dielectrics, photoluminescence, electroluminescence, conduction mechanisms

1. Introduction

The use of photonic signals instead of electrons to transmit information through an electronic circuit is an actual challenge. Unfortunately, it is well known that bulk silicon (Si) is an indirect bandgap semiconductor, making it an inefficient light emitter. Therefore, great efforts have been taken to obtain highly luminescent Si-based materials in order to get Si-based photonic devices, especially a light emitting device [1–3]. Such circumstances have led to explore new options for converting silicon into a luminescent material. Si nanoparticles (Si-nps) embedded in a dielectric material as silicon-rich oxide (SRO) or silicon-rich nitride (SRN) show a prominent photoluminescence (PL) emission in red and blue-green region, respectively [4–10]. Thus, SRN or SRO films have been considered as promising candidates for emissive materials due to their potential applications in Si-based optoelectronic devices, and their fully compatibility with the complementary metal-oxide-semiconductor (CMOS) processes [11–16].

Two main strategies have been explored: those that focus on the intrinsic emission from the matrix, either through emissions from defects or by the presence of Si-nps. The second one focus on extrinsic emission, which is produced by doping the material (usually introducing rare earth ions) [3, 17].

The most common strategy to obtain intrinsic emission is through silicon nanostructures, which significantly increase the emission due to the quantum confinement effect (QCE) [5, 18]. Furthermore, the dependence on the size of the Si-nps on the forbidden gap width allows that the emission can be adjusted in the visible and the red-near infrared region of the electromagnetic spectrum [19]. Several studies have reported both red and near infrared electroluminescence (EL) SRO which is mainly attributed to the recombination of excitons in Si-nps [20, 21]. On the other hand, the emission of green or blue light has been attributed to defects associated with oxygen [22, 23]. Some studies have reported that red (620 nm) EL emission could be attributed to non-bridging oxygen hole center (NBOHC) defects whose origin has been corroborated by the fact that the peak position does not change if the film is excited with different energies [24].

Another alternative to obtain intrinsic light emission is through an ordered structure of Si-nps by a superlattice, which is formed by the alternating of SRO and SiO₂ nano-films. Red or near infrared emission has been observed in these structures and has been related to both excitonic recombination taking place in confined states within Si-nps or relaxation of hot electrons [25, 26].

Intrinsic emission has been also observed in SRN films [27–31]. For example, an orange emission at 600 nm was observed at room temperature and has been related to the electron-hole pairs' recombination within Si-nps [27]. Also, green emission has been observed in nitrogen-rich silicon nitride, which was attributed to radiative recombination in localized states related to Si-O [28]. Some other authors have shown significant improvement of the green emission intensity using oxidized silicon-rich nitride [29]. Also, when a silicon nitride film is implanted with Si ions, violet and green-yellow emission bands are observed, giving rise to an intense

white EL emission [30]. The violet band was related with the presence of defects states related to silicon dangling bonds ($=\text{Si}^0$ or centers K^0) located near the middle of the forbidden gap of silicon nitride and defect states related to the unit $\text{Si}-\text{Si}=\text{}$ located near the edge of the valence band, while the green-yellow band was attributed to the transition from the $=\text{Si}^0$ state to nitrogen dangling bonds ($=\text{N}-$) in the tails of valence bands.

Red-near infrared EL (800 nm) has been reported in superlattices combining SRN and SiO_2 films and explained by the bipolar recombination of electron-hole pairs in Si-nps present within the SRN films [31]. A yellow EL emission has been reported when an SRO film instead of SiO_2 layer is used in the multilayer structure [32]. All of these promising results have proved the first implemented all-silicon-based photonic device [33]. Nevertheless, despite all these promising results in luminescent silicon-based materials, the improvement of the efficiency of the light emitting devices is still necessary.

This chapter shows a review about our experience on the PL and EL properties of SRN and SRO films deposited by low-pressure chemical vapor deposition (LPCVD). The effect of the combination of the SRN and SRO luminescent properties is also analyzed as an SRN/SRO structure. A study about the composition, structural, optical, and electro-optical properties of these films will be discussed. The study also includes the analysis of the charge transport mechanism through the SRO, SRN, and SRN/SRO films to understand their electroluminescence behavior and its correlation with the different luminescent centers (LCs) within the active material.

2. Experimental procedure

In this chapter, SRN, SRO, and SRN/SRO films were deposited in a homemade LPCVD hot-wall reactor. In these silicon-rich dielectrics materials, the Si content was controlled by a ratio of partial pressure of reactant gases; R_N and R_o for SRN and SRO, respectively.

The SRN films were deposited on N-type ((100)-oriented) Si wafers with a resistivity of 1–5 $\Omega\text{-cm}$ at 750°C using ammonia (NH_3) and 5% nitrogen (N_2)-diluted silane (SiH_4) as the reactant gases by the ratio $R_N = 20 \cdot P(\text{NH}_3)/P(\text{SiH}_4)$. SRN films with R_N values of 5, 20, and 80 were deposited with the parameters shown in **Table 1**. SRO films were deposited on N-type Si wafers with a resistivity of 5–10 $\Omega\text{-cm}$ ((100)-oriented) at a temperature of 720°C using pure nitrous oxide (N_2O) and 3.3% nitrogen (N_2)-diluted silane (SiH_4) as the reactant gases by the ratio $R_o = 30 \cdot P(\text{N}_2\text{O})/P(\text{SiH}_4)$. SRO films with R_o values of 30 and 20 were deposited with the parameters shown in **Table 1**. Finally, SRN/SRO bilayers were deposited on P-type silicon substrates ((100)-oriented) with resistivity of 5–10 $\Omega\text{-cm}$. $R_o = 20$ and 30 and $R_N = 80$ values were used for the SRO and SRN films, respectively. SRO and SRN films were deposited at 730 and 760°C, respectively. The deposition conditions are also summarized in **Table 1**. About 3.3% of nitrogen diluted silane was used for the bilayer structures.

After deposition, SRN, SRO and SRN/SRO samples were thermally annealed at 1100°C under nitrogen atmosphere conditions for 180 min.

	Sample name	R_N	R_o	Pressure of gases (Torr)			Time (min)	Thickness (nm)
				N_2O	NH_3	SiH_4		
SRO	M20		20	0.53		0.80	12	55.72 ± 5.0
	M30		30	0.80		0.80	15	64.00 ± 3.4
SRN	N5	5			0.22	0.85	10	102.83 ± 3.62
	N20	20			0.85	0.85	15	112.67 ± 6.19
	N80	80			2.00	0.50	13	66.93 ± 2.12
SRN/SRO	B20	80			1.08	0.41	4	16.32 ± 1.54
			20	0.53		0.80	15	55.72 ± 5.0
	B30	80			1.08	0.41	4	16.32 ± 1.54
			30	0.80		0.80	15	64.00 ± 3.4

Table 1. Process parameters of the SRO, SRN and SRN/SRO films deposited by LPCVD and thickness of the sample after thermal annealing.

For electrical and electroluminescence studies, light emitting capacitive (LEC) structures were fabricated. For SRN-LECs, a transparent 300-nm thick fluorine-doped tin oxide $SnO_2:F$ (FTO) film was deposited onto the surface of the SRN by ultrasonic spray pyrolysis. Square-shaped patterns with 1 mm^2 area were defined by a photolithography process step to act as gate contact. For SRO-LECs, ~400-nm thick semitransparent n^+ polycrystalline silicon (poly) gate was deposited onto the SRO film surface by LPCVD. After a photolithography process step, square-shaped gates of 4 mm^2 area were defined. For SRN/SRO-LECs, ~300-nm thick indium tin oxide (ITO) film was deposited by RF sputtering onto the surface of the films as gate contact. Square-shaped patterns with area of 1 mm^2 were defined by a photolithography process step to act as anode gate contact. Approximately 700-nm thick aluminum (Al) film was evaporated onto the backside of the silicon substrates as cathode contact in all of the LECs. A thermal annealing process at 460°C in N_2 atmosphere for 20 min was used to form the ohmic contact.

The thickness of thermally annealed SRO and SRN films was measured with a Gaertner L117 ellipsometer with a 70° incident laser with wavelength of 632.8 nm and is also shown in **Table 1**. Chemical bonding characteristics was analyzed by means of Fourier transform infra-red spectroscopy (FTIR) with a Bruker V22 equipment in the $4000\text{--}350 \text{ cm}^{-1}$ range with a resolution of 5 cm^{-1} . The PL spectra were measured with a Fluoromax 3 of Horiba Jobin Yvon. The samples were excited using a 300 nm radiation, and the PL emission signal was collected from 400 to 900 nm with a resolution of 1 nm. The depth analysis profile of thermally annealed SRN, SRO, and SRN/SRO films was analyzed by means of X-ray photoelectron spectroscopy (XPS) Escalab 250Xi of Thermo Scientific equipment, with an Al $K\alpha$ monochromated source. Current-voltage (I-V) measurements of SRN, SRO, and SRN/SRO-LECs were

performed using a Keithley 4200-SCS parameter analyzer at the same time that the EL was collected with an optical fiber, which was located right on the surface of the device and connected to an Ocean Optics QE-65000 spectrometer.

3. Composition

The composition of SRN and SRO films play an important role in order to understand their luminescence, electrical, and electro-optical properties. In this sense, some techniques such as FTIR and XPS spectroscopies have been used.

3.1. Silicon-rich nitride (SRN) film

The Si-N bonds of SRN films were determined by FTIR measurements. **Figure 1(a)** shows the IR spectra measured from SRN films with $R_N = 5$ (N5), 20 (N20), and 80 (N80) before (B-TA) and after (A-TA) thermal annealing.

IR peaks at 460 and 840 cm^{-1} ascribed to Si-N wagging and stretching modes, respectively, were observed for all samples [35–37]. An IR band appears at 1080 cm^{-1} after thermal annealing, being more evident in the N80 sample. The presence of this peak has been observed before and attributed to a reordering in the films toward $\alpha\text{-Si}_3\text{N}_4$ bonding configuration [38, 39]. Nevertheless, it could be related to the Si-O stretching mode due the oxygen incorporation in the samples.

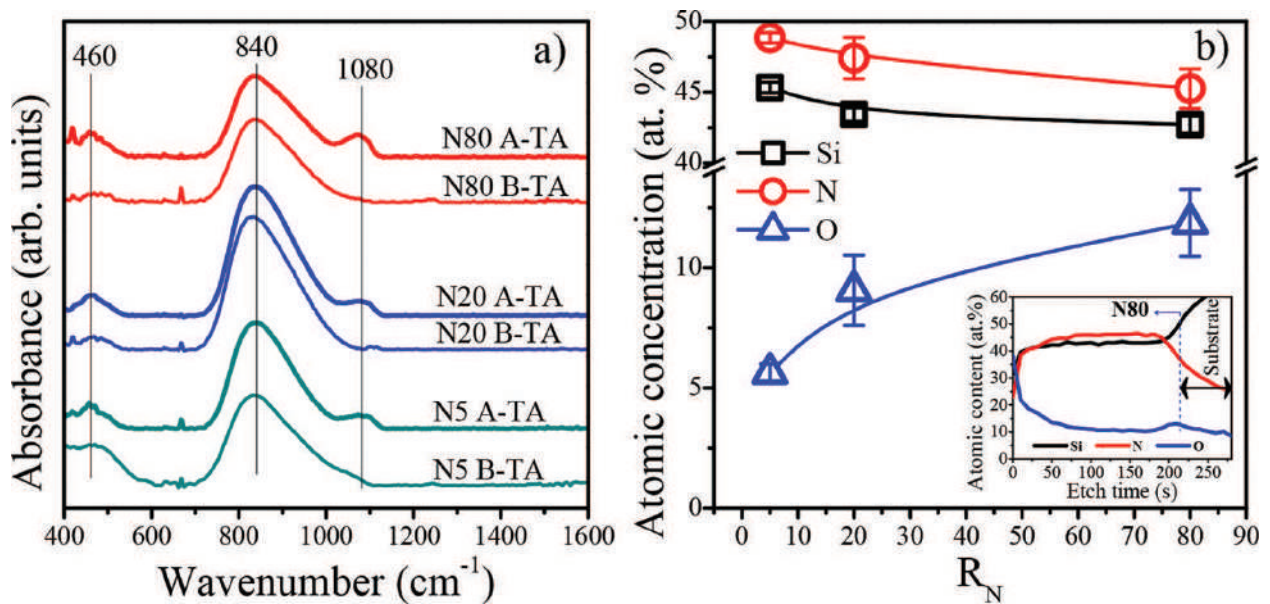


Figure 1. (a) FTIR spectra of SRN films with $R_N = 5$ (N5), 20 (N20) and 80 (N80) before and after thermal annealing, and (b) atomic concentration (at.%) of Si, O, and N as a function of R_N . Inset shows the XPS depth profile of SRN film with $R_N = 80$ (N80). From Cabañas-Tay et al. [34].

In order to comprehend the stoichiometry and the presence of some oxygen into the SRN films, analysis of their composition was performed by means of XPS. **Figure 1(b)** shows information about the chemical composition of the thermally annealed SRN samples. The inset of **Figure 1(b)** exhibits the depth profile composition of the thermally annealed $R_N = 80$ (N80) sample. As can be observed, some oxygen is present at the outmost part of the layer through the film depth, being present mainly at the film surface. This behavior is similar for different R_N but with different concentrations. **Figure 1(b)** shows the atomic concentration of Si, O, and N as a function of R_N . Mean silicon content values along the layer of 45.55 ± 0.38 , 43.58 ± 0.48 , and 42.88 ± 1.39 at.% were obtained for the SRN films with $R_N = 5$, 20, and 80, respectively. Moreover, the presence of oxygen increases from 5.6 to 11.8 at.% as the R_N value increases from 5 to 80, respectively.

3.2. Silicon-rich oxide (SRO) film

The Si–O bonds of SRO films were also determined by FTIR measurements. The IR spectra measured from SRO films with $R_o = 20$ (M20) and $R_o = 30$ (M30) after thermal annealing are shown in **Figure 2(a)**. Typical vibration bands at 460, 810, and 1070 cm^{-1} related to Si–O rocking, Si–O bending, and Si–O stretching modes, respectively, were present in both SRO films [40, 41]. The shoulder from ~ 1100 to $\sim 1300 \text{ cm}^{-1}$ observed in both SRO films has been attributed to Si–O stretching out of phase [42]. It has been reported that this shoulder is less pronounced for the suboxides compared to the stoichiometric oxide [43, 44]. The absorption at 610 cm^{-1} due to unsaturated Si–Si bonds (phonon-phonon interactions) was observed only in M20 (SRO film with higher proportion of silicon precursor) showing the presence of structural imperfections at the SiO_2 /silicon nanoparticles (Si-nps) interface [45].

Figure 2(b) exhibits the depth profile composition of the thermally annealed SRO films. Mean silicon content values of 41.85 ± 1.1 and 39.98 ± 0.8 at.% were obtained for the SRO films with

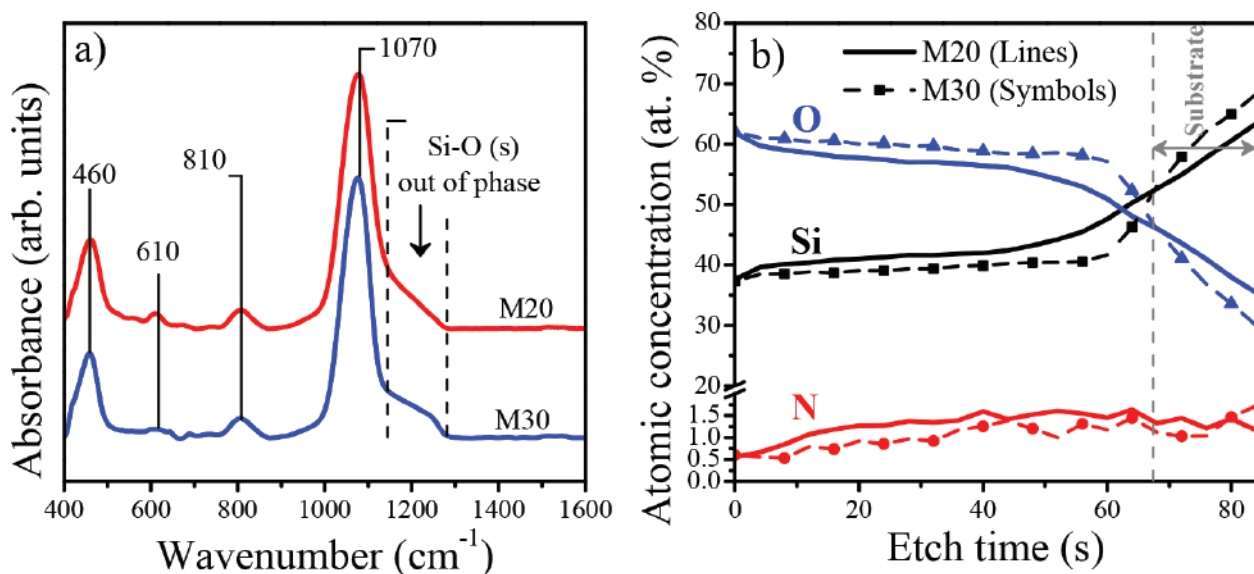


Figure 2. (a) FTIR spectra of SRO films with $R_o = 20$ (M20) and 30 (M30) after thermal annealing, and (b) XPS depth profile of SRO films with $R_o = 20$ (M20) and 30 (M30).

$R_o = 20$ (M20) and 30 (M30), respectively. The presence of nitrogen was also observed in both SRO films being slightly more evident for M20. An analysis of the Si2p XPS signal of SRO film with $R_o = 30$ thermally annealed at 1100°C (not showed here) [46] shows that the microstructure of this film is almost a stoichiometric SiO₂ (Si⁴⁺) and that the silicon excess is present as Si–O compounds, which could include the neutral oxygen vacancy (NOV) and non-bridging oxygen hole center (NBOHC) defects. As expected by the Si2p XPS signal, crystalline silicon nanoparticles were not observed in this films; however, energy-filtered transmission electron microscopy (EFTEM) analysis has shown (although not clearly) the presence of silicon nanoparticles with a mean size of 1.5 nm and density of $\sim 1.1 \times 10^{12} \text{ cm}^{-2}$ as reported in [47, 48]. In fact, it has been reported that a largely disordered system is expected when the size of Si-nps is between 1 and 2 nm. Thus, the small Si-nps are no longer crystalline but amorphous like, as also indicated by theoretical calculations [49, 50]. Then, the dispersed Si atoms in the M30 films are preferentially arranged as very small Si-nps (E_v) and some defects like oxygen-deficiency center (ODC) and NBOHC as reported for thin SiO_x films (<100 nm) [51].

The presence of the Si⁰ peak in the Si2p XPS signal correlates well with the presence of silicon nanocrystal observed by high-resolution transmission electron microscopy (HRTEM, not shown here) in the M20 film. HRTEM reveals Si nanocrystals with an average size (and density) of $2.91 \pm 0.40 \text{ nm}$ ($8.66 \times 10^{11} \text{ cm}^{-2}$) [46].

3.3. Silicon-rich nitride/silicon-rich oxide (SRN/SRO) bilayer

The Si–N and Si–O bonds of SRN/SRO bilayers with $R_o = 20$ (B20) and $R_o = 30$ (B30) were also determined. **Figure 3(a)** shows the FTIR spectra of SRO and SRN/SRO films with $R_o = 20$ (M20 and B20, respectively) after thermal annealing. The IR peak at 820 cm⁻¹ observed only in the B20 bilayer is ascribed to Si–N stretching present in SRN films [45]. The intensity of a shoulder

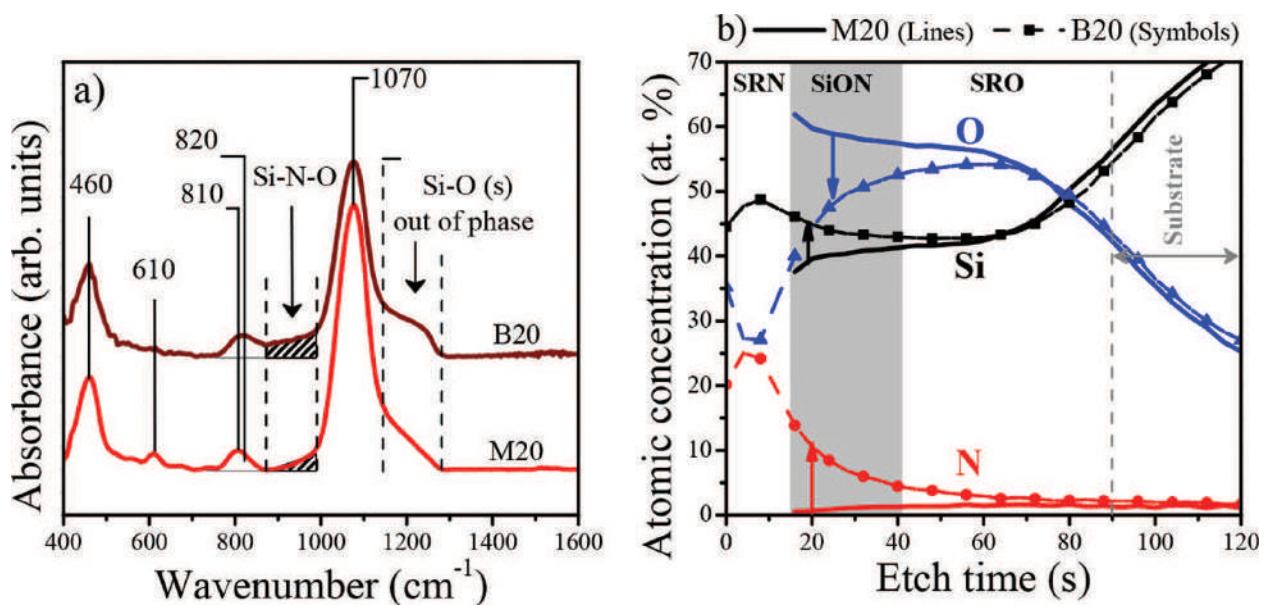


Figure 3. (a) FTIR spectra of SRO and SRN/SRO films with $R_o = 20$ (M20 and B20, respectively) after thermal annealing, and (b) XPS depth profile of SRO and SRN/SRO films with $R_o = 20$ (M20 and B30, respectively) after thermal annealing.

(shadow area) from 900 to 1000 cm^{-1} increased when the B20 bilayer was formed, and it was attributed to the formation of Si–N–O bonds in silicon oxynitride [45].

As shown in **Figure 3(a)**, the shoulder from ~ 1100 to ~ 1300 cm^{-1} was observed in both samples (M20 and B20) and it was attributed to Si–O stretching out of phase [42]. The IR peak at 610 cm^{-1} observed in the SRO monolayer (M20) disappeared for the bilayer (B20) and it could be related to the nitrogen incorporation within the SRO that creates Si–N–O–Si bridges. The presence of these bridges decreased the quantity of strained bonds and Si dangling bonds at the $\text{SiO}_2/\text{Si-np}$ interface [45]. The SRN/SRO film with $R_o = 30$ (B30) showed the same IR peaks than the B20 bilayer, except for the 610 cm^{-1} IR peak.

Figure 3(b) showed the depth profile composition of the thermally annealed SRO monolayer and SRN/SRO bilayer, both with $R_o = 20$ (M20 and B20, respectively). The average Si content within the SRO monolayer was about 41.85 ± 1.1 at.%. When the SRN/SRO bilayer was formed, the oxide-nitride interface became an imprecise oxynitride (SiON) layer almost for 30 s etching time (shadow area in **Figure 3(b)**). In that region, a gradual increasing of both nitrogen and silicon was observed toward the interface. The average Si content slightly increased up to $\sim 43.21 \pm 0.7$ at.% in the SRO layer, whereas the oxygen content in the SRO film was reduced from 56.78 ± 1.3 to 53.08 ± 1.0 at.%. The Si, O, and N diffusion could be enhanced by the high annealing temperature. This is supported by two facts: first, the presence of a nitrogen concentration within the oxide layer which goes from 2 to 10%, and second, the oxygen presence in the nitride layer ($\sim 25\%$). The nitrogen content inside of the SRO in the SRN/SRO bilayer structure could modify its optical and structural properties. It has been reported that the nitrogen hinder the diffusion of Si atoms and prevents the phase separation in the amorphous $\text{SiO}_x\text{:N}$ films [52]. Thus, the mobility of the Si atoms is smaller and the growth of the Si-nps during the thermal diffusion process is reduced, giving as a result smaller Si-nps. A similar behavior was observed for the B30 bilayer, but with different concentration.

4. Photoluminescence

4.1. Silicon-rich nitride (SRN) film

The PL spectra of SRN films before and after thermal annealing are shown in **Figure 4**. The PL intensity was normalized to the thickness of each SRN film. The as-deposited SRN film with $R_N = 80$ (N80) emit a broad PL band with the main peak at 490 nm, as shown in **Figure 4(a)**. As the R_N value decreases, the PL emission band becomes narrower and shifts to a higher wavelength reaching 590 nm for $R_N = 5$ (N5, higher silicon excess) but with a lower intensity.

The PL band of the SRN films blueshifts after thermal annealing, particularly for $R_N = 80$ where the main band shifts from 490 to 420 nm, as shown in **Figure 4(b)**. It is well known that the silicon excess in silicon-rich dielectrics agglomerates forming Si-nps after high temperature annealing, resulting in a redshift of the PL band due to the quantum confinement effects [53–57]. However, contrary to this assumption, in this work, the PL blueshifts after the annealing, as shown in **Figure 4(b)**. This effect has been observed before and it has been ascribed to compositional-dependent changes in the concentration of defect states within the samples [58].

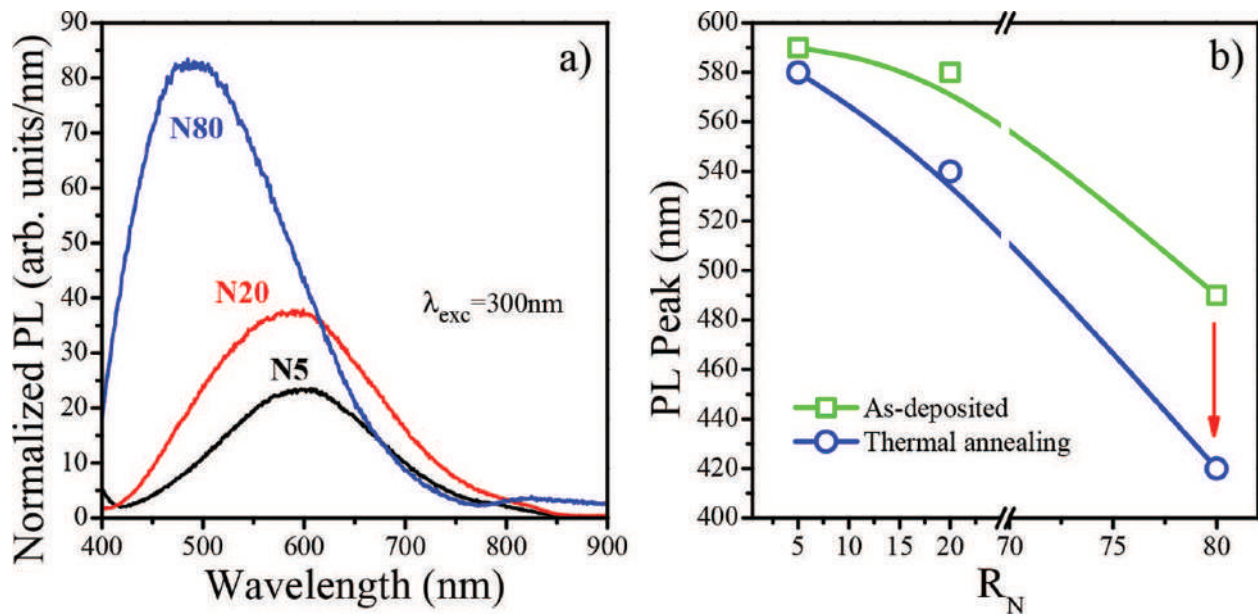


Figure 4. (a) Normalized PL spectra of as-deposited, and (b) maximum PL peak position before and after thermally annealed, SRN films with $R_N=5$ (N5), 20 (N20), and 80 (N80). Lines are plotted as an eye-guide. From Cabañas-Tay et al. [34].

Therefore, defects are created rather than Si-nps, after thermal annealing. Moreover, due to the low diffusivity of silicon atoms in Si_3N_4 , a high Si content (>52 at.%) is needed to form Si-nps [59, 60]. Because of the low Si content present in the SRN films from this work (<46 at.%), as shown above in the XPS results, these films can be explained as a sub-stoichiometric nitride with structural defects, as reported in the study of Cabañas-Tay et al. [34].

PL bands between 380 and 600 nm (2.0–3.2 eV) have been observed before in SRN films, and they have been ascribed to the radiative recombination of carriers in band tail states, which are related to defect energy levels within the gap of amorphous silicon nitride [61–64]. Therefore, the PL bands emitted by the SRN films from this work can be explained by the excitation of different defects as discussed in the study of Cabañas-Tay et al. [34]. As observed in **Figure 4(a)**, the as-deposited SRN films emit at 590, 580, and 490 nm, whereas the thermally annealed films emit at 580, 540, and 420 nm for R_N of 5, 20, and 80, respectively. PL emission bands observed at 580–590 nm (~2.1 eV) have been related to electronic transitions from the conduction band minimum (CBM) to K^0 centers located near of the mid-gap, the emission band at 540 nm (~2.3 eV) is related to electronic transition from the K^0 centers to $=\text{N}^-$ centers located near of the valence band maximum (VBM), and the emission band at 420 nm (~2.9 eV) has been related to electronic transitions from the K^0 centers to VBM. Hence, the PL bands observed in this work could have a similar origin, as discussed in the study of Cabañas-Tay et al. [34].

Some studies have shown that electronic transition related with K^0 centers to $=\text{Si-O-Si}$ states are observed when oxygen is incorporated in the SRN film [65, 66]. The presence of oxygen in SRN films creates a gap state of Si-O above the VBM, giving rise to the 485 nm (~2.55 eV) emission. The XPS analysis demonstrated that SRN films contain oxygen, being the higher concentration for $R_N=80$ (11.8 at.%). Therefore, the PL emission band at 490 nm (~2.53 eV)

observed in the as-deposited sample with $R_N = 80$ could be related to the electronic transition from the K^0 centers to $=\text{Si}-\text{O}-\text{Si}$ states.

In summary, the analysis of the PL emission observed in the SRN films before and after thermal annealing indicates that it could be mainly originated from the radiative recombination via luminescent Si dangling bonds, N dangling bonds, and Si-O bonds existing in the silicon nitride matrix.

4.2. Silicon-rich oxide (SRO) film

Figure 5 shows the normalized PL spectra of SRO films before and after thermal annealing. The as-deposited SRO film with $R_o = 30$ (M30) emits a broad PL band with the main peak at 460 nm. After thermal annealing, the PL emission band becomes narrower and redshifts reaching 690 nm, as shown in **Figure 5(a)**. As the R_o value decreases, the PL emission band becomes wider and shifts to a higher wavelength reaching 660 nm for $R_o = 20$ (M20, higher silicon excess), as shown in **Figure 5(b)**. After thermal annealing, the PL of M20 redshifts, reaching 740 nm.

The PL emitted by M30 exhibit a significant redshift of the main peak after thermal annealing as shown in **Figure 5(a)**. Nevertheless, when the silicon content is increased (M20), the PL band appears mainly at the red side of the spectrum. The redshift of the main PL peak (after thermal annealing) has been widely observed and ascribed to the agglomeration of silicon excess and a subsequent silicon nanoparticle formation as a result of thermal annealing process [67–71]. Nevertheless, some point defects are also present within the SRO films. It is widely accepted that violet-blue (400–460 nm), green (520), and even red (630) emission bands, obtained from the deconvolution of the PL spectrum [72], can be related with oxygen

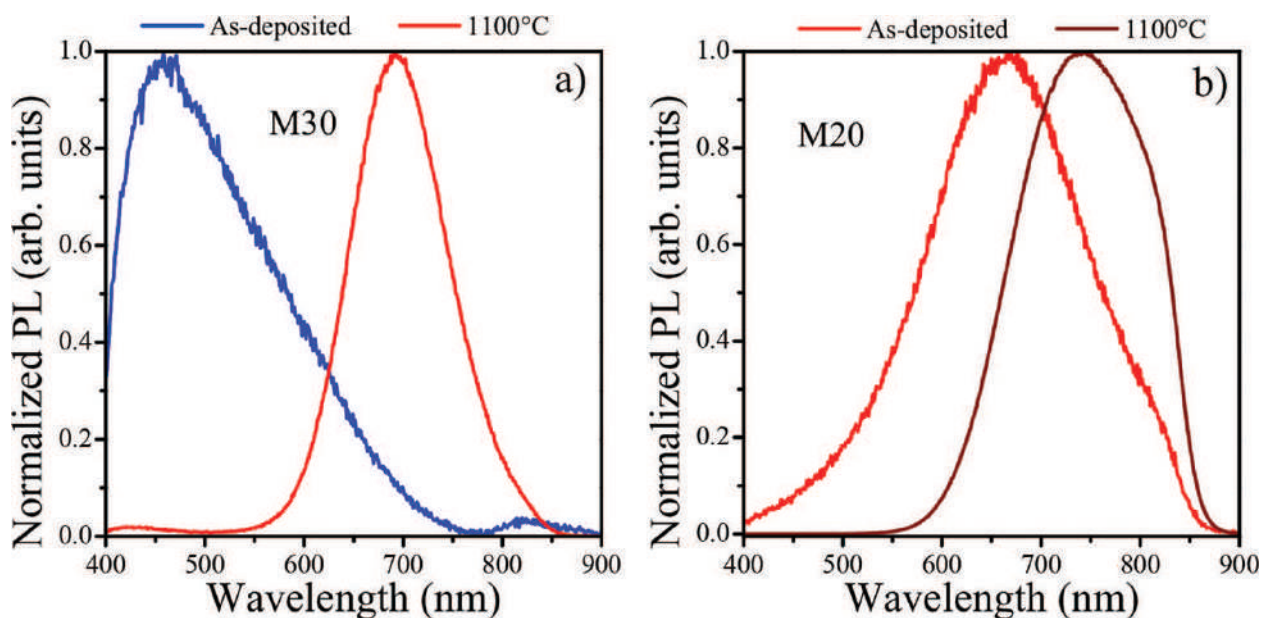


Figure 5. Normalized PL spectra of SRO monolayer (a) with $R_o = 30$ (M30) and (b) $R_o = 20$ (M20) before and after thermal annealing. From Palacios-Huerta et al. [46].

defect centers (ODC), E'_δ (Si \uparrow Si=Si) and NBOHC defects, respectively [67–71]. The E'_δ center is one of the at least four different E' centers [43], which comprises an unpaired spin delocalized over five silicon atoms and suggest the presence of very small Si-nps in the films.

4.3. Silicon-rich nitride/silicon-rich oxide (SRN/SRO) bilayers

In previous studies, it has been reported that the combination of Si₃N₄/SRO structure improves luminescent emission properties [73, 74]. Previous studies have also shown that a Si₃N₄-SRO bilayer structure improves the operation of light-emitting devices, such as a reduced leakage current, a reduced electric field on the oxide layer, and results an improvement in efficiency and a longer device life [73–76]. In this chapter, the effect of a SRN film on a SRO film (SRN/SRO bilayers) on their optical properties is analyzed. SRN films, deposited by LPCVD with $R_N=80$ (N80), show luminescence in the blue region, while the SRO films emit in the red region, as observed in **Figures 4** and **5**, respectively. Therefore, a combination of SRN with $R_N=80$ and SRO films could allow reaching a broad emission spectrum.

Figure 6 shows the PL spectra of SRN/SRO bilayers with $R_o=20$ (B20) and 30 (B30) after thermal annealing. The emission spectra of the SRN (N80) and SRO monolayer films with $R_o=20$ (M20) and 30 (M30) are shown as references, respectively. The emission spectra of the samples were normalized to the SRO thickness. Each PL spectrum of SRN and SRO

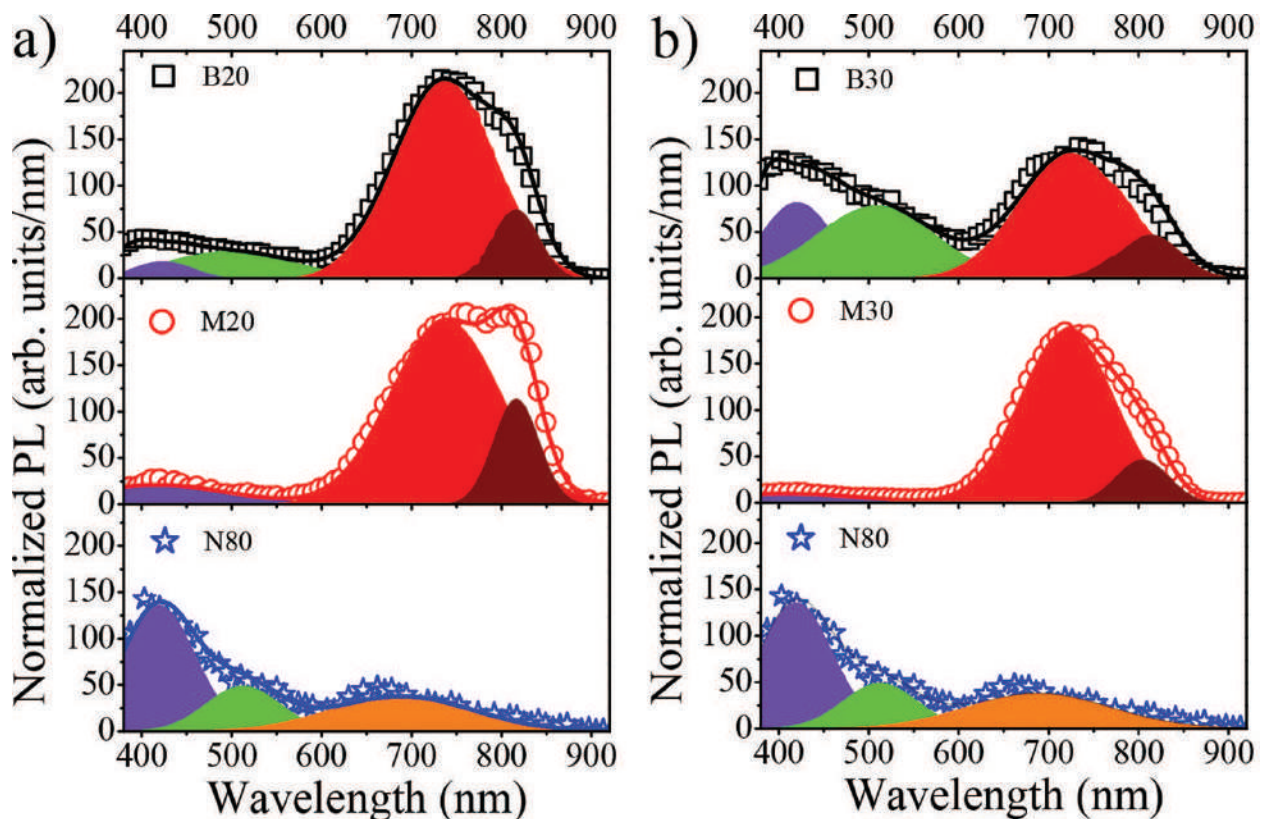


Figure 6. Normalized PL spectra after thermal annealing of (a) SRN/SRO film with $R_o=20$ (B20), SRN film with $R_N=80$ (N80), and SRO with $R_o=20$ (M20), and (b) SRN/SRO film with $R_o=30$ (B30), SRN film with $R_N=80$ (N80), and SRO with $R_o=30$ (M30).

monolayers was fitted three Gaussian, while four Gaussians were used to fit the PL spectrum of the SRO/SRN bilayer.

For the SRN film (N80), PL bands at about ~420, 505, and 680 nm were identified, which are related to electronic transitions from the K^0 centers to the VBM, K^0 centers to =Si–O–Si, and states of defects nitrogen (N^0_2), respectively [64]. For the SRO film with $R_o = 20$ (M20), PL bands at ~420, 735, and 820 nm were identified and have been widely related to weak oxygen bond (WOB) defects, interactions that take place at the Si-np/SiO_x interface, and quantum confinement in silicon nanocrystals, respectively [72]. The PL spectrum of the SRN/SRO bilayer with $R_o = 20$ (B20) exhibits the same PL bands of the SRO films at ~420, ~735, and 812 nm, but with an additional band at ~505 nm (green band), which is related to transitions from K^0 centers to =Si–O–Si featured of the SRN film, as shown in **Figure 6(a)**.

As observed in **Figure 6(b)**, the SRO monolayer with $R_o = 30$ (M30) exhibits PL bands at ~420, 720, and 805 nm, which have been also linked to WOB defects, interactions that take place at the Si-nps/SiO_x interface, and silicon nanocrystals (Si-ncs) through quantum confinement, respectively [72]. The PL spectrum of the SRN/SRO with $R_o = 30$ (B30) is composed by the same luminescent bands than that observed in the bilayer with $R_o = 20$ (B20), but with an increased intensity of the bands at ~420 and ~505 nm related with transitions from K^0 centers to VBM (violet band), transitions from K^0 centers to =Si–O–Si (green band), respectively.

In summary, it is observed that the emission intensity in the blue and green bands (~420 and 505 nm) is improved when a SRN/SRO bilayer is formed compared to SRO monolayers, being higher when a $R_o = 30$ (B30) is used. The XPS results show a diffusion of oxygen from the SRO layer to the SRN layer and nitrogen from the SRN layer to the SRO layer during SRN deposition (onto SRO layer). Therefore, some defects could be passivated into the SRO layer and others generated into the SRN layer like WOB or =Si–O–Si defects.

5. Electroluminescence

SRN, SRO, and SRN/SRO films exhibit intense and visible photoluminescence. In this section, luminescent characteristics of the samples are present but under electrical excitation.

5.1. Silicon-rich nitride (SRN)-LECs

Figure 7 shows the EL spectra of the light emitting capacitors using the as-deposited SRN film with $R_N = 20$ as an active dielectric layer at different injected currents. At forward bias (FB) (positive voltage to FTO contact respect to Si substrate), the SRN-LEC shows a broad spectrum with the maximum emission centered at around 580 nm, and it remains at the same wavelengths for different voltages as shown in **Figure 7(a)**. This luminescence has been reported as a characteristic behavior of defect-related EL [67]. In fact, the luminescent properties of SRN films in this chapter are related to the presence of defects. Therefore, the EL in SRN-LECs may originate from the same electronic transitions of the CBM to K^0 centers,

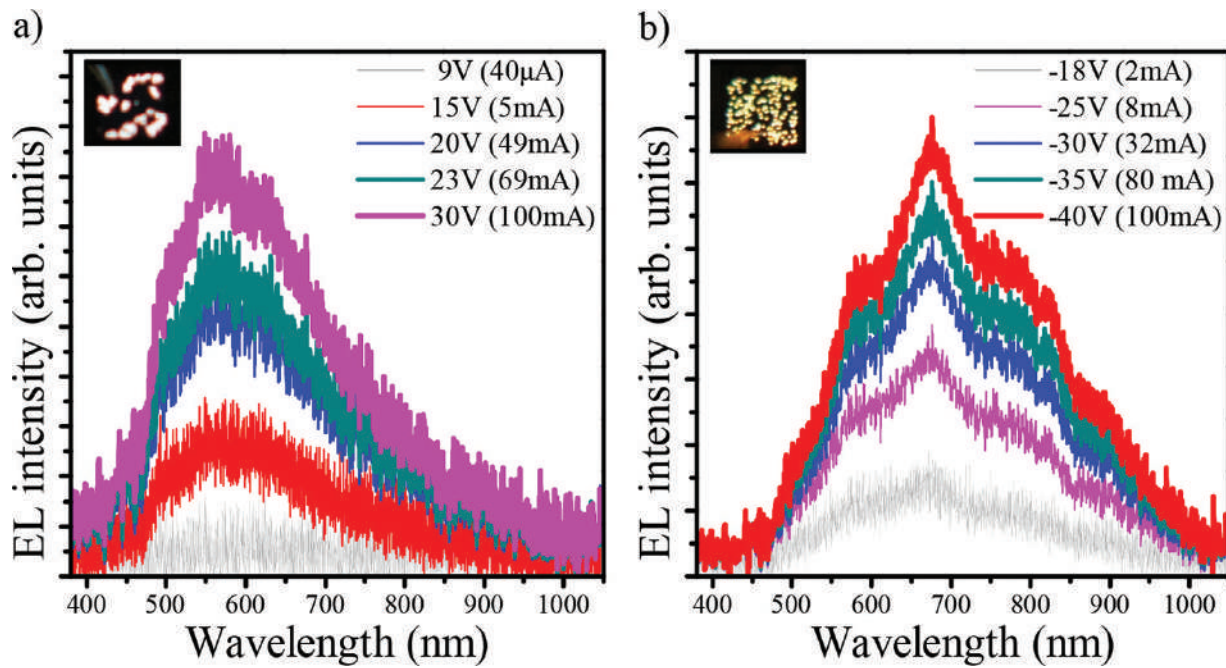


Figure 7. EL spectra of the as-deposited SRN LEC with $R_N=20$ for different injected currents at (a) forward bias and (b) reverse bias. In the inset, pictures for the device with 100 mA of injected current for each bias. FTO was used as gate electrode. From Cabañas-Tay et al. [34].

as observed in PL [77, 78]. This behavior is similar for all SRN films in both as-deposited and after thermal annealing, as reported in the study of Cabañas-Tay et al. [34].

On the other hand, at reverse bias (RB), the EL spectrum changes and now three main emission bands are observed at around 600, 680, and 780 nm, as observed in **Figure 7(b)**. Namely, the maximum emission band blueshifts when the polarity is changed from RB to FB. The EL bands at 600, 680, and 780 nm also remains at the same wavelength when the voltage is increased indicating the EL emission is also produced by defects. These EL bands have been ascribed to electronic transitions from the K^0 centers to valence band tail states [58, 77]. The EL emission for all the SRN-LECs in both polarities is through shine dots as shown in the inset of **Figure 7(a)** and **(b)**. The device's area is covered with more shine dots when the current increases. The EL emission composed by shining spots is attributed to the formation of a finite number of preferential conductive paths within the SRN films, which connect the top and bottom electrodes, as discussed in the study of Cabañas-Tay et al. [34].

Negligible spectral shift is observed between the EL at forward bias and PL spectra of SRN films with $R_N=5$ and 20 before and after thermal annealing, indicating that both PL and EL emissions are originated from the same radiative centers [34]. Nevertheless, a long spectral shift is observed for the SRN films with $R_N=80$ (before and after thermal annealing). This behavior was explained as a significant smaller electrical pumping of electrons allowing the holes to relax to the lowest defect states before recombining. For the EL at RB, a similar behavior is presented but the electrical pumping of electrons is slightly improved allowing only few of the holes to relax to the lowest defect states before recombining [34].

5.2. Silicon-rich oxide (SRO)-LECs

The presence of defects including the Si-nps, either crystalline or amorphous, and their density and size in silicon-rich dielectric materials affect clearly the current transport, and therefore the EL, as in the SRO case. **Figure 8** shows J-E curves of SRO-LECs with $R_o = 30$ and 20; samples were thermally annealed at 1100°C. SRO-LECs are forwardly biased (accumulation mode) considering the substrate as reference.

SRO-LECs with $R_o = 30$ (M30) films show a high current state (HCS) at low electric fields, then after the applied voltage increased, the current was switched to an LCS, as shown in **Figure 8**. This behavior was observed by our group before in SRO films with $R_o = 30$, and it was related to the creation and annihilation of preferential conductive paths generated possibly by adjacent stable Si-nps and unstable silicon nanoclusters (Si-ncls) through structural changes and by the possible creation of defects (breaking off Si-Si bonds) [70, 79, 80]. Indeed, a clear correlation between current jumps/drops and EL dots appearing/disappearing on the LEC surface was observed [70, 79, 80]. This RS behavior is independent on the thermal annealing temperature [46]. Recent studies regarding the same electrical RS behavior in SRO films was observed and related with a conductive filament formed by Si-nps [81–84], which undergoes structural changes through a crystallization and amorphization process of the Si-nps, as discussed in [82]. Such observations are in agreement with the presented asseverations about the behavior of the SRO with $R_o = 30$ (M30)-based LECs.

Once the current fluctuations disappear, through the electrical annealing, the current behavior stabilized (see I-V curve marked as M30-after in dark blue line, **Figure 8**) and EL on the whole area (WA EL) was observed at higher electric fields. On the other hand, the electrical behavior of SRO-LEC with $R_o = 20$ (M20) did not show current fluctuations. The latter could

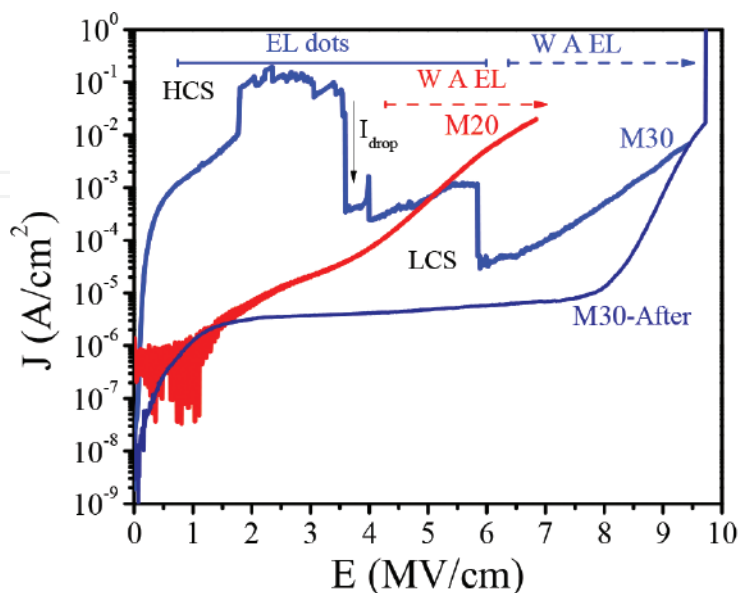


Figure 8. J-E curve of SRO-LECs with $R_o = 20$ (M20) and 30 (M30) thermally annealed at 1100°C. From Palacios-Huerta et al. [46].

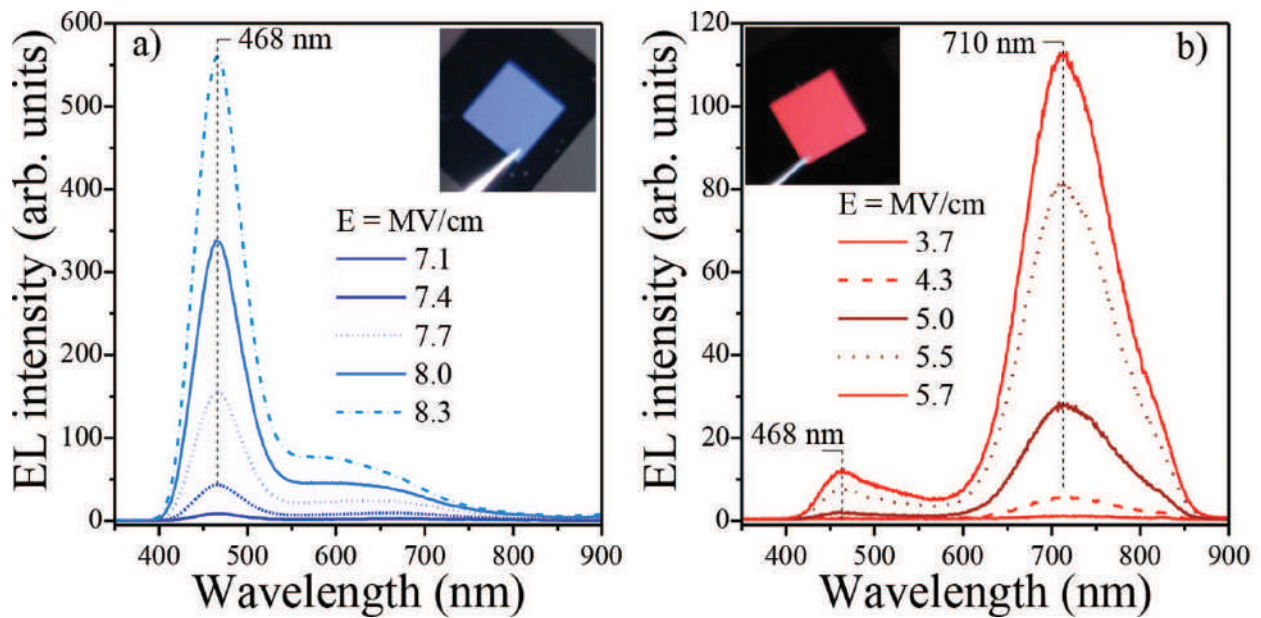


Figure 9. EL spectra and images of SRO-LECs with (a) $R_o = 20$ (M20) and (b) 30 (M30) annealed at 1100°C . Semitransparent n^+ polycrystalline silicon was used as gate electrode. From Palacios-Huerta et al. [46].

be related to the presence of well-separated and crystalline silicon nanoparticles, mainly on the density of Si-nps, as shown by transmission electron microscopy (TEM) analysis [46]. Therefore, a uniform network of conductive paths becomes possible as the Si-nps density increases, allowing a uniform charge flow through the whole capacitor area.

Figure 9 shows the EL spectra from the SRO-LECs. Blue EL in the whole area was observed with $R_o = 30$ (M30) only after the current drop. The main EL peak remains at 468 nm when the electric field increases, as observed in **Figure 9(a)**. When the silicon content is increased ($R_o = 20$), the LECs emit a broad EL spectrum in the red region, as observed in **Figure 9(b)**. The EL peak is placed at 710 nm. This value is blueshifted with respect to the value found in PL at 740 nm. Differences in the PL and EL peak wavelength have been related to the transmittance of the top electrode, which influences the real light emission from the active layer [85]. Indeed, the process of carrier injection and the several transport mechanism taking place through the active luminescent materials produces a complicated understanding of the EL process, as compared to the PL one [86]. Nevertheless, both EL and PL spectra appear in the same red region, which could indicate that the emission is originated by the same radiative centers. Images of LECs are shown as insets in **Figure 9**. As can be observed, the LEC devices emit an intense whole area EL.

5.3. Silicon-rich nitride/silicon-rich oxide (SRN/SRO)-LECs

Figure 10 shows the $J(E)$ characteristic and the EL spectra of SRN/SRO-LECs at forward bias considering the substrate like reference. SRN/SRO-LECs show a high current state (HCS) at low electric fields, and then after the applied voltage increases, the current is switched to a LCS, as shown in **Figure 10(a)**. The resistive switching in the B20 bilayer occurs at a lower electric field (~ 2 MV/cm) compared to the B30 bilayer. When SRN/SRO-LECs, both with $R_o = 20$

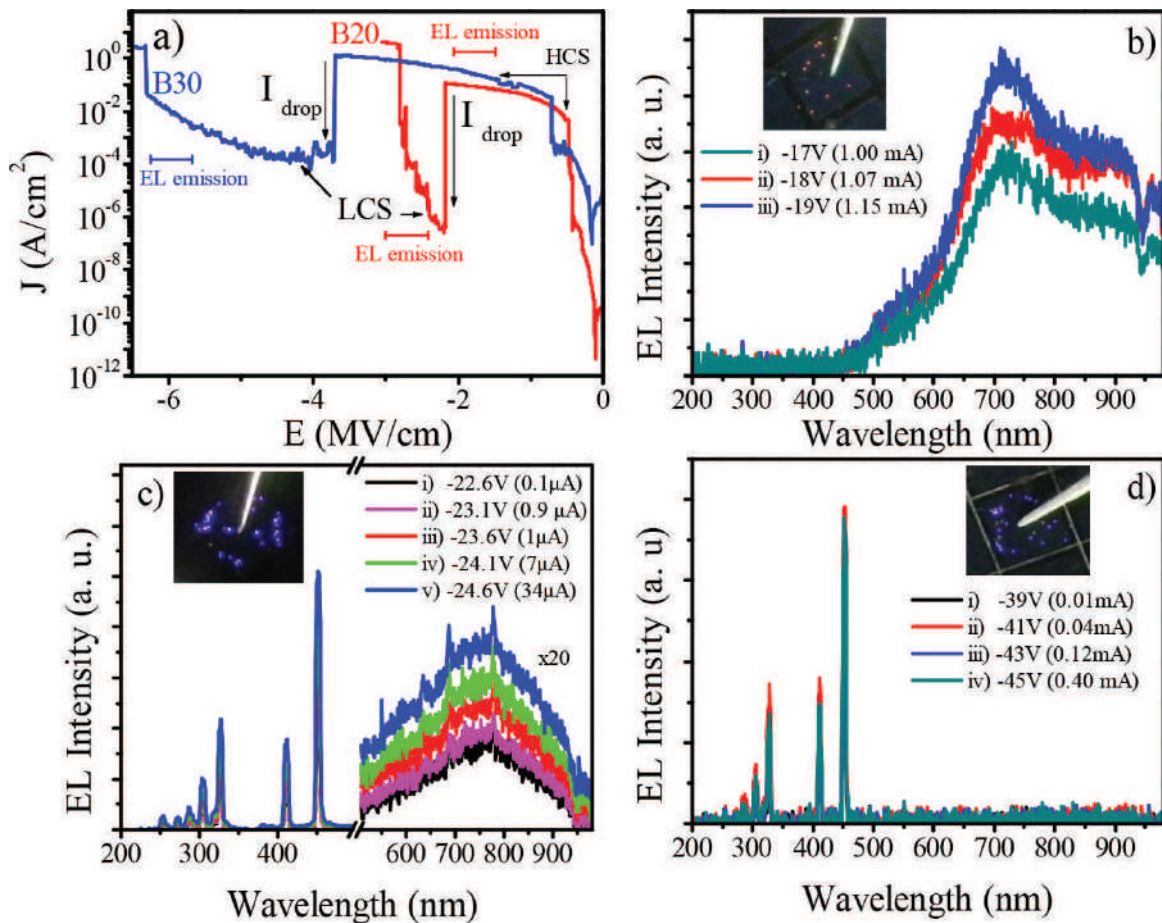


Figure 10. (a) J-E curve of SRN/SRO-LECs with $R_o = 20$ (B20) and 30 (B30) and EL spectra of SRN/SRO LECs at forward bias for different currents applied with (b) $R_o = 20$ (B20) in the HCS, (c) $R_o = 20$ (B20) in the LCS, and (d) $R_o = 30$ (B30) in the LCS. Inset of each graph are shown photographs of the LEC. ITO was used as gate contact.

(B20) and $R_o = 30$ (B30), are in the HCS ($<20V$), a broad spectrum with the maximum emission centered at about 730 nm and a shoulder at ~ 900 nm is observed. The 730 nm emission increases as the voltage also increases, as observed in **Figure 10(b)**. Nevertheless, first the shoulder at 900 nm increases its intensity when the voltage is between -17 and -18 V and then remains at the same value for larger voltages. As we can see in **Figure 10(b)**, the EL is observed as randomly scattered luminescent spots (mainly red) over the entire LEC surface. The spectrum exhibits that the EL emission follows the PL, showing that the emission is caused by the same luminescent centers.

After current switching, in the LCS ($>20V$), the EL spectra changes, as observed in **Figure 10(c)**. Also, a narrow (width of 7 ± 0.6 nm) and highly intense UV EL peaks appear at $\sim 250, 270, 285, 305, 325,$ and 415 nm. A narrow blue EL peak with the highest intensity is observed at ~ 450 nm. All EL peaks remain at the same wavelength as the current increases. The red EL band observed in the HCS is still present at the LCS, but with a slight redshift and with a low intensity. The emission intensity of the blue EL is about 20 times higher than the red emission. The EL emission is observed as luminescent blue-violet dots randomly distributed on the surface of the contact, as shown in the insets of **Figure 10(c)**.

Figure 10(d) shows the EL emission of the SRN/SRO-LEC with $R_o = 30$ (B30) in the range of LCS ($>35V$). The same narrow and highly intense UV EL peaks at $\sim 250, 270, 285, 305, 325, 415,$ and 450 nm with an average width of 7 ± 0.6 nm are also observed in these devices. Nevertheless, these LECs do not show EL emission in the red-near infrared region.

Four narrow UV EL peaks have been reported at 293.78, 316.10, 403.07, and 444.82 nm, with an average width at half peak of 4 nm, in ITO/ Y_2O_3 /Ag EL devices. This emission was attributed to the characteristic radiation of indium ions [87]. However, as the best of our knowledge, narrow UV EL peaks in silicon rich dielectric materials have not been reported before. The most intense EL peaks emitted by the present SRN/SRO-LECS ($\sim 305, 325, 415,$ and 450 nm) are very similar to those obtained in reference [87], but displaced ~ 10 nm toward longer wavelengths. Thus, they could have a similar origin; however, a deeper analysis of these narrow emission bands needs to be done.

6. Conduction mechanisms

The origin of the EL emission from the SRO, SRN, and SRN/SRO-LECs can be determined by identifying the charge transport mechanism that takes place within the different silicon-rich dielectric materials as discussed below.

6.1. Silicon-rich nitride (SRN)-LECs

Figure 11 shows the $J(E)$ dependency for the SRN-LECs with $R_N = 5, 20,$ and 80 . The conduction mechanism of the carriers in the SRN films was studied by analyzing the different reported mechanism including P-F conduction [88, 89], TAT [90], and space charge limited current (SCLC) [91]. As observed in **Figure 11**, the TAT mechanism is dominating the carrier transport at both forward and reverse bias, and it can be ascribed to the defect states generated during the SRN deposition. A model based on the trap-assisted tunneling carrier transport is shown with the EL radiative recombination process in the reference [34].

6.2. Silicon-rich oxide (SRO)-LECs

Figure 12 shows the experimental J-E data from SRO-LECs with $R_o = 20$ and 30 fitted to the carrier transport mechanisms including Poole-Frenkel (P-F) conduction [88, 89] and trap-assisted tunneling (TAT) [90]. As can be observed, the TAT conduction mechanism predominates in the SRO-LEC with $R_o = 30$ (M30).

The trap energy was estimated to be $\phi_t \cong 1.75$ eV, if a uniformly distributed trap concentration is assumed. It is worth to mention that these trap energy levels correlates well with the one obtained for Er-doped SRO/ SiO_2 superlattice (2.1 eV) and Er-doped SiO_2 (1.9 eV), which are assumed to be deep traps inherent to the SiO_2 [92] possibly neutral oxygen vacancy [93]. Mehonic et al. have reported that the barrier height of the trap is modified by the concentration of oxygen vacancies in the connecting tissue; lower barrier heights correspond to a higher concentration of oxygen vacancies, which defines the device resistance [84]. Moreover, it has been reported that a poor quality of nanocrystalline composite material (formed by Si

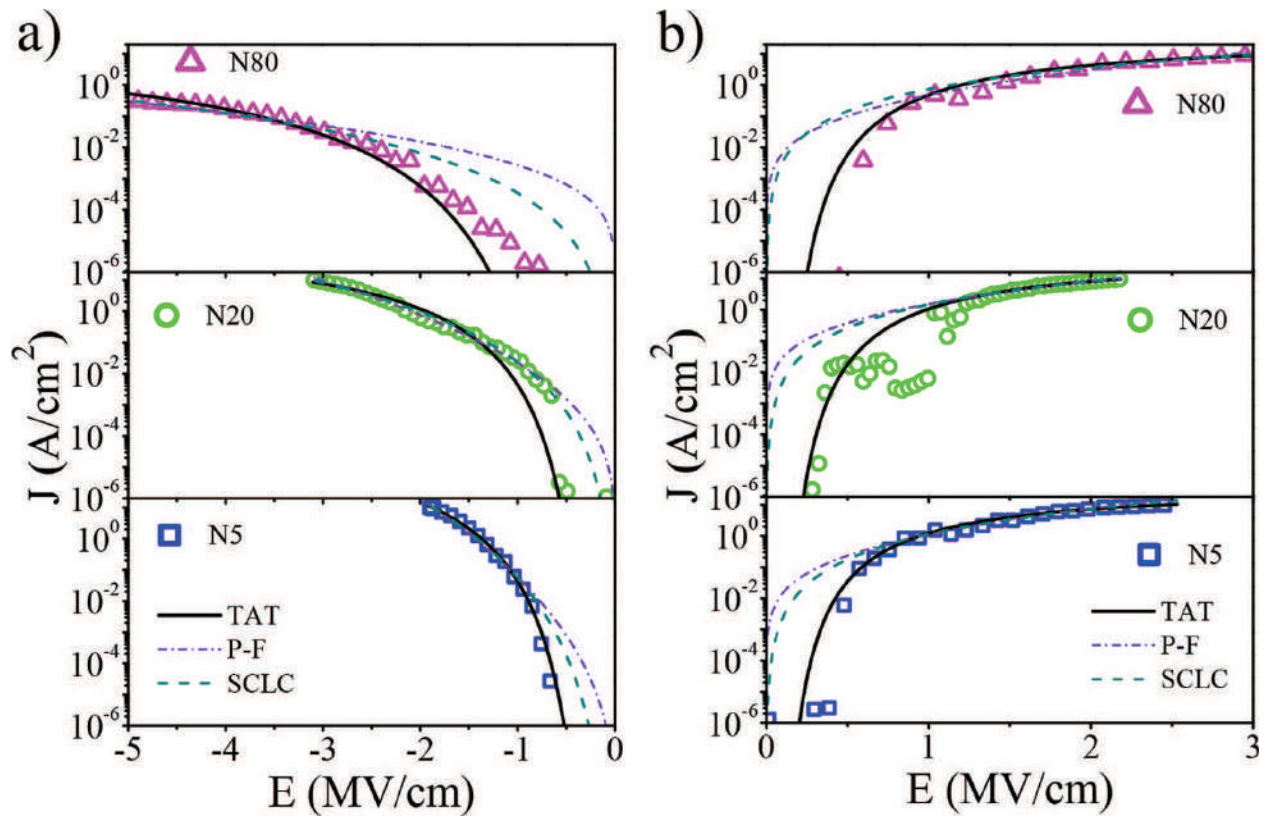


Figure 11. J-E characteristic and conduction mechanism fitting of SRN-LECs with $R_N=5$ (N5), 20 (N20), and 80 (N80) after thermal annealing at: (a) reverse bias (RB) and (b) forward bias (FB). Symbols are the experimental current data, black line represents the TAT conduction, green dash line SCLC, and violet dash dot line the Poole-Frenkel conduction. From Cabañas-Tay et al. [34].

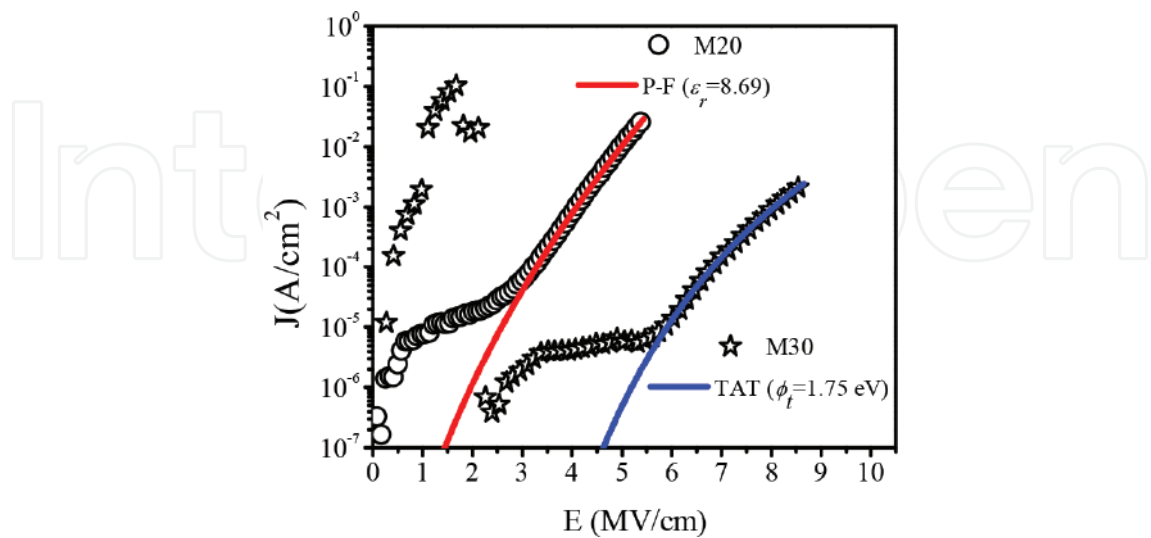


Figure 12. J-E characteristic and conduction mechanism fitting of SRO-LECs with $R_o=30$ (M30) and $R_o=20$ (M20). Red line represents the TAT conduction and blue line the Poole-Frenkel conduction. Symbols are the experimental data. From Palacios-Huerta et al. [46].

nanocrystals and SiO_x) yields parasitic current paths, while low density of nanocrystals turns difficult the direct charge injection into the nanocrystals [94]. A similar behavior is obtained for SRO-LECs with $R_o=30$ (M30), where the annihilation of conductive paths, created by adjacent stable Si-nps and unstable silicon nanoclusters (Si-ncls), produce structural changes including the possible creation of defects. Then, it can be assumed that M30 films exhibit a poor quality of the silicon oxide resulting from the phase separation and the low silicon content. This behavior is well correlated to the blue EL emission observed in the M30-based LECs.

On other hand, the P-F conduction fits well the charge transport in SRO-LECs with $R_o=20$ (M20), as observed in **Figure 12**. A relative permittivity (ϵ_r) value of 9.16 was obtained from the P-F fit for M20, which is closer to the relative permittivity of silicon ($\epsilon_{Si} = 11.9$), similar to other reports [92]. Relatively high permittivity values are a good indication of the large amount of silicon present as Si-nps within the M20 films. Moreover, the Si-nps size calculated by using the P-F estimate relative permittivity are very close to that obtained through the TEM analysis, as reported in [46].

6.3. Silicon-rich nitride/silicon-rich oxide (SRN/SRO)-LECs

When the SRN/SRO bilayer structure is used as active layer in LECs, several charge transport mechanisms are present, as observed in **Figure 13**. For the SRN/SRO-LEC with $R_o=20$ (B20), and in the HCS where red EL emission is observed, the hopping tunneling is the predominant mechanism (pink line), as shown in **Figure 13(a)**.

The average distance between traps (a) was estimated to be about 0.25 nm. When the current switches to the low conduction state, the tunneling mechanism changes, then the P-F conduction

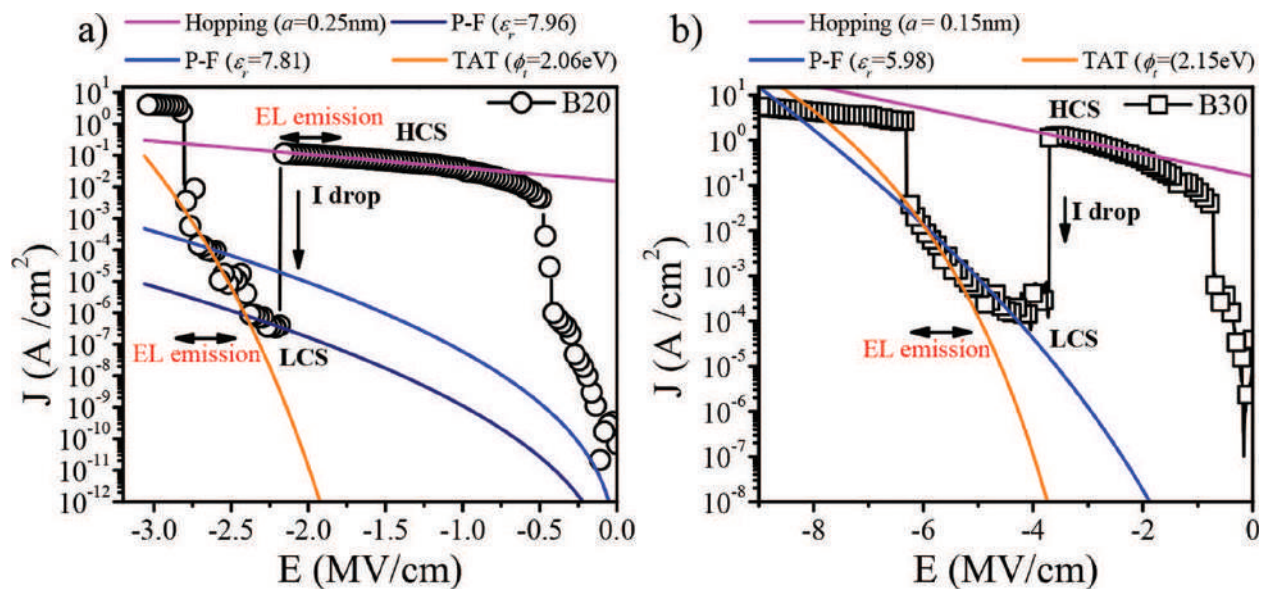


Figure 13. J-E characteristic and conduction mechanism fitting of SRN/SRO-LECs with (a) $R_o=20$ (B20) and (b) $R_o=30$ (B30) thermally annealed at 1100°C. Pink line represents the hopping conduction, orange line the TAT conduction, and blue lines the Poole-Frenkel conduction. Symbols are the experimental data.

dominates (dark blue line). The dielectric constant (ϵ_r) obtained by the P-F fit was about 7.96. However, when the deep UV EL emission starts, the conduction transport is dominated by two different mechanisms: TAT (orange line) and P-F (blue line). In this region, the traps depth obtained by the TAT fit was about 2.06 eV, and the dielectric constant (ϵ_r) obtained by the P-F fit was about 7.81.

The SRN/SRO-LECs with $R_o = 30$ (B30) behaves similar to the B20 bilayer, as observed in **Figure 13(b)**. In the high conduction state, the dominant mechanism is hopping tunneling (pink line), where the average distance between traps is about 0.15 nm, indicating a higher density of traps compared to the B20 sample (0.25 nm). When the current drops to the low conduction state, the dominating mechanism changes to the P-F conduction (blue line). The dielectric constant (ϵ_r) was estimated at 5.98, indicating a lower content of silicon related to B20 sample (8.61), as expected. However, when the EL emission starts, the conduction begins to be dominated by TAT (orange line). The traps depth was estimated at about 2.15 eV, very similar to that obtained in B20 sample (2.06) and very close to the depth at which are the centers K^0 (~2.1 eV) [64].

In summary, the conduction mechanism in the region of low electric fields at HCS is hopping for SRN/SRO bilayers. It was observed that when the nitrogen content in the SRO layer increases, the average distance between defects also increases either due to the defects passivation or due to the reduction of the Si-nps size. In the region of high electric fields at low conduction, both TAT and P-F mechanisms take place simultaneously. The trap depth, obtained by the TAT fit, was ~2.1 eV from the minimum of the conduction band for both bilayers (B20 and B30), which relates to the location of the centers K^0 in SRN film.

7. Conclusions

The compositional, structural, optical, and electro-optical properties of SRO, SRN films as well as combination of SRN/SRO bilayers deposited by LPCVD were studied. The EL of the SRN-LECs showed a broad emission spectrum where the maximum peak blueshifts when the polarity changed from reverse to forward bias. The EL spectrum was nearly similar to that of PL when LECs were forwardly biased and the silicon excess was increased. Analyzing the current-voltage characteristics, it was found that TAT was the main carrier transport mechanism in SRN films in both biases, where typical EL was observed. In SRO films, it was demonstrated that the silicon content affects the luminescence centers density obtaining the EL emission at lower electric field as the silicon excess increased. SRO with $R_o = 30$ films exhibited the presence of structural defects like NOV, NBOHC, and E'_s ($Si\uparrow Si=Si$) centers, which produced blue to red PL band after thermal annealing. SRO with $R_o = 20$ films showed mainly red PL produced by the presence of well-defined Si-ncs. It was found that SRO-LECs with $R_o = 30$ shows an intense blue EL, after a resistance switching behavior was reached. The RS was originated by the annihilation of preferential conductive paths created by Si-nps and silicon nanoclusters through structural changes that result in a long spectral blueshift (~222 nm) between the PL and EL. On the other hand, the RS was not observed in

SRO-LECs with $R_o = 20$ due to the well-defined Si-nps with 2.7 nm size. These well-defined Si-nps produce a better charge injection through multiple conductive paths enhancing an intense red EL, which is related mainly to defects at the Si-nps/SiO_x interface. The transport mechanism was affected by the composition and structure of the films, being TAT and PF the dominant transport mechanism in SRO with $R_o = 30$ and 20, respectively. When the SRN was deposited onto the SRO to form the bilayer, compositional and electro-optical changes were observed. The SRN/SRO layers showed a broad PL emission respect to a simple SRO or SRN layer. In addition, multiple defects or centers were responsible of PL emission. The same luminescent centers in SRN/SRO were present in SRO and SRN monolayers. SRN/SRO-LECs showed an intense UV EL at high electric fields related to indium ions radiation. The conduction mechanism in SRN/SRO bilayers was found to be dominated by Pool-Frenkel and TAT mechanisms at LCS, and hopping at HCS.

Acknowledgements

This work has been partially supported by the project CONACyT-180992. The authors acknowledge technicians Pablo Alarcon, Armando Hernández, and Victor Aca from INAOE and Luis Gerardo Silva from CIMAV.

Author details

Santiago A. Cabañas-Tay¹, Liliana Palacios-Huerta², Mariano Aceves-Mijares², Antonio Coyopol¹, Sergio A. Pérez-García¹, Liliana Licea-Jiménez¹, Carlos Domínguez³ and Alfredo Morales-Sánchez^{1*}

*Address all correspondence to: alfredo.morales@cimav.edu.mx

1 Advanced Materials Research Center (CIMAV), Monterrey-PIIT Apodaca, Nuevo León, México

2 Electronics Department, National Institute of Astrophysics Optics and Electronics Tonantzintla, Puebla, México

3 Microelectronics Institute of Barcelona (IMB-CNM, CSIC) Bellaterra, Barcelona, Spain

References

- [1] Tseng C.-K., Lee M.-C. M., Hung H.-W., Huang J.-R., Lee K.-Y., Shieh J.-M., and Lin G.-R. Silicon-nanocrystal resonant-cavity light emitting devices for color tailoring. *Journal of Applied Physics*. 2012;111(7): 074512. DOI: 10.1063/1.3702793
- [2] Zhiping Z., Bing Y., and Jurgen M. On-chip light sources for silicon photonics. *Light: Science & Applications*. 2015;4: e358. DOI: 10.1038/lsa.2015.131

- [3] Berencén Y., Illera S., Rebohle L., Ramírez J. M., Wutzler R., Cirera A., Hiller D., Rodríguez J. A., Skorupa W., and Garrido B. Luminescence mechanism for Er³⁺ ions in a silicon-rich nitride host under electrical pumping. *Journal of Physics D: Applied Physics*. 2016;49(8): 085106. DOI: 10.1088/0022-3727/49/8/085106
- [4] Canham L. T. Silicon quantum wire array fabrication by electrochemical and chemical dissolution of wafers. *Applied Physics Letters*. 1990;57:1046–1048. DOI: 10.1063/1.103561
- [5] Delerue C., Allan G., and Lannoo M. Theoretical aspects of the luminescence of porous silicon. *Physical Review B*. 1993;48(15):11024–11036. DOI: 10.1103/PhysRevB.48.11024
- [6] Barreto J., Morales A., Perálvarez M., Garrido B., and Domínguez C. Stoichiometry of silicon-rich dielectrics for silicon nanocluster formation. *Physica Status Solidi (C)*. 2011;8(3):1610–1642. DOI: 10.1002/pssc.201000363
- [7] Shih C.-F., Hsiao C.-Y., and Su K.-W. Enhanced white photoluminescence in silicon-rich oxide/SiO₂ superlattices by low-energy ion-beam treatment. *Optics Express*. 2013;21(13): 15888–15895. DOI: 10.1364/OE.21.015888
- [8] Mohammed S., Nimmo M. T., Malko A. V., and Hinkle C. L. Chemical bonding and defect states of LPCVD grown silicon-rich Si₃N₄ for quantum dot applications. *Journal of Vacuum Science & Technology A*. 2014;32(2): 021507. DOI: 10.1116/1.4861338
- [9] Liao W., Zeng X., Wen X. and Wen Y. Tunable photoluminescence of Si-rich nitride films with silicon quantum dots by changing the total pressure. *International Photonics and Optoelectronics*. 2015; JW3A.33. DOI: 10.1364/OEDI.2015.JW3A.33
- [10] Vlasukova L. A., Komarov F. F., Parkhomenko I. N., Milchanin O. V., Makhavikou M. A., Mudryi A. V., Žuk, J., Kopychiński P., and Togambayeva A. K. Visible photoluminescence of non-stoichiometric silicon nitride films: The effect of annealing temperature and atmosphere. *Journal of Applied Spectroscopy*. 2015;82(3): 386–389. DOI: 10.1007/s10812-015-0117-9
- [11] Lin G.-R., Lin C.-J., and Lin C.-K. Enhanced Fowler-Nordheim tunneling effect in nanocrystallite Si based LED with interfacial Si nano-pyramids. *Optics Express*. 2007;15(5):2555–2563. DOI: 10.1364/OE.15.002555
- [12] Lin Y.-H., Wu C.-L., Pai Y.-H., and Lin G.-R. A 533-nm self-luminescent Si-rich SiN_x/SiO_x distributed Bragg reflector. *Optics Express*. 2011;19(7):6563–6570. DOI: 10.1364/OE.19.006563
- [13] Nishi H., Tsuchizawa T., Shinojima H., Watanabe T., Itabashi S-I., Kou R., Fukuda H., and Yamada K. Low-polarization-dependent silica waveguide monolithically integrated on SOI photonic platform. *Journal of Lightwave Technology*. 2013;31(11):1821–1827. DOI: 10.1109/JLT.2013.2256880
- [14] Cheng C.-H., Lien Y.-C., and Wu C.-L., and Lin G.-R. Multicolor electroluminescent Si quantum dots embedded in SiO_x thin film MOSLED with 2.4% external quantum efficiency. *Optics Express*. 2013;21(1): 391–403. DOI: 10.1364/OE.21.000391

- [15] Zimmermann H., editors. *Integrated Silicon Optoelectronics*. 2nd ed. Germany: Springer-Verlag Berlin Heidelberg; 2010. 406 p. DOI: 10.1007/978-3-642-01521-2
- [16] Pavesi L., Gaponenko S., and Dal Negro L., editors. *Towards the First Silicon Laser*. 1st ed. Dordrecht: Kluwer Academic Publishers; 2003. 490 p. DOI: 10.1007/978-94-010-0149-6
- [17] Klak M. M., Zatoryb G., Wojcik J., Misiewicz J., Mascher P., and Podhorodecki A. Mechanism of enhanced photoluminescence of Tb ions in hydrogenated silicon-rich silicon oxide films. *Thin Solid Films*. 2016;611: 62–67. DOI: 10.1016/j.tsf.2016.04.050
- [18] Barbagioanni E. G., Lockwood D. J., Simpson P. J., and Goncharova, L. V. Quantum confinement in Si and Ge nanostructures. *Journal of Applied Physics*. 2012;111(3): 034307. DOI: 10.1063/1.3680884
- [19] Iacona F., Franzò G., and Spinella C. Correlation between luminescence and structural properties of Si nanocrystals. *Journal of Applied Physics*. 2000;87(3): 1295–1303. DOI: 10.1063/1.372013
- [20] Kim T.-W., Cho C.-H., Kim B.-H., and Park S.-J. Quantum confinement effect in crystalline silicon quantum dots in silicon nitride grown using SiH₄ and NH₃. *Applied Physics Letters*. 2006;88(12): 123102. DOI: 10.1063/1.2187434
- [21] Qin G. G., Li A. P., Zhang B. R., and Li B.-C. Visible electroluminescence from semitransparent Au film/extra thin Si-rich silicon oxide film/p-Si structure. *Journal of Applied Physics*. 1995;78(3): 2006–2009. DOI: 10.1063/1.360175
- [22] Lin G.-R., and Lin C.-J. Improved blue-green electroluminescence of metal-oxide-semiconductor diode fabricated on multirecipe Si-implanted and annealed SiO₂/Si substrate. *Journal of Applied Physics*. 2004;95(12): 8484–8486. DOI: 10.1063/1.1739283
- [23] Liu Y., Chen T. P., Ding L., Yang M., Wong J. I., Ng C. Y., Yu S. F., Li Z. X., Yuen C., Zhu F. R., Tan M. C., and Fung S. Influence of charge trapping on electroluminescence from Si-nanocrystal light emitting structure. *Journal of Applied Physics*. 2007;101(10): 104306. DOI: 10.1063/1.2713946
- [24] Liao L.-S., Bao X.-M., Li N.-S., Zheng X.-Q., and Min N.-B. Visible electroluminescence from Si⁺-implanted SiO₂ films thermally grown on crystalline Si. *Solid State Communications*. 1996;97(12): 1039–1042. DOI: 10.1016/0038-1098(95)00846-2
- [25] Wang T., Wei D. Y., Sun H. C., Liu Y., Chen D. Y., Chen G. R., Xu J., Li W., Ma Z. Y., Xu L., and Chen K. J. Electrically driven luminescence of nanocrystalline Si/SiO₂ multilayers on various substrates. *Physica E: Low-dimensional Systems and Nanostructures*. 2009;41(6): 923–926. DOI: 10.1016/j.physe.2008.08.001
- [26] López-Vidrier J., Berencén Y., Hernández S., Blázquez O., Gutsch S., Laube J., Hiller D., Löper P., Schnabel M., Janz S., Zacharias M., and Garrido B. Charge transport and electroluminescence of silicon nanocrystals/SiO₂ superlattices. *Journal of Applied Physics*. 2013;114(16): 163701. DOI: 10.1063/1.4826898

- [27] Cho K. S., Park N.-M., Kim T.-Y., Kim K.-H., Shin J.-H., Sung G. Y., and Shin J. H. High efficiency visible electroluminescence from silicon nanocrystals embedded in silicon nitride using a transparent doping layer. *Applied Physics Letters*. 2006;88(20): 209904. DOI: 10.1063/1.2205754
- [28] Huang R., Chen K., Qian B., Chen S., Li W., Xu J., Ma Z., and Huang X. Oxygen induced strong green light emission from low-temperature grown amorphous silicon nitride films. *Applied Physics Letters*. 2006;89(22): 221120. DOI: 10.1063/1.2399393
- [29] Huang R., Chen K., Dong H., Wang D., Ding H., Li W., Xu J., Ma Z., and Xu L. Enhanced electroluminescence efficiency of oxidized amorphous silicon nitride light-emitting devices by modulating Si/N ratio. *Applied Physics Letters*. 2007;91(11): 111104. DOI: 10.1063/1.2783271
- [30] Cen Z. H., Chen T. P., Liu Z., Liu Y., Ding L., Yang M., Wong J. I., Yu S. F., and Goh W. P. Electrically tunable white-color electroluminescence from Si-implanted silicon nitride thin film. *Optics Express*. 2010;18(19): 20439–20444. DOI: 10.1364/OE.18.020439
- [31] Warga J., Li R., Basu S. N., and Dal Negro L. Electroluminescence from silicon-rich nitride/silicon superlattice structures. *Applied Physics Letters*. 2008;93(15): 151116. DOI: 10.1063/1.3003867
- [32] Tai H. Y., Lin Y. H., and Lin G. R. Wavelength-shifted yellow electroluminescence of Si quantum-dot embedded 20-pair SiN_x/SiO_x superlattice by Ostwald ripening effect. *IEEE Photonics Journal*. 2013;5(1): 6600110. DOI: 10.1109/JPHOT.2012.2232285
- [33] González-Fernández A. A., Juvert J., Aceves-Mijares M., and Domínguez C. Monolithic integration of a silicon-based photonic transceiver in a CMOS Process. *IEEE Photonics Journal*. 2016;8(1):1–13. DOI: 10.1109/JPHOT.2015.2505144
- [34] Cabañas-Tay S. A., Palacios-Huerta L., Luna-López J. A., Aceves-Mijares M., Alcántara-Iniesta S., Pérez-García S. A., and Morales-Sánchez A. Analysis of the luminescent centers in silicon rich silicon nitride light-emitting capacitors. *Semiconductor Science and Technology*. 2015;30(6):065009. DOI: 10.1088/0268-1242/30/6/065009
- [35] Tsu D. V., Lucovsky G., Mantini M. J., and Chao S. S. Deposition of silicon oxynitride thin films by remote plasma enhanced chemical vapor deposition. *Journal of Vacuum Science & Technology A*. 1987;5(4):1998–2002. DOI: 10.1116/1.574902
- [36] Vuillod J. Preparation and characterization of plasma enhanced chemical vapor deposited silicon nitride and oxynitride films. *Journal of Vacuum Science & Technology A*. 1987;5(4):1675–1679. DOI: 10.1116/1.574545
- [37] Debieu O., Nalini R. P., Cardin J., Portier X., Perrière J., and Gourbilleau F. Structural and optical characterization of pure Si-rich nitride thin films. *Nanoscale Research Letters*. 2013;8(1): 1–13. DOI: 10.1186/1556-276X-8-31
- [38] Lin K-C, and Lee S-C. The structural and optical properties of a-SiN_x:H prepared by plasma-enhanced chemical-vapor deposition. *Journal of Applied Physics*. 1992;72(11):5474–5482. DOI: 10.1063/1.351992

- [39] Scardera G., Puzzer T., Conibeer G., and Green M. A. Fourier transform infrared spectroscopy of annealed silicon-rich silicon nitride thin films. *Journal of Applied Physics*. 2008;104(10):104310. DOI: 10.1063/1.3021158
- [40] Tsu D. V., Lucovsky G., and Mantini M. J. Local atomic structure in thin films of silicon nitride and silicon diimide produced by remote plasma-enhanced chemical-vapor deposition. *Physical Review B*. 1986;33(10):7069–7076. DOI: 10.1103/PhysRevB.33.7069
- [41] Aceves-Mijares M., Espinosa-Torres N. D., Flores-Gracia F., González-Fernández A. A., López-Estopier R., Román-López S., Pedraza G., Domínguez C., Morales A., and Falcony C. Composition and emission characterization and computational simulation of silicon rich oxide films obtained by LPCVD. *Surface and Interface Analysis*. 2014;46: 216–223. DOI:10.1002/sia.5212
- [42] Fazio E., Barletta E., Barreca F., Neri F., and Trusso S. Investigation of a nanocrystalline silicon phase embedded in SiO_x thin films grown by pulsed laser deposition. *Journal of Vacuum Science & Technology B*. 2005;23(2):519–524. DOI: 10.1116/1.1880252
- [43] Schliwinski H. -J., Schnakenberg U., Windbracke W., Neff H., and Lange P. Thermal annealing effects on the mechanical properties of plasma-enhanced chemical vapor deposited silicon oxide films. *Journal of the Electrochemical Society*. 1992;139(6):1730–1735. DOI: 10.1149/1.2069484
- [44] Pai P. G., Chao S. S., Takagi Y., and Lucovsky G. Infrared spectroscopic study of SiO_x films produced by plasma enhanced chemical vapor deposition. *Journal of Vacuum Science & Technology A*. 1986;4(3):689–694. DOI: 10.1116/1.573833
- [45] Diniz J. A., Tatsch P. J., and Pudenzi M. A. A. Oxynitride films formed by low energy NO⁺ implantation into silicon. *Applied Physics Letters*. 1996;69(15):2214–2215. DOI: 10.1063/1.117169
- [46] Palacios-Huerta L., Cabañas-Tay S. A., Luna-López J. A., Aceves-Mijares M., Coyopol A., and Morales-Sánchez A. Effect of the structure on luminescent characteristics of SRO-based light emitting capacitors. *Nanotechnology*. 2015;26(39):395202. DOI: 10.1088/0957-4484/26/39/395202
- [47] Morales-Sánchez A., Monfil-Leyva K., González A. A., Aceves-Mijares M., Carrillo J., Luna-López J. A., Domínguez C., Barreto J., and Flores-Gracia F. J. Strong blue and red luminescence in silicon nanoparticles based light emitting capacitors. *Applied Physics Letters*. 2011;99(17):171102. DOI: 10.1063/1.3655997
- [48] Lin G.-R., Lin C.-J., and Kuo H.-C. Improving carrier transport and light emission in a silicon-nanocrystal based MOS light-emitting diode on silicon nanopillar array. *Applied Physics Letters*. 2007;91(9):093122. DOI: 10.1063/1.2778352
- [49] Dohnalová K., Ondič L., Kusová K., Pelant I., Rehspringer J. L., and Mafouana R.-R. White-emitting oxidized silicon nanocrystals: Discontinuity in spectral development with reducing size. *Journal of Applied Physics*. 2010;107(5):053102. DOI: 10.1063/1.3289719

- [50] Wang X., Zhang R. Q., Lee S. T., Niehaus T. A., and Frauenheim T. Unusual size dependence of the optical emission gap in small hydrogenated silicon nanoparticles. *Applied Physics Letters*. 2007;90(12):123116. DOI: 10.1063/1.2715101
- [51] Cueff S., Labbé C., Jambois O., Berencén Y., Kenyon A. J., Garrido B., and Rizk R. Structural factors impacting carrier transport and electroluminescence from Si nano-cluster-sensitized Er ions. *Optics Express*. 2012;20(20): 22490–22502. DOI: 10.1364/OE.20.022490
- [52] Kiebach R., Yu Z., Aceves-Mijares M., Bian D., and Du J. The deposition and control of self-assembled silicon nano islands on crystalline silicon. *International Journal of High Speed Electronics and Systems*. 2008;18(4):901–910. DOI: 10.1142/S0129156408005862
- [53] Park N.-M., Choi C.-J., Seong T.-Y., and Park S.-J. Quantum confinement in amorphous silicon quantum dots embedded in silicon nitride. *Physical Review Letters*. 2001;86(7):1355–1357. DOI: 10.1103/PhysRevLett.86.1355
- [54] Wang Y. Q., Wang Y. G., Cao L., and Cao Z. X. High-efficiency visible photoluminescence from amorphous silicon nanoparticles embedded in silicon nitride. *Applied Physics Letters*. 2003;83(17):3474–3476. DOI: 10.1063/1.1621462
- [55] Park N.-M., Kim T.-S., and Park S.-J. Band gap engineering of amorphous silicon quantum dots for light-emitting diodes. *Applied Physics Letters*. 2001;78(17):2575–2577. DOI: 10.1063/1.1367277
- [56] Mercaldo L. V., Veneri P. D., Esposito E., Massera E., Usatii I., and Privato C. PECVD in-situ growth of silicon quantum dots in silicon nitride from silane and nitrogen. *Materials Science and Engineering B*. 2009;159–160:77–79. DOI: 10.1016/j.mseb.2008.09.029
- [57] Liao W., and Zeng X., Wen X., Chen X., and Wang W. Annealing and excitation dependent photoluminescence of silicon rich silicon nitride films with silicon quantum dots. *Vacuum*. 2015;121: 147–151. DOI: 10.1016/j.vacuum.2015.08.002
- [58] Xie M., Li D., Wang F., and Yang D. Luminescence properties of silicon-rich silicon nitride films and light emitting devices. *ECS Transactions*. 2011;35(18):3–19. DOI: 10.1149/1.3647900
- [59] Dal Negro L., Li R., Warga J., and Basu S. N. Sensitized erbium emission from silicon-rich nitride/silicon superlattice structures. *Applied Physics Letters*. 2008;92(18):181105. DOI: 10.1063/1.2920435
- [60] Sahu B. S., Delachat F., Slaoui A., Carrada M., Ferblantier G., Muller D. Effect of annealing treatments on photoluminescence and charge storage mechanism in silicon-rich SiN_x:H films. *Nanoscale Research Letters*. 2011;6(1):1–10. DOI: 10.1186/1556-276X-6-178
- [61] Giorgis F., Vinegoni C., and Pavesi L. Optical absorption and photoluminescence properties of a-Si_{1-x}:H films deposited by plasma-enhanced cvd. *Physical Review B*. 2000;61(7):4693–4698. DOI: 10.1103/PhysRevB.61.4693

- [62] Warren W. L., Robertson J., and Kanicki J. Si and N dangling bond creation in silicon nitride thin films. *Applied Physics Letters*. 1993;63(19):2685–2687. DOI: 10.1063/1.110420
- [63] Warren W. L., Lenahan P. M., and Curry S. E. First observation of paramagnetic nitrogen dangling-bond centers in silicon nitride. *Physical Review Letters*. 1990;65(2):207–210. DOI: 10.1103/PhysRevLett.65.207
- [64] Robertson J., and Powell M. J. Gap states in silicon nitride. *Applied Physics Letters*. 1984;44(4):415–417. DOI: 10.1063/1.94794
- [65] Liu Y., Zhou Y., Shi W., Zhao L., Sun B., and Ye T. Study of photoluminescence spectra of Si-rich SiN_x films. *Materials Letters*. 2004;58(19):2397–2400. DOI: 10.1016/j.matlet.2004.02.015
- [66] Nguyen P. D., Kepaptsoglou D. M., Ramasse Q. M., Sunding M. F., Vestland L. O., Finstad T. G., and Olsen A. Impact of oxygen bonding on the atomic structure and photoluminescence properties of Si-rich silicon nitride thin films. *Journal of Applied Physics*. 2012;112(7):073514. DOI: 10.1063/1.4756998
- [67] Hao X. J., Podhorodecki A. P., Shen Y. S., Zatoryb G., Misiewicz J., and Green M. A. Effects of Si-rich oxide layer stoichiometry on the structural and optical properties of Si QD/SiO₂ multilayer films. *Nanotechnology*. 2009;20(48):485703. DOI: 10.1088/0957-4484/20/48/485703
- [68] Lai B. H., Cheng C. H., and Lin G. R.. Multicolor ITO/SiO_x/p-Si/Al Light Emitting Diodes With Improved Emission Efficiency by Small Si Quantum Dots. *IEEE Journal of Quantum Electronics*. 2011;47(5):698–704. DOI: 10.1109/JQE.2011.2109699
- [69] González-Fernández A. A., Aceves-Mijares M., Morales-Sánchez A., and Monfil-Leyva K. Intense whole area electroluminescence from low pressure chemical vapor deposition-silicon-rich oxide based light emitting capacitors. *Journal of Applied Physics*. 2010;108(4):043105. DOI: 10.1063/1.3465335
- [70] Salh R. Defect Related Luminescence in Silicon Dioxide Network: A Review. In: Prof. Sukumar Basu, editor. *Crystalline Silicon—Properties and Uses*. Umeå, Sweden: InTech; 2011. DOI: 10.5772/22607
- [71] Rodríguez J. A., Vásquez-Agustín M. A., Morales-Sánchez A., and Aceves-Mijares M. Emission mechanisms of Si nanocrystals and defects in SiO₂ materials. *Journal of Nanomaterials*. 2014;2014:409482. DOI: 10.1155/2014/409482
- [72] González-Fernández A. A., Juvert J., Aceves-Mijares M., Llobera A., and Domínguez C. Influence of silicon binding energy on photoluminescence of Si-implanted silicon dioxide. *ECS Transactions*. 2012;49(1):307–314. DOI: 10.1149/04901.0307ecst
- [73] Perálvarez M., Carreras J., Barreto J., Morales A., Domínguez C., and Garrido B. Efficiency and reliability enhancement of silicon nanocrystal field-effect luminescence from nitride-oxide gate stacks. *Applied Physics Letters*. 2008;92(24):241104. DOI: 10.1063/1.2939562

- [74] Parker C. G., Lucovsky G., and Hauser J. R. Ultrathin oxide-nitride gate dielectric MOSFET's. *IEEE Electron Device Letters*. 1998;19(4):106–108. DOI: 10.1109/55.663529
- [75] Wang X., Huang R., Song C., Guo Y., and Song J. Effect of barrier layers on electroluminescence from Si/SiO_xN_y multilayer structures. *Applied Physics Letters*. 2013;102(8):081114. DOI: 10.1063/1.4794079
- [76] Berencén Y., Ramírez J. M., Jambois O., Domínguez C., Rodríguez J. A., and Garrido B. Correlation between charge transport and electroluminescence properties of Si-rich oxide/nitride/oxide-based light emitting capacitors. *Journal of Applied Physics*. 2012;112(10):109901. DOI: 10.1063/1.4768249
- [77] Pei Z., Chang Y. R., and Hwang H. L. White electroluminescence from hydrogenated amorphous-SiN_x thin films. *Applied Physics Letters*. 2002;80(16):2839–2841. DOI: 10.1063/1.1473230
- [78] Li D., Huang J., and Yang D. Enhanced electroluminescence of silicon-rich silicon nitride light-emitting devices by NH₃ plasma and annealing treatment. *Physica E: Low-dimensional Systems and Nanostructures*. 2009;41(6):920–922. DOI: 10.1016/j.physe.2008.08.024
- [79] Morales-Sánchez A., Barreto J., Domínguez C., Aceves-Mijares M., and Luna-López J. A. The mechanism of electrical annihilation of conductive paths and charge trapping in silicon-rich oxides. *Nanotechnology*. 2009;20(4):045201. DOI: 10.1088/0957-4484/20/4/045201
- [80] Morales-Sánchez A., Barreto J., Domínguez C., Aceves-Mijares M., Perálvarez M., Garrido B., and Luna-López J. A. DC and AC electroluminescence in silicon nanoparticles embedded in silicon-rich oxide films. *Nanotechnology*. 2010;21(8):085710. DOI: 10.1088/0957-4484/21/8/085710
- [81] Yao J., Sun Z., Zhong L., Natelson D., and Tour J. M. Resistive switches and memories from silicon oxide. *Nano Letters*. 2010;10(10):4105–4110. DOI: 10.1021/nl102255r
- [82] Yao J., Zhong L., Natelson D., and Tour J. M. In situ imaging of the conducting filament in a silicon oxide resistive switch. *Scientific Reports*. 2012;2:242. DOI: 10.1038/srep00242
- [83] Mehonic A., Vrajitoarea A., Cuff S., Hudziak S., Howe H., Labbé C., Rizk R., Pepper M., and Kenyon A. J. Quantum conductance in silicon oxide resistive memory devices. *Scientific Reports*. 2013;3:2708. DOI: 10.1038/srep02708
- [84] Mehonic A., Cuff S., Wojdak M., Hudziak S., Labbé C., Rizk R., and Kenyon A. J. Electrically tailored resistance switching in silicon oxide. *Nanotechnology*. 2012;23(45):455201. DOI: 10.1088/0957-4484/23/45/455201
- [85] González-Fernández A. A., Juvert J., Aceves-Mijares M., Llobera A., and Domínguez C. Influence by layer structure on the output EL of CMOS compatible silicon-based light emitters. *IEEE Transactions on Electron Devices*. 2012;60(6): 1971–1974. DOI: 10.1109/TED.2013.2258158
- [86] Wang D.-C., Chen J.-R., Zhu J., Lu C.-T., and Lu M. On the spectral difference between electroluminescence and photoluminescence of Si nanocrystals: a mechanism study of

electroluminescence. *Journal of Nanoparticle Research*. 2013;15(11):1–7. DOI: 10.1007/s11051-013-2063-x

- [87] Yin X., Wang S., Li L., Mu G., Tang Y., Duan W., and Yi L. Intense deep-blue electroluminescence from ITO/Y₂O₃/Ag structure. *Optics Express*. 2015;23(14):18092–18097. DOI: 10.1364/OE.23.018092
- [88] Huang R., Song J., Wang X., Guo Y. Q., Song C., Zheng Z. H., Wu X. L., and Chu P. Origin of strong white electroluminescence from dense Si nanodots embedded in silicon nitride. *Optics Letters*. 2012;37(4):692–694. DOI: 10.1364/OL.37.000692
- [89] Tao Y., Zheng J., Zuo Y., Xue C., Cheng B., and Wang Q. Enhanced current transportation in silicon-riched nitride (SRN)/silicon-riched oxide (SRO) multilayer nanostructure. *Nano-Micro Letters*. 2012;4(4): 202–207. DOI: 10.1007/BF03353715
- [90] Huang R., Wang D. Q., Ding H. L., Wang X., Chen K. J., Xu J., Guo Y. Q., Song J., and Ma Z. Y. Enhanced electroluminescence from SiN-based multilayer structure by laser crystallization of ultrathin amorphous Si-rich SiN layers. *Optics Express*. 2010;18(2):1144–1150. DOI: 10.1364/OE.18.001144
- [91] Vila M., Prieto C., and Ramírez R. Electrical behavior of silicon nitride sputtered thin films. *Thin Solid Films*. 2004;459(1–2):195–199. DOI: 10.1016/j.tsf.2003.12.082
- [92] Ramírez J. M., Berencén Y., López-Conesa L., Rebled J. M., Peiró F., and Garrido B. Carrier transport and electroluminescence efficiency of erbium-doped silicon nanocrystal superlattices. *Applied Physics Letters*. 2013;103(8):081102. DOI: 10.1063/1.4818758
- [93] Perera R., Ikeda A., Hattori R., and Kuroki Y. Trap assisted leakage current conduction in thin silicon oxynitride films grown by rapid thermal oxidation combined microwave excited plasma nitridation. *Microelectronic Engineering*. 2003;65(4):357–370. DOI: 10.1016/S0167-9317(02)01025-0
- [94] Anopchenko A., Marconi A., Moser E., Prezioso S., Wang M., Pavese L., Pucker G., and Bellutti P. Low-voltage onset of electroluminescence in nanocrystalline-Si/SiO₂ multilayers. *Journal of Applied Physics*. 2009;106(3):033104. DOI: 10.1063/1.3194315